UNIVERSITY OF GENOA

# Battery Energy Storage System converter control: Virtual Generator application for fault conditions

by

Alessandro Rosini

A thesis submitted in partial fulfillment for the
degree of Doctor of Philosophy in Electrical Engineering

in the
Faculty of Engineering
Department of Electrical, Electronic, Telecommunications Engineering, and
Naval Architecture

Tutor: Prof. Andrea Bonfiglio
Supervisor of the PhD Program: Prof. Mario Marchesoni

May 2021

*Dedicato a miei Nonni*

*"Remember to look up at the stars and not down at your feet. Try to make sense of what you see and wonder about what makes the universe exist. Be curious. And however difficult life may seem, there is always something you can do and succeed at. It matters that you don't just give up."*

Stephen Hawking

*"Logic will get you from A to Z; imagination will get you everywhere."*

Albert Einstein

# *Abstract*

The growing need of integrate renewable energies, such as wind and solar has been driven by the necessity of reducing air pollutant, reducing greenhouse gases emissions, improving public health and having energy supply diversification. This need of sustainability cannot exclude the necessity to guarantee reliability and stability of the electrical power system, and more specifically Microgrid systems, both in normal operating scenarios and during unexpected events such as unintentional islanding or fault events. For this reason renewable generation as to be support by intelligent system such as Battery Energy Storage Systems in order to have an energy reserve able to follow the oscillations of the renewable energies and to guarantee a stable control of voltage and frequency. These energy sources are typically connected via power electronics in order to have rapid response and degree of freedom to implement several control techniques. But the increase in the interfacing of energy sources with inverters has contributed to the reduction of system inertia and this aspect has to be investigated. This thesis proposes a new control algorithm for Battery Energy Storage System able to provide inertial contribution in order to mimic the behaviour of a synchronous generator and then a new approach to adapt this algorithm to fault condition which can cause severe instability of the Microgrid.

After a first introduction chapter, Chapter 2 presents the new Virtual Synchronous Generator control algorithm and some simulations carried out with the dedicated simulation software DIgSILENT PowerFactory® show the correct dynamic behaviour in normal operating scenarios. Then Chapter 3 deals with the modification of the proposed control scheme in order to properly manage symmetrical faults in islanded and grid connected configuration with a particular focus on the resynchronisation problem. Chapter 4 proposes a complete set of simulations in order to show the excellent results obtained in this research field. Overall conclusions and final remarks are reported in Chapter 5.

This Ph.D. thesis is an outcome of a scientific research that I have conduct during the three years long Ph.D. program, in collaboration with and founded by Hitachi Power Grids.

# *Acknowledgements*

Sento il forte bisogno di iniziare questo capitolo di ringraziamenti con un pensiero al periodo che abbiamo attraversato, e che stiamo attravesrsando nel momento in cui scrivo questi ringraziamneti in maniera tale che anche io, quando tra molti anni riprenderò in mano questa tesi, potrò rileggere nero su bianco le sensazioni di questo periodo. Questa tesi di dottorato prende forma in un periodo molto complicato, che ha segnato tutti nel profondo, che ci ha fatto usare vocaboli non proprio di uso comune: ”tampone molecolare” , ”test antigenico”, ”assembramento”, ”distanziamento sociale” e così via. Un periodo che ci ha dato una sofferenza profonda, intima, che ci ha tenuti lontano dalle persone che più amiamo nel momento in cui ne avremmo avuto più bisogno. Ma nonostante ciò, nonstante tutto ciò, la passione e per questa materia stupenda che è l'Ingegneria dei Sistemi Elettrici, la dedizione, le soddisfazioni per ogni successo, e anche le delusioni di fronte agli insuccessi hanno contribuito ad avere sempre una luce guida nel mio percorso di vita, anche quando sembrava che il buio non ci abbandonasse mai. Staccare la testa dal mondo e immergersi in questo lavoro, che forse è più una passione, mi ha aiutato tantissimo. Questa tesi va a coronare un periodo intenso, pieno di alti e bassi, ma tremendamente affasciante quale il Dottorato di Ricerca. Questo periodo mi ha insegnato moltissimo sia dal punto di vista umano che tecnico, permettendomi di crescere da un punto di vista professionale ed umano in maniera profonda. Questo periodo di tre anni mi ha fatto capire che la Ricerca, con tutti i suoi diffetti, è un'arte mervigliosa, me ne ha fatto innamorare sempre di più, giorno dopo giorno, fino al voler inseguire il sogno di farla diventare la mia Professione. Devo quindi ringraziare tutte le persone che mi sono state vicine in questo periodo di apprendimento ed innamoramento.

Grazie Renato per essere sempre stato il Professore al quale si può dare del *tu*, e per essere stato capace di stimolare la mia fantasia nella ricerca e al contempo essere empatico e sempre pronto ad ascoltarmi nei momenti in cui i dubbi, anche di vita professionale, non erano pochi.

Grazie Professor Denegri, perchè spero un domani di diventare un Professore con la *P* maiuscola come è lei, capace di essere fonte di ispirazione come lei è stato con me.

Grazie Andrea, perchè hai sempre saputo essere capace di organizzare la nostra vita lavorativa, scandire i tempi, per le belle idee di lavori scientifici che hai avuto e per esserti occupato di tutta la gestione di questo periodo.

Grazie Professor Invernizzi, le sarò sempre debitore per avermi fatto conoscere il NICES quel giorno ormai lontano in cui le chiesi di poter fare la tesi triennale con lei.

Grazie ai Professori Davide Poli e Marco Merlo per la preziosa revisione della tesi di dottorato.

Grazie Ale, Dami, Dani, Ale BCC, Manu, Massi e Giacomo per essere stati, e essere ancora, colleghi incredibili ed amici preziosi.

Grazie Carletto, per i caffè, per le belle chiacchierate fatte, per essere stato ed essere ancora una guida dentro al DITEN, perchè mi hai sempre tenuto con i piedi per terra, ricordandomi che non si vive di soli numeri e alle 13 bisogna pranzare con il tuo "*Ingegnè che fa? Lei non mangia oggi?*". Ti voglio bene e forza Napoli.

Grazie Massimo ed Emanuela per tutti i pranzi spensierati insieme, e Massimo stai pur certo che per ancora un pò di anni verrò a prendere il caffè da te, magari rubandoti un pezzetto di focaccia.

Grazie a tutti i voi di ABB ed in particolare a Pietro, Andrew e Michele, mi avete insegnato così tante cose, e permesso di assorbire in maniera così profondamente bella i vostri insegnamenti sia tecnici che di vita professionale che saranno un bagaglio che porterò con me tutta la vita.

Grazie a tuti voi ragazzi, amici di sempre, amici per sempre. Abbiamo condiviso tutto, momenti belli e momenti di grande dolore, siete una delle mie certezze.

Grazie a tutti voi Famiglia, mi avete permesso di potermi dedicare serenamente alla mia passione dello studio durante questi otto anni bellissimi, vi devo praticamente tutto. Ovviamente un ringraziamento speciale va al piccolo Tommy, tu non sai quanto hai colorato la nostra vita, ma ti spiegherò tutto quando sarai grande.

Grazie a tutte le belle persone che ho conosciuto nella palestra MSA, ed in particolare a te Dani, durante un periodo buio le tue lezioni su Zoom erano la salvezza sotto più punti di vista. Grazie coach!

Grazie a tutta la famiglia Ceccarelli, il vostro bellissimo calore tipicamente partenopeo è stato ed è un dono prezioso.

Ed infine grazie alla persona più speciale che ha condiviso con me buona parte di questo percorso, che sei tu Vale. Con te ho imparato molto, e mi hai fatto sempre sentire l'uomo più fortunato del mondo ad averti vicino, vorrei dire mille parole, ma nelle parole di questa tesi, in cui forse sono stato capace di racchiudere un buon lavoro, non sono capace di intrappolare la bellezza di averti avuto vicino in questo mio cammino, nel festeggiare insieme per un paper accettato, per avermi sempre ascoltato con attenzione mentre ti raccontavo con il mio, a volte eccessivo, entusiasmo questa parte del mio mondo, e per esserci stata anche nei momenti di sconforto, supportandomi con la tua delicatezza e la tua unica sensibilità. Il ringraziamento migliore te lo farò il giorno che discuterò questa tesi, perchè i miei occhi si faranno strada tra tutte le persone che avrò davanti alla ricerca dei tuoi, alla ricerca di quel supporto che non mi hai mai fatto mancare. *Thank you Valentina.*

# Contents

# List of Figures

# List of Tables

# Abbreviations

| | |
|---|---|
| **DER** | **D**istributed **E**nergy **R**esources |
| **EES** | **E**lectrical **E**nergy **S**ysytems |
| **RES** | **R**enewable **E**nergy **S**ources |
| **MG** | **M**icro**G**rid |
| **PCC** | **P**oint of **C**ommon **C**oupling |
| **EMS** | **E**nergy **M**anagement **S**ystem |
| **PLL** | **P**hase **L**ocked **L**oop |
| **GSM** | **G**rid **S**upport **M**ode |
| **VGM** | **V**irtual **G**enerator **M**ode |
| **BESS** | **B**attery **E**nergy **S**torage **S**ystem |
| **AVR** | **A**utomatic **V**oltage **R**egulator |
| **SDG** | **S**ynchronous **D**iesel **G**enerator |
| **GFM** | **G**rid **F**orming **M**ode |
| **CLF** | **C**urrent **L**imiting **F**actor |
| **LVRT** | **L**ow **V**oltage **R**ide **T**hrough |
| **PID** | **P**roportional **I**ntegral **D**erivative |

# Chapter 1

# Introduction

## 1.1 Virtual Synchronous Generator: State of Art

In the recent years the electricity energy scenario has been the protagonist of impressive changes due to the strong growth of Distributed Energy Resources (DERs) including, among others, microturbines, Electrical Storage Systems (ESS), fuel cells and Renewable Energy Sources (RES), such as photovoltaic and wind generation [1].

This allows the ensuring of better exploitation of RES, increasing system efficiency and a lower environmental impact of energy production. On the other hand, many new technical issues have to be tackled, such as the management of inverse power flows, the variability of RES generation and the possible deterioration of power quality.

However, the possible aggregation of local generation and loads have given rise to the generalisation of the concept of Microgrid (MG), i.e. an electricity distribution system containing loads and DERs that can be operated in a controlled, coordinated way either while connected to the main power network or while islanded. When an MG operates in a grid-connected configuration, the interface with the main distribution grid is achieved via a Point of Common Coupling (PCC).

MGs are usually operated with a hierarchical control architecture divided into three levels, namely tertiary, secondary, and primary regulation.

The tertiary control level is the so-called Energy Management System (EMS) and this defines the production of the dispatchable units that minimises the MG operational cost or other environmental/technical indicators. The EMS operates on long time frames (e.g., 15 minutes or longer). The two lower layers have different aims depending on whether they manage islanded or grid-connected MGs. In the grid-connected mode, primary and secondary control levels are expected to *i*) perform voltage or frequency regulation in order to support the grid and *ii*) to make the DERs provide the active and reactive powers ordered by the EMS, while variation in load demands is satisfied by the main distribution grid.

Islanded operation, on the other hand, is much more challenging since the MG controllers need to provide suitable voltage and frequency regulation and, of course, guarantee the balance between production and demand. In this framework, the MG control system needs to replicate the hierarchical structure of the main power grid but on a smaller scale including a primary layer (that guarantees active and reactive power balance) and a secondary one (aiming at restoring suitable values for the frequency and voltages.

Achieving the goals of primary regulation becomes even more challenging if all the DERs are connected to the MG distribution network by means of power electronic devices (usually referred to as no-inertia MGs). Primary control is typically a communication-less control layer; it is normally implemented in a decentralized manner in order to properly control voltage and frequency and/or active and reactive powers [2]. Inner control loops are adopted to regulate the output voltage and to control the current while maintaining the system stable. Considering the normative aspect, IEEE Std.1547 [3] clearly defines the inverter's primary control functionalities that can be essentially clustered in two operational configurations (*i*) Grid-Following Operation or Grid Support Mode (GSM) and (*ii*) Grid-Forming Operation. In GSM, the inverter is controlled as a current source in which the main control goals are to supply the load connected to the MG and to participate in frequency and voltage support [4, 5]; for these reasons, GSM is the typical configuration in grid-connected state. Just to propose some examples of BESS around the world used for Grid Support, it is possible to mention that the electricity utility installed a 3 MW/750 kWh lead–acid battery system in Alaska, as spinning reserve, in order to mitigate the curtailment of energy from wind farms and to provide frequency response within 0.5 s [6]. In Illinois, a 31.5 MW battery storage was located near a wind farm project and solar plant to provide fast frequency response as well as other ancillary services. Similarly, Australia's energy market operator contracted Tesla's 100 MW/129 MWh lithium-ion battery in Hornsdale. This battery was considered the largest ESS when it was built and it provides frequency control and participates in the ancillary services market [7]. In Germany, it was recognized that BESS can play an active role in providing fast frequency response: in 2017, BESS systems provided about 200 MW of Frequency Containment Reserve, about 31% of the market. In Italy, to date, only significant thermal and programmable hydroelectric plants (i.e., larger than 10 MVA) compulsory provide ancillary services. On the contrary, Grid-Forming Operation is typically exploited in islanded mode where the inverter can be either the voltage and frequency master (stand-alone mode) or allow parallel operations with other DERs.

An obvious consequence of this high penetration of inverter-interfaced DERs is the reduction of total inertia and damping because most of the proposed control methods for Grid-Forming inverters, e.g., droop control methods [8], provides barely any inertia or damping support for the MG. For this reason, one of the most performing primary control technique for Grid-Forming inverters is the Virtual Synchronous Machine or Virtual Generator Mode (VGM) [9], where the control acts on the inverter in order to mimic the dynamical behaviour of a traditional synchronous generator [10–13], virtually adding some inertia and frequency damping to the system and accordingly, improving MG stability [14] and , since inertia response is the result of rotating heavy mass and it is proportional to the rotor speed, the VGM concept can also directly improve the frequency response [15, 16]. In [17–19], the VGM primary control is developed using the complete model of the synchronous generator and this makes the algorithm complex and the controller tuning difficult. Simpler design models for the VGM control are proposed in [20–23], where only the inertial behaviour of a synchronous generator is considered by imposing the swing equation in the primary controller. In [24], a VGM control technique is proposed showing how it can theoretically provide all the required functionalities of Grid-Forming inverters (according to IEEE Std.1547) and also presenting some practical applications of VGM control technique for Battery Energy Storage System (BESS) around the world.

So it is clear that the VGM approach to the converter control is an interesting and challenging field for academic and industrial research and several aspects need to be investigated and need to have reliable and practicable solutions. One of the most interesting field on VGM algorithms is the study of their behaviour during faults and this is meticulously detailed in the following section.

## 1.2 Virtual synchronous generator algorithm during faults: an overview

Today electricity energy production mainly comes from centralized power plants, which thanks to their large rotational inertia, are able to provide the main grid high transient stability and robust performance. However, a large number of DERs connected via inverter can negatively affect the network stability when disturbances and faults occur. The VGM strategy can contribute to the creation of inertia and damping effect and solve the issues related to frequency deviations [25–27]. Moreover, it has been demonstrated that VGM can be integrated with droop characteristic, and thus, such VGM inherited the advantages of droop control, for instance, proper load sharing among parallel-connected DERs. Still, other concerns exist over grid stability under the large DERs penetration. One of the most important concerns is the interrupted/unstable operation in the DERs system due to the effect of transient disturbances on the utility grid [28–30]. Without a proper countermeasure, the whole grid could suffer from a large imbalance between the power supply and power demand. According to several grid codes, the requirements for Low Voltage Ride Through (LVRT), state that for fault of a given duration and with voltage drop larger than a specific value of rated voltage, the DER converters have to remain connected and guarantee the following requests:

- The converter has to limit the output current when a fault occurs both in GSM and VGM operating modes;
- Ride-through behaviour during low voltage conditions is required;
- When the converter is in islanded configuration, it must be able to restore the voltage level of the pre-fault operating point;
- When the converter is connected to an external grid or to a diesel generator, it has to resynchronize when the fault is cleared.

This indicates that in such an event of a fault, the DER converter must not be tripping. Nevertheless, unlike a conventional generator, semiconductor switches in the inverter-based DERs system cannot tolerate over-current condition due to their low thermal inertia [31]. Therefore, the fault must be quickly detected to prevent over-current in the inverter and equipment connected to the grid. However, the LVRT ability of VGM based converter has not yet been thoroughly analysed.

For instance, a current restraining method under the balance voltage sag was presented in [32] based on control mode switching; however, it faces a challenge of managing the transition between normal mode and over current mode during and after fault condition, especially against the case of asymmetrical voltage sag, where the current becomes oscillatory under the unbalanced condition. But in this case the proposed VGM algorithm uses active and reactive power references, so there is the need of a PLL to generate current references and for this reason it can not work independently.

In [33], evaluation of voltage sag consequences and current suppressing strategy was conducted for both symmetrical and asymmetrical voltage sags; however, only the case of mild voltage sag (over 0.9 pu) was studied in the presented work. Recently, a grid-connected based DER that uses voltage references provided by VGM to achieve current control via virtual admittance is proposed in [34]. Although the referred control is able to cope with unbalanced faults, since the issue of over-current limiting was not addressed specifically, it is undetermined whether the dynamic response of the method in [34] is quick enough to deal with over current condition.

Another way to deal with over-current limiting in VGM is to use multiple loop control of voltage and current, and the current limiting can be implemented in the inner current control loop by simply limiting current reference as proposed in [35]. However, to ensure stability in all operating conditions, tuning of Proportional–Integral-Derivative (PID) has to be done appropriately, which can be challenging when a number of DERs are connected together. Wind-up and waveform clipping can be also the disadvantages of this method. Furthermore, when multi loop control is connected to another voltage source, the control has a problem with active and reactive power regulators during and after disturbance. Moreover, it is possible to point out that maintaining stability after disturbances and exiting current limiting are other issues for multi loop control.

In the literature, other types of current limiting strategies are proposed, which can be accomplished in the voltage control loop. These current-limiting methods are typically accomplished by reducing the voltage magnitude when the current exceeds a threshold [36] or by a current-limiting PID controller [37]. Adopting these methods in VGM control, however, could lead to another shortcoming, because a complicated strategy to guarantee current limits during fault and the restoring of previous current value can be required.

Considering all these aspects, the aim of this thesis is to present a new VGM algorithm which can guarantee optimal performances in normal operation scenarios and in fault conditions in order to satisfy all grid code requirements. The thesis is organized as follows: Chapter 2 presents the new Virtual Synchronous Generator control algorithm and some simulations carried out with the dedicated simulation software DIgSILENT PowerFactory® to show the correct dynamic behaviour in normal operating scenarios. Then Chapter 3 deals with the modification of the proposed control scheme in order to properly manage symmetrical faults in islanded and grid connected configuration with a particular focus on the resynchronisation problem. Chapter 4 proposes a complete set of simulations in order to deeply discuss the performances obtained in this research field. Overall conclusions and final remarks are reported in Chapter 5.

# Chapter 2

# Virtual Synchronous Generator Control Algorithm

**Brief:** This chapter proposes the design of a comprehensive inverter BESS (Battery Energy Storage System) primary control capable of providing satisfactory performances both in grid-connected and islanded configurations as required by international standards and grid codes, such as IEEE Std. 1547. Such a control guarantees smooth and fast dynamic behaviour of the converter in islanded configuration as well as fast power control and voltage-frequency support in grid-connected mode. The performances of the proposed primary control are assessed by means of Electro Magnetic Transients (EMT) simulations in the dedicated software DIgSILENT PowerFactory®. The simulation results show that the proposed BESS primary control is able to regulate frequency and voltage in Grid-Forming mode independently of the number of paralleled generators. This is achieved adopting a virtual generator technique which presents several advantages compared to the conventional one. Moreover, the proposed control can be switched to Grid Support Mode (GSM) in order to provide fast control actions to allow frequency and voltage support as well as power control following the reference signals from the secondary level.
**Personal contribution:** I developed the control system and performed simulations in the dedicated simulation software.

As explained on Chapter 1, the aim of this chapter is to present a new primary control for BESS converter based on the concept of the virtual synchronous generator, able to guarantee relevant performances in grid-connected and islanded configurations, and more precisely:

- Regulation of frequency and voltage in Grid-Forming mode independently of the number of paralleled generators using the VGM technique in order to mimic the dynamic behaviour of synchronous generators;
- Ability to guarantee MG black-start in Grid-Forming mode;
- Correct active and reactive power sharing in parallel with other DERs;
- Fast control actions in grid-connected mode to allow providing frequency and voltage support (GSM) as well as power control following the reference signals from the secondary level control;
- Synchronization and connection of the BESS to the external main grid or to other DERs in islanded mode with minimum transients.

The results will show that the new primary control proposed in this thesis is also interesting not only from an academic point of view, but also from an industrial one for these aspects:

- The BESS converter is able to work both in VGM and in GSM guaranteeing the possibility to work in parallel with other DERs or to an external main grid;
- The primary control can be switched from Grid-Forming mode to Grid-Support mode and vice versa without converter power interruption;
- Considering the Grid-Support mode, the proposed control is able to provide fast actions to the MG because this functionality is implemented in the primary level and not in the secondary one;
- When the support to the MG is not necessary, the control is able to use control signal coming from the secondary level control in order to satisfy other tasks reported in IEEE Std. 1547 such as State of Charge management, power smoothing, and compliance with power flow constraints imposed at the connection point with the external Main Grid (peak lopping);
- Considering the Grid-Forming operating mode, the proposed VGM technique is a PI-based one, which means that the tuning procedure can be easily managed by operators and not just by control engineers. In summary, all these aspects and the

level of detail in which they have been implemented and presented in this thesis represent the main contribution of the work and a good starting point for actual implementation on industrial controller (which is the final aim of the Hitachi Power Grids/University of Genoa's final goal).

Finally, it is important to highlight that in the present work the DC part of the BESS converter is modelled as an ideal voltage source. This is a common practice when dealing with the converter primary and inner loops control, in fact the fast dynamics involved are not relevant for the State of Charge of the battery. More precisely the primary control level and inner control loops work on the time scales of seconds and milliseconds respectively, and so in these time scales the State of Charge can be considered constant [10].

## 2.1 Primary Control Method Description

The aim of this section is to provide an effective description of the proposed primary level BESS control: as stated before, it can provide a proper BESS converter regulation both in Grid-Forming and Grid-Support operating modes as it will be detailed in the following subsections. As one can see from figure 2.1, the BESS converter has a R-L-C filter at its output ($R_f$, $L_f$, and $C_f$) and the primary control needs some measurements from the field in order to guarantee optimal performances in the two operating modes. In detail, these measurements are active power $P_{meas}^{BESS}$ and reactive power $Q_{meas}^{BESS}$ at the output of the BESS converter, the RMS value of the controlled voltage $V_{meas}$, the controlled frequency $f_{meas}$ and phase angle $\theta_{meas}$ coming from a Phase Locked Loop (PLL) control function synchronized at the connection bus to the MG. The output of the BESS primary control are the reference voltages $v_{ref}^{\alpha}$ and $v_{ref}^{\beta}$ in the $\alpha-\beta$ stationary reference frame for the Grid-Forming operating mode and the $d$-$q$ reference frame currents $i_{d,ref}^{GSM}$ and $i_{q,ref}^{GSM}$ for the Grid-Support operating mode. In order to generate the control signals for the BESS converter $v_{d,ref}^{inv}$ and $v_{q,ref}^{inv}$, voltage and current control loops are mandatory, more precisely when the Grid-Forming operating mode is required, voltage and current control loops are used in a cascade configuration, while in Grid-Support operating mode only the current control loop is required. In the next subsection, VGM and GSM techniques as well as voltage and current control loops are described in detail.

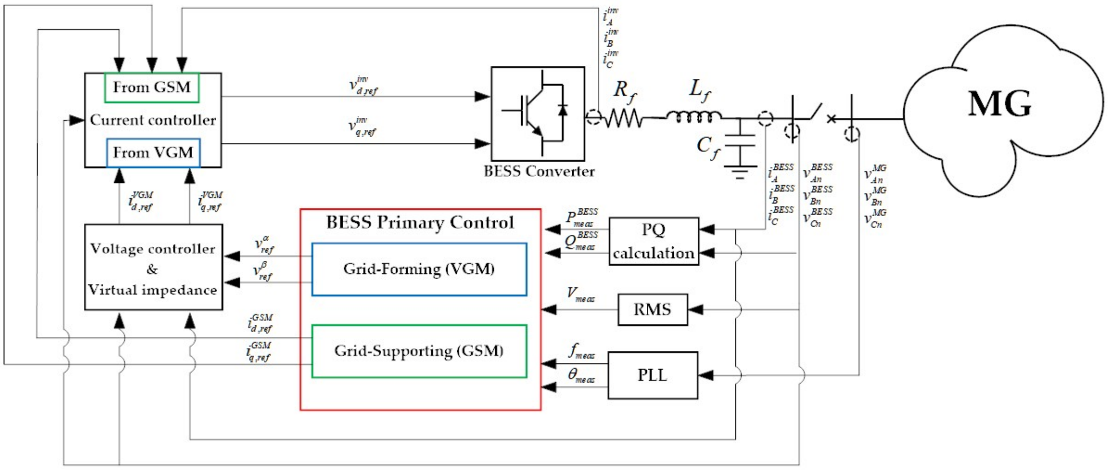

FIGURE 2.1: Proposed BESS (Battery Energy Storage System) primary control scheme.

### 2.1.1 Grid-Forming Operating Mode: VGM

Considering the Grid-Forming operating mode, the VGM technique presented in [24] is exploited and its control block diagram is reported in figure 2.2 where AVR (Automatic Voltage Regulator) and Rotor Flux Model make the reactive power/voltage magnitude similar to that of a synchronous generator. More precisely, the Rotor Flux Model, modelled as an integrator with a gain $K_{\Psi}$, responds to the reactive power $Q^{BESS}_{meas}$ at the output of the inverter with an initial voltage variation of $V^{VGM}_{ref}$ to model the machine flux variation through the following virtual electrical dynamic equation:

$$\frac{dV^{VGM}_{ref}}{dt} = K_{\Psi}\left(Q^{BESS}_{AVR} - Q^{BESS}_{meas}\right) \tag{2.1}$$

where $Q^{BESS}_{AVR}$ is the control action of the BESS converter AVR. Then, the AVR brings the RMS voltage at the output of the inverter $V_{meas}$ back to its set point $V_{set}$. Similarly, the Inertia model and the Frequency Governor make the VGM similar to a synchronous generator active power/frequency dynamics. In particular, the Inertia model, described by an integrator and by two gains $K_H$ for the inertia itself and $K_d$ for the damping effect, reacts to the active power $P^{BESS}_{meas}$ at the output of the inverter, drawing energy from the inertia and slowing the rotational speed of the virtual generator $\omega^{VGM}_{ref}$ using the following virtual mechanical dynamic equation:

$$\frac{d\omega^{VGM}_{ref}}{dt} = K_H\left(P^{BESS}_{GOV} - P^{BESS}_{meas} - K_d\omega^{VGM}_{ref}\right) \tag{2.2}$$

where $P_{GOV}^{BESS}$ is the regulating action of the BESS converter Governor. Then, the Governor brings back the frequency $f_{meas}$ to its set point $f_{set}$. To allow operation in parallel with other sources, the control includes droop factors $m_{droop}$ and $n_{droop}$ to achieve power sharing control in the steady state; while for stand-alone operation, the droop coefficients are usually set to zero. Then, in order to guarantee the black-start capability [38] of the MG using the BESS, two different selectors are implemented in the control diagram:

- If the measured RMS voltage $V_{meas}$ is zero, the primary control is able to understand the necessity to provide a black-start procedure; so, imposing the logic signal named *Bl-St* equal to 1, the VGM channel is bypassed and the MG is energized using a ramp voltage reference $V_{ref}^{Bl-St}$ and the rated angular frequency $\omega_n$.
- When the voltage reaches a specific percentage $k_{\%}$ of the rated voltage $V_n$, the VGM control channel is activated (reset of the control integrators) and the selectors switch to the VGM control actions $V_{ref}^{VGM}$ and $\theta_{ref}^{VGM}$.

Finally, the control actions are transformed in the $\alpha - \beta$ stationary reference frame. As a final remark, it is worth pointing out that the tuning procedure of the VGM control is based on a "trial and error" strategy due to the intrinsic simplicity of the proposed primary controller. For example, the inertia parameter $K_H$ of the virtual generator is set in order to have a precise frequency dynamic after an active power step. Then, the governor parameters are set in order to guarantee a desired time response.

### 2.1.2 Grid-Support Operating Mode: GSM

Considering now the grid-connected operating mode, the proposed control must provide fast control actions to allow frequency and voltage support (GSM-$fV$) as well as power control following the reference signals from the secondary level control (GSM-$PQ$). To meet these control requests, the block diagram in grid-connected mode is depicted in 2.3.

In grid-connected mode, the BESS inverter is controlled starting from the measurements of frequency and voltage at the inverter output, i.e., $f_{meas}$ and $V_{meas}$, respectively. Based on an error between measurements and respective set points, it is possible to carry

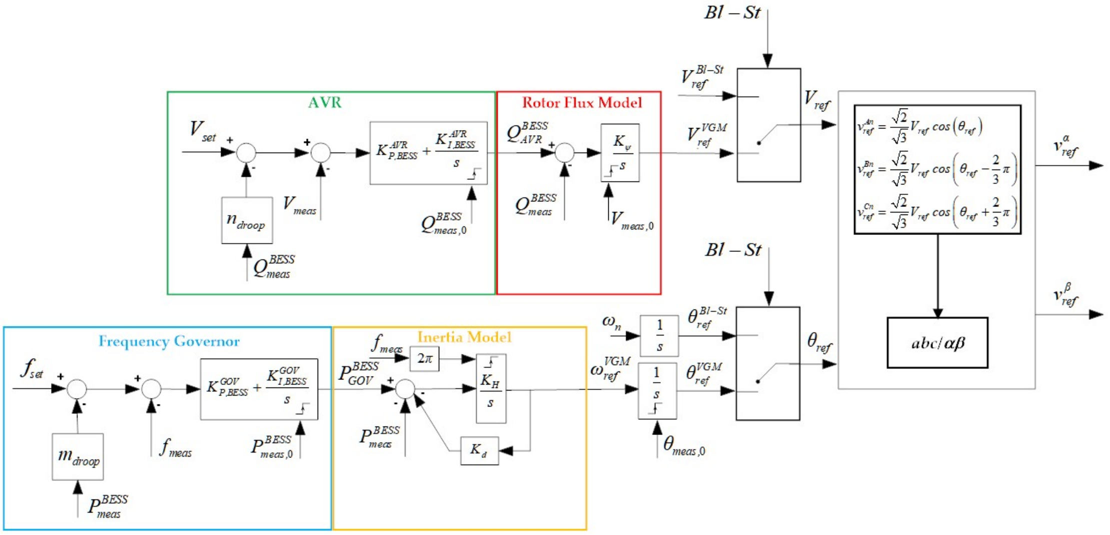

FIGURE 2.2: Proposed VGM (Virtual Generator Mode) control model for Grid-Forming operating mode.

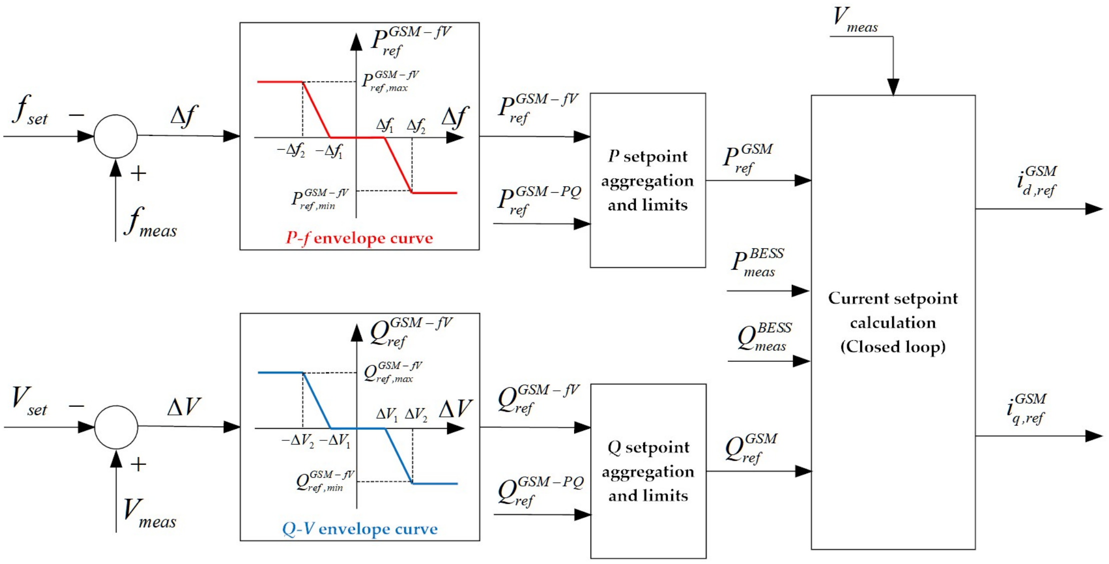

FIGURE 2.3: Proposed GSM (Grid Support Mode) control diagram in grid-connected operating mode.

out the target values of active and reactive powers $P_{ref}^{GSM-fV}$ and $Q_{ref}^{GSM-fV}$ through user-defined *P*-*f* envelope curve and *Q*-*V* envelope curve, respectively. Considering, for example, the *P*-*f* envelope curve, it is described by maximum ($P_{ref,max}^{GSM-PQ}$) and minimum ($P_{ref,min}^{GSM-PQ}$) active power references and by threshold frequency errors $\pm\Delta f_1$ and $\pm\Delta f_2$. The same characterization is done for the *Q*-*V* envelope curve. As stated before, the control also gives the possibility to track the reference values coming from the secondary level regulation, i.e., $P_{ref}^{GSM-PQ}$ and $Q_{ref}^{GSM-PQ}$, so the two blocks “P setpoint aggregation and limits” and “Q setpoint aggregation and limits” are implemented. Then, the *d*-*q* axis currents set points $i_{d,ref}^{GSM}$ and $i_{q,ref}^{GSM}$ are generated by closed-loop controllers which use the voltage measurement $V_{meas}$. Then, they are processed by the BESS inverter Current controller as depicted in figure 2.1.

### 2.1.3 Voltage and Current Inner Control Loops for *L*-*C* Filter

In this subsection, the inner control loops of the BESS converter are presented in order to provide a detailed description of the entire control system. Voltage control loop is depicted in figure 2.4, and as one can see, it is based on PI regulators described by proportional gain $K_{PV}$ and integral gain $K_{IV}$. Its main control objective is to regulate the output voltage of the inverter by minimizing the errors between the references $v_{d,ref}^{BESS}$, $v_{q,ref}^{BESS}$ and the measurements $v_d^{BESS}$, $v_q^{BESS}$. The outputs of the voltage controller are the inverter output current references $i_{d,ref}^{VGM}$ and $i_{q,ref}^{VGM}$. The Park transform adopted is the following:

$$K(\theta_p) = \frac{2}{3}\begin{bmatrix} \cos(\theta_p) & \cos\left(\theta_p - \frac{2}{3}\pi\right) & \cos\left(\theta_p + \frac{2}{3}\pi\right) \\ -\sin(\theta_p) & -\sin\left(\theta_p - \frac{2}{3}\pi\right) & -\sin\left(\theta_p + \frac{2}{3}\pi\right) \\ \frac{1}{2} & \frac{1}{2} & \frac{1}{2} \end{bmatrix} \tag{2.3}$$

In order to decouple the *d*-*q* axis in the voltage controller it is necessary to insert some feed-forwards actions; considering the voltage-current relation for the filter capacitor $C_f$ below:

$$C_f \frac{dv_{ABC}^{BESS}}{dt} = i_{ABC}^{inv} - i_{ABC}^{BESS} \tag{2.4}$$

it is possible to perform the Park transformation as follows:

$$K(\theta_p) C_f \frac{dK^{-1}(\theta_p) v_{dq0}^{BESS}}{dt} = K(\theta_p)\left(i_{ABC}^{inv} - i_{ABC}^{BESS}\right) \tag{2.5}$$

and after some calculations, it is possible to write:

$$C_f \frac{dv_{dq0}^{BESS}}{dt} + \omega_n C_f \begin{bmatrix} 0 & -1 & 0 \\ 1 & 0 & 0 \\ 0 & 0 & 0 \end{bmatrix} v_{dq0}^{BESS} = i_{dq0}^{inv} - i_{dq0}^{BESS} \tag{2.6}$$

and consequently:

$$C_f \frac{dv_d^{BESS}}{dt} = i_d^{inv} - i_d^{BESS} + \omega_n C_f v_q^{BESS} \tag{2.7}$$

$$C_f \frac{dv_q^{BESS}}{dt} = i_q^{inv} - i_q^{BESS} - \omega_n C_f v_d^{BESS} \tag{2.8}$$

Considering equations (2.7) and (2.8) it is possible to write the two feed-forward actions $i_{ff,d}$ and $i_{ff,q}$ for the two regulating channels:

$$i_{ff,d} = i_d^{BESS} - \omega_n C_f v_q^{BESS} \tag{2.9}$$

$$i_{ff,q} = i_q^{BESS} + \omega_n C_f v_d^{BESS} \tag{2.10}$$

Moreover, Virtual Impedance strategy is added to the voltage control loop through algebraic manipulation of the $\alpha - \beta$ voltage reference signals coming from primary controller as follows:

$$v_{ref,v}^{\alpha} = v_{ref}^{\alpha} - \left(R_v i_{\alpha}^{BESS} - X_v i_{\beta}^{BESS}\right) \tag{2.11}$$

$$v_{ref,v}^{\beta} = v_{ref}^{\beta} - \left(R_v i_{\beta}^{BESS} + X_v i_{\alpha}^{BESS}\right) \tag{2.12}$$

with $R_v$ and $X_v$ being virtual resistance and reactance, respectively. This modification enables the output impedance to be set (by parameters, or adaptively) and this is usually made predominantly inductive to ensure a strong coupling between active power and frequency, a strong coupling between reactive power and voltage and an inherent decoupling between these two relationships, even in LV MG.

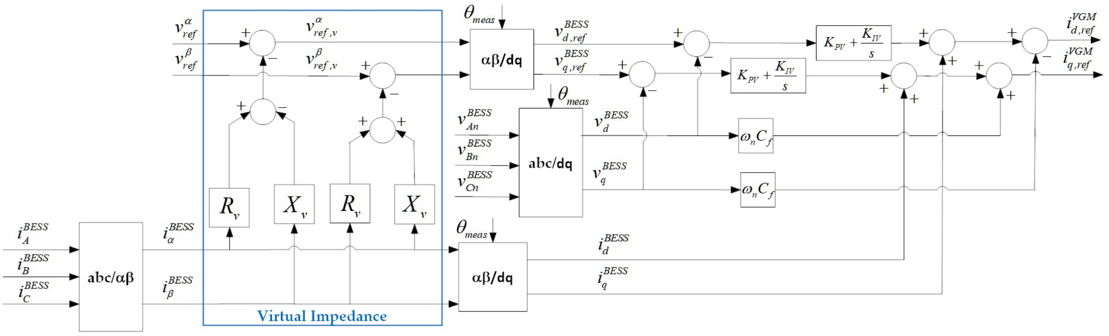

Figure 2.4: Voltage controller for BESS converter.

Current control loop is instead depicted in figure 2.5: due to the fact it is used not only in VGM, but also in GSM operating mode, two selectors are implemented in order to choose the d-q current references coming from the VGM ($i_{d,ref}^{VGM}$ and $i_{q,ref}^{VGM}$) or from the GSM ($i_{d,ref}^{GSM}$ and $i_{q,ref}^{GSM}$). The current controller is based on PI regulators described by proportional gain $K_{PC}$ and integral gain $K_{IC}$ and it acts on the system in order to control the converter output current by minimizing the errors between the references and the measured current described by $i_d^{inv}$ and $i_q^{inv}$. The outputs of the current controller are the inverter voltage modulation signals in the d-q reference frame $v_{d,ref}^{inv}$ and $v_{q,ref}^{inv}$. In order to implement feed-forward actions for the channels decoupling the first step is to write the Kirchhoff law for the filter:

$$L_f \frac{di_{ABC}^{inv}}{dt} = v_{ABC}^{inv} - R_f i_{ABC}^{inv} - v_{ABC}^{BESS} \tag{2.13}$$

performing the Park transform as follows:

$$K(\theta_p) L_f \frac{dK^{-1}(\theta_p) i_{dq0}^{inv}}{dt} = K(\theta_p) \left( v_{ABC}^{inv} - R_f i_{ABC}^{inv} - v_{ABC}^{BESS} \right) \tag{2.14}$$

and after some calculations as done for the voltage controller is possible to write:

$$L_f \frac{di_d^{inv}}{dt} = v_d^{inv} - Rf i_d^{inv} - v_d^{BESS} + \omega_n L_f i_q^{inv} \tag{2.15}$$

$$L_f \frac{di_q^{inv}}{dt} = v_q^{inv} - Rf i_q^{inv} - v_q^{BESS} - \omega_n L_f i_d^{inv} \tag{2.16}$$

Considering equations (2.15) and (2.16) it is possible to write the two feed-forward actions $v_{ff,d}$ and $v_{ff,q}$ for the two regulating channels:

$$v_{ff,d} = v_d^{BESS} - \omega_n L_f i_q^{inv} \tag{2.17}$$

$$v_{ff,q} = v_q^{BESS} + \omega_n L_f i_d^{inv} \tag{2.18}$$

## 2.2 DIgSILENT PowerFactory® Model for Testing

### 2.2.1 Synchronous Diesel Generator Model for Paralleling Operation

As stated in the introduction section, the proposed BESS control is implemented in the widely used power system simulator DIgSILENT PowerFactory® in order to have reliable and high-fidelity simulation results. Due to the fact that in Grid-Forming operating mode the BESS inverter must be the voltage/frequency master in stand-alone

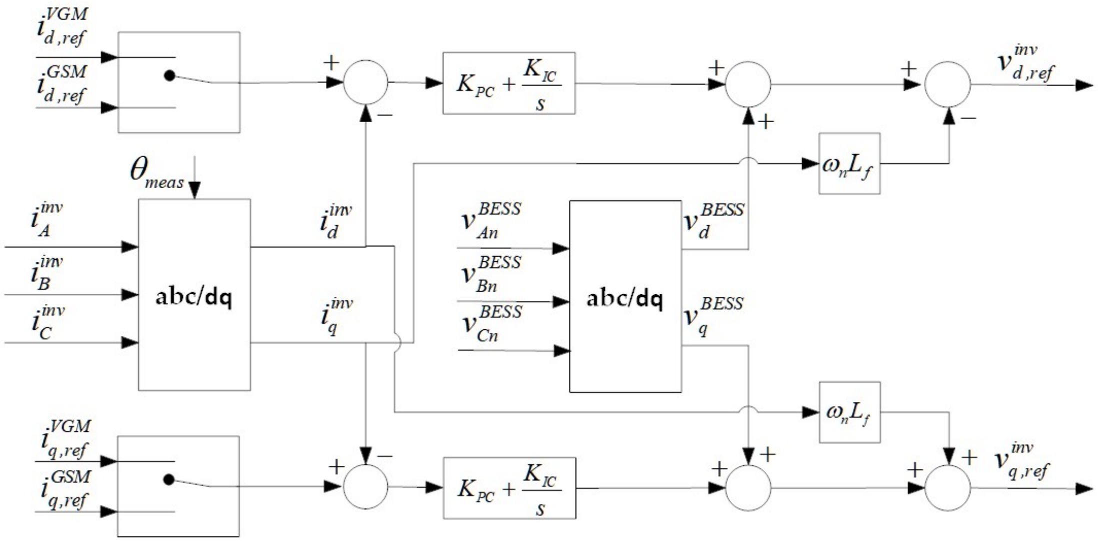

FIGURE 2.5: Current controller for BESS converter.

configuration and must allow parallel operations with other DERs, a Synchronous Diesel Generator (SDG) model has been included in the simulated power system; the SDG model is briefly described below starting from the conceptual model depicted in figure 2.6. As one can see, it consists of three main elements: Synchronous Generator EMT model is available from PowerFactory library [39], while the Diesel Engine with Governor and Excitation System models are depicted in figure 2.7 and figure 2.8, respectively.

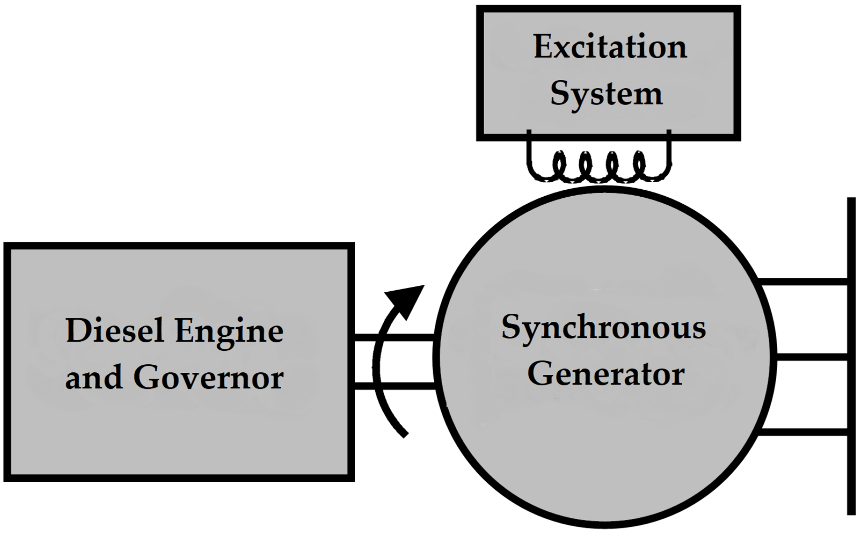

FIGURE 2.6: Synchronous Diesel Generator (SDG) conceptual model.

The frequency-active power regulation of the SDG is realized using a Governor whose inputs are the electrical speed $f_{SDG}$ and the active power measurement $P_e^{SDG}$. Droop coefficient $f_{droop}$ is implemented to guarantee the correct power sharing in islanded mode

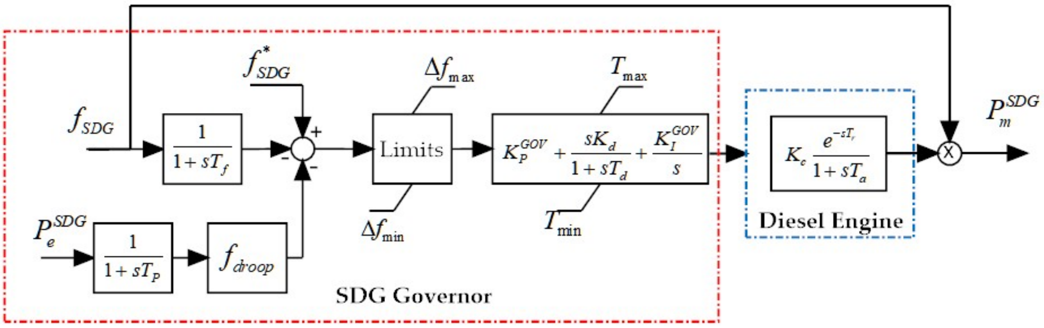

FIGURE 2.7: Diesel Engine and Governor model for the SDG.

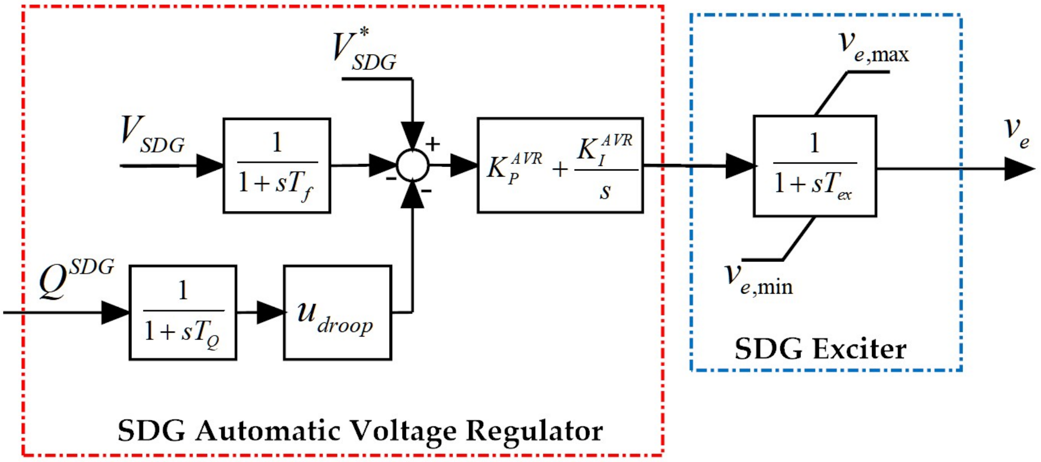

FIGURE 2.8: Exciter and Automatic Voltage Regulator model for the SDG.

and in parallel with the BESS unit. A PID regulator generates the torque input for the diesel generator, which is modelled by the combustion gain $K_c$, the fuel dynamics time delay $T_r$, and by a first order dynamic where $T_a$ models the engine fuel system time constant. The voltage-reactive power regulation is performed by an AVR where RMS voltage and reactive power measurements are the inputs and where the droop logic is implemented by the use of the coefficients $u_{droop}$. The AVR output is then processed by the exciter, which is modelled by a first order dynamic with time constant equal to $T_{ex}$ [40].

### 2.2.2 Test MG Layout and Parameters

In order to test the performances of the proposed BESS primary control, the test case MG reported in figure 2.9 is used. The main element in the MG is the BESS unit, which is connected to the MG via inverter. The storage component of the BESS is modelled as ideal DC voltage source and so its internal dynamics are neglected. Similarly, the inverter model, provided by DIgSILENT PowerFactory® library, is considered as an ideal controlled AC voltage source. The inverter is interfaced to the MG with a R-L-C filter modelled by the parameters $R_f$, $L_f$ and $C_f$, respectively, and with a unitary-ratio transformer $T_{BESS}$. The SDG exploits the DIgSILENT PowerFactory® synchronous generator model and it is connected to the MG Point of Common Coupling (PCC) using longitudinal impedance $\dot{Z}_{SDG}$. An external grid is connected to the MG through a medium voltage/low voltage transformer $T_{MV-LV}$ in order to test the Grid support and the paralleling functionalities. Load centre bus is connected to the PCC with a line $\dot{Z}_{line}$ while $Load_1$ is connected to Load centre bus using a cable $\dot{Z}_{cable}$. MG data are reported in table 2.1.

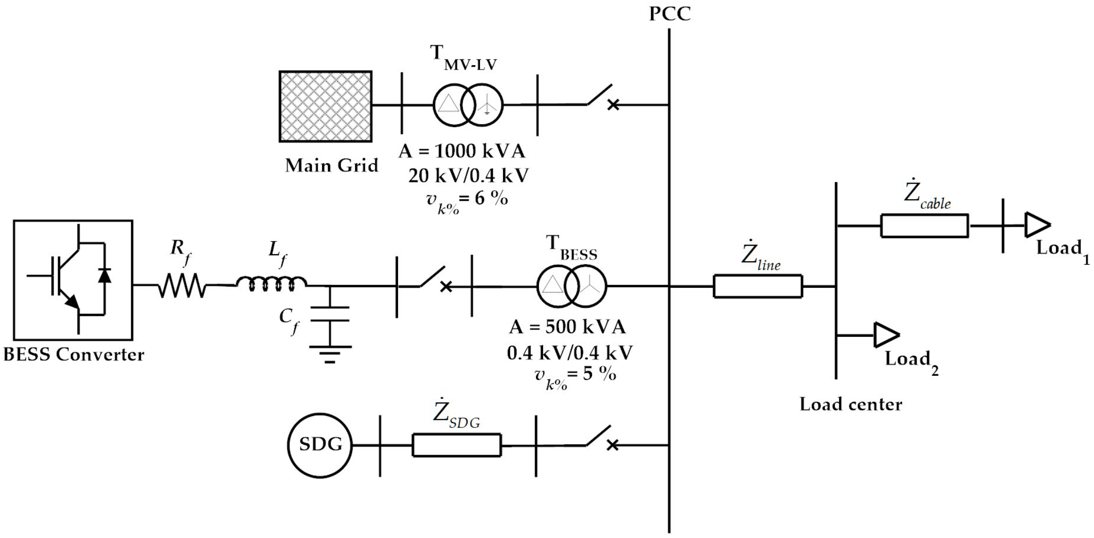

FIGURE 2.9: Test case microgram (MG) one-line diagram.

| **BESS Data** | **SDG Data** | **Load Data** | **Impedances at f$_n$** |
|---|---|---|---|
| $A_{BESS}$=500 kVA | $A_{SDG}$=1250 kVA | $P_n(Load_1)$=300 kW | $\dot{Z}_{SDG}$ = 0.007+j0.0008 Ω |
| $V_n$=400 V (AC-side) | $\cos\phi_n$=0.8 | $Q_n(Load_1)$=100 kVAr | $\dot{Z}_{line}$ = 0.014+j0.0016 Ω |
| $f_n$=50 Hz | $V_n$ 400 V | $P_n(Load_2)$=50 kW | $\dot{Z}_{cable}$ = 0.0037+j0.004 Ω |
| $R_f$=0.044 Ω | $f_n$ 50 Hz | $Q_n(Load_2)$=0 kVAr | |
| $L_f$=0.088 mH | | | |
| $C_f$=50 $\mu$F | | | |

TABLE 2.1: Test case microgrids (MG) parameters.

## 2.3 Simulations Results

### 2.3.1 Black Start and Load Step in a Stand-Alone Configuration

This is the first functionality that the BESS primary control has to satisfy. IEEE 1547.4 Std. gives a clear definition of the black-start, i.e., the ability to start local generation with no external source of power. During this phase, the main grid and the diesel generator are disconnected from the MG and no load is connected. As described in the previous section, the BESS is controlled in Grid-Forming operating mode and the VGM control is bypassed imposing voltage and frequency reference signals. As one can see from 2.10, the three-phase voltages at the controlled node of the MG perfectly follow the ramp reference signal $V_{ref}$, and the zoomed box highlights the correct dynamic behaviour when the VGM control channel is activated with the switch of $V_{ref}$ from $V_{ref}^{Bl-St}$ to $V_{ref}^{VGM}$ and of $\theta_{ref}$ from $\theta_{ref}^{Bl-St}$ to $\theta_{ref}^{VGM}$ and with the reset of the integrators of the VGM control. When the black-start procedure ends (the ramping time is defined through a parameter and in this case it was chosen to last 1 s), a load step event is implemented in the simulation in order to test the dynamic response of the BESS in VGM mode in terms of voltage and frequency in a stand-alone configuration. As one can see from figure 2.11, after the load step occurred at $t = 4s$, frequency and voltage

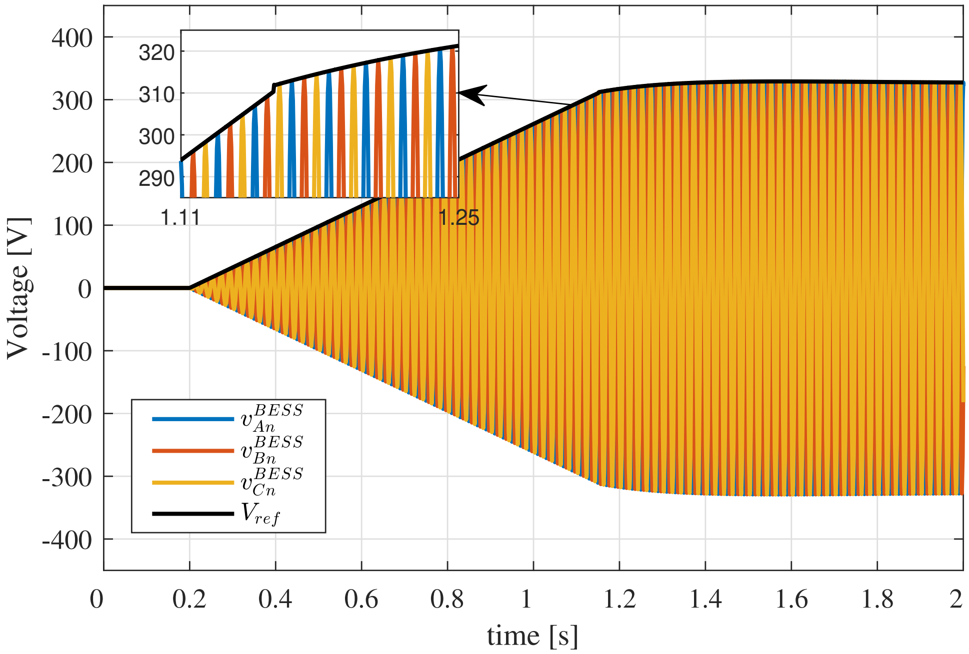

FIGURE 2.10: Controlled BESS bus voltage time profiles during black-start procedure.

have a time profile in which it is possible to note the effects of the inertia model and of the governor regulating action for the frequency and of rotor flux model and AVR regulating action for the voltage. In this simulation, the droop coefficient $m_{droop}$ and $n_{droop}$ are equal to zero because the power sharing functionality is not required in a stand-alone configuration, and for this reason, after the transient, frequency and voltage return to their rated values (namely 50 Hz for the frequency and 400 V for the voltage). Moreover, it is possible to notice the effect of the virtual impedance implemented in the voltage control loop of the converter; in fact, in the final steady state, the reference value $V_{ref}^{VGM}$ is greater than the controlled inverter output voltage $V_{meas}$. Finally, figure 2.12 reports the active and reactive powers' time profile after load step contingency ($P_{load}$ and $Q_{load}$), and it is possible to see how the BESS is able to supply the load power request with a fast and smooth dynamic response.

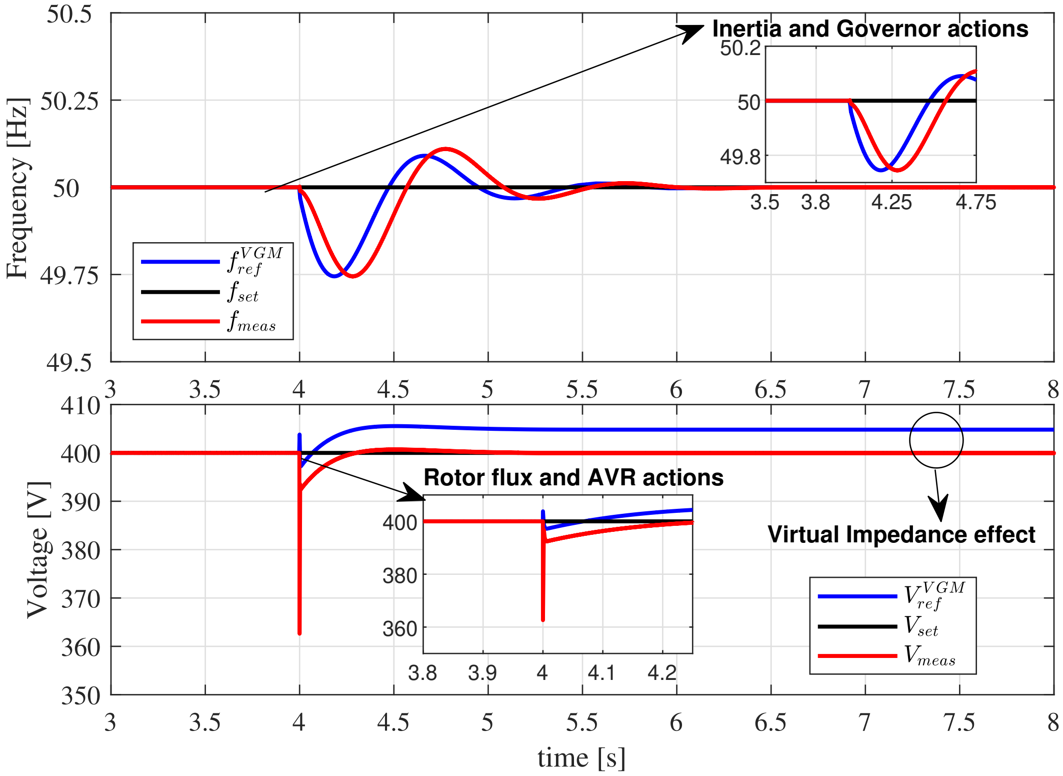

FIGURE 2.11: Frequencies (first panel) and RMS (Root Mean Square) voltages (second panel) time profile during load step in stand-alone configuration.

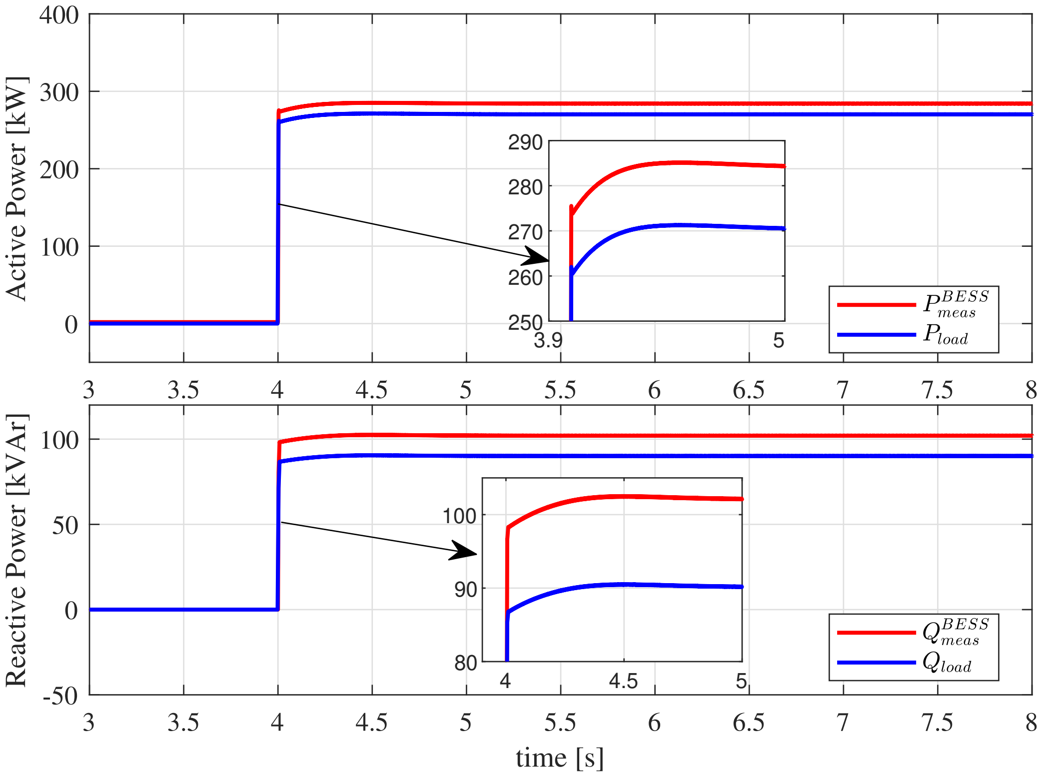

FIGURE 2.12: Active (first panel) and reactive (second panel) powers' time profile during load step in stand-alone configuration.

### 2.3.2 VGM Operating Mode With Setpoints Variation

As stated in the introduction, when the VGM operating mode is activated, the BESS converter has to provide fast regulation of voltage and frequency. In these simulations, the main grid is connected to the MG and the load request is totally fed by the main grid. The BESS converter is then connected to the MG in Grid-Forming operating mode without active and reactive powers production. In order to highlight the advantages of the proposed VGM control technique, a comparison with the conventional droop control for Grid-Forming operating mode is shown. When this conventional control technique is adopted, all the macro blocks of the proposed controller (i.e., the AVR, the Rotor Flux Model, the Governor and the Inertia Model) are bypassed avoiding all the dynamics introduced by the virtual generator scheme. So, the control signals $V_{ref}$ and $\theta_{ref}$ with the conventional droop control technique become:

$$\begin{cases} V_{ref} = V_{set} - n_{droop} Q_{meas}^{BESS} \\ \theta_{ref} = 2\pi \int \left[ f_{set}(s) - m_{droop} P_{meas}^{BESS}(s) \right] ds \end{cases} \tag{2.19}$$

The first simulation results are depicted in figure 2.13: in this scenario, the frequency setpoint $f_{set}$ is fixed at the MG rated value, while the voltage setpoint $V_{set}$ changes from 400 V to 410 V at $t = 2s$ then from 410 V to 390 V at $t = 6s$ and finally from 390 V to 400 V at $t = 10s$. As one can see, the set point is correctly followed by the controlled RMS voltage $V_{meas}$ with good time response and minimum overshoots (the droop parameters $m_{droop}$ and $n_{droop}$ are equal to zero in this simulation since there are no other DERs to share the load request). The second panel shows instead reactive powers time profile, and it is possible to see that an increase/decrease of the controlled voltage corresponds to a BESS converter reactive power production/absorption, which is balanced by the main grid, due to the strong coupling between voltage and reactive power. Considering the comparison, the conventional droop control has a faster time response because there is no effect of the virtual generator dynamics, but it has two main drawbacks: (*i*) voltage steady-state errors due to the absence of an AVR in the droop control to compensate the effect of the virtual impedance implemented in the voltage controller (the greater the output current of the BESS converter, the greater the voltage steady-state error, as apparent in equations (2.11) and (2.12)) and (*ii*) large initial overshoots in the reactive power time profiles as detailed in figure 2.14. Then, in order to test the possibility of managing the BESS converter active power production by changing the frequency setpoint, in the second scenario the voltage setpoint $V_{set}$ is fixed to the rated value while the frequency setpoint $f_{set}$ changes from 50 Hz to 50.1 Hz V at $t = 2s$, then from 50.1 Hz to 49.9 Hz V at $t = 6s$ and finally from 49.9 Hz to 50 Hz at $t = 10s$. Due to synchronism with Main Grid requirement, the frequency droop factor $m_{droop}$ is activated. As one can see from Figure 15, the frequency setpoint is not tracked (first panel), but varying its value it is possible to correctly manage the BESS active power production (second panel), which is correctly balanced by the Main Grid. Also, in this test case, conventional droop control guarantees a faster active power regulation due to the lack of the virtual inertia of the VGM control technique but, as one can see from Figure 16, the droop control creates a greater frequency variation in the very first transient.

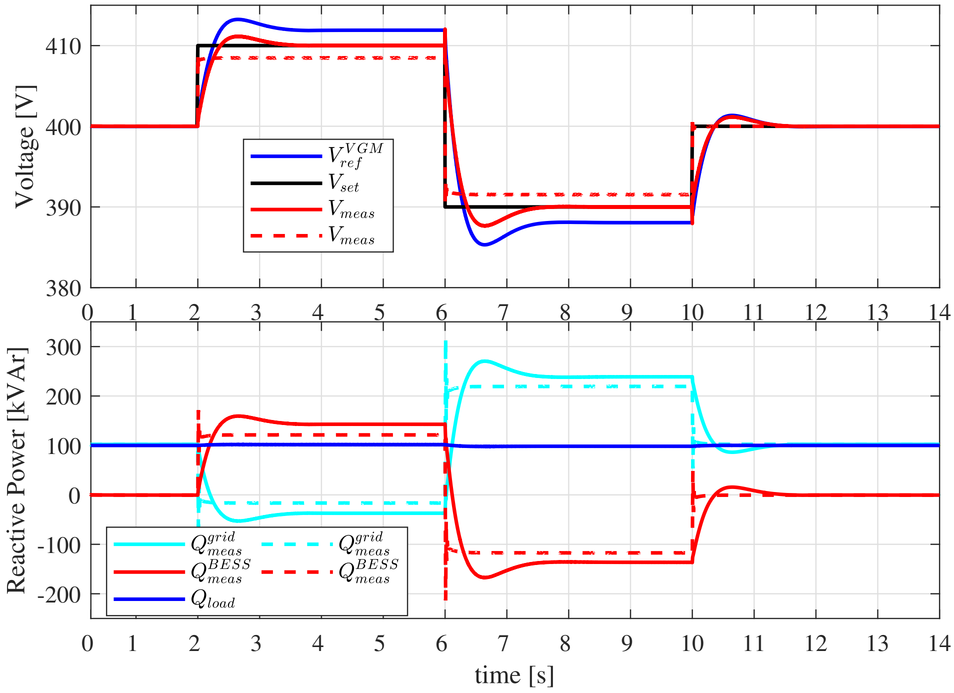

FIGURE 2.13: Voltage (first panel) and reactive powers (second panel) time profiles with voltage setpoint variations with Virtual Generator Mode (VGM) (solid lines) and conventional (dotted lines) techniques.

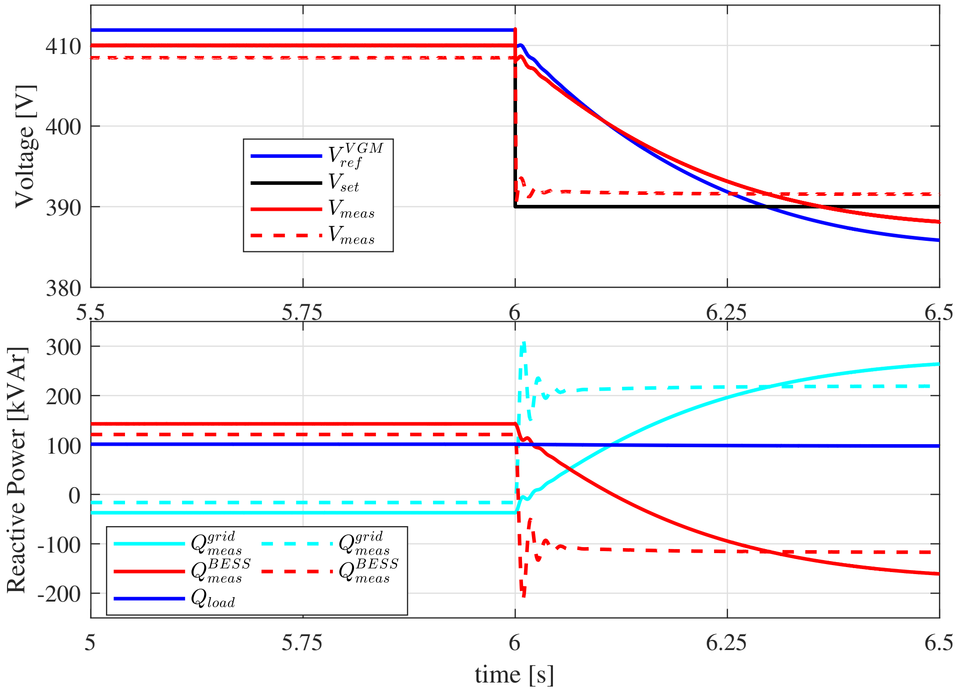

FIGURE 2.14: Detail on the comparison between the proposed technique (solid lines) and conventional droop control (dotted lines).

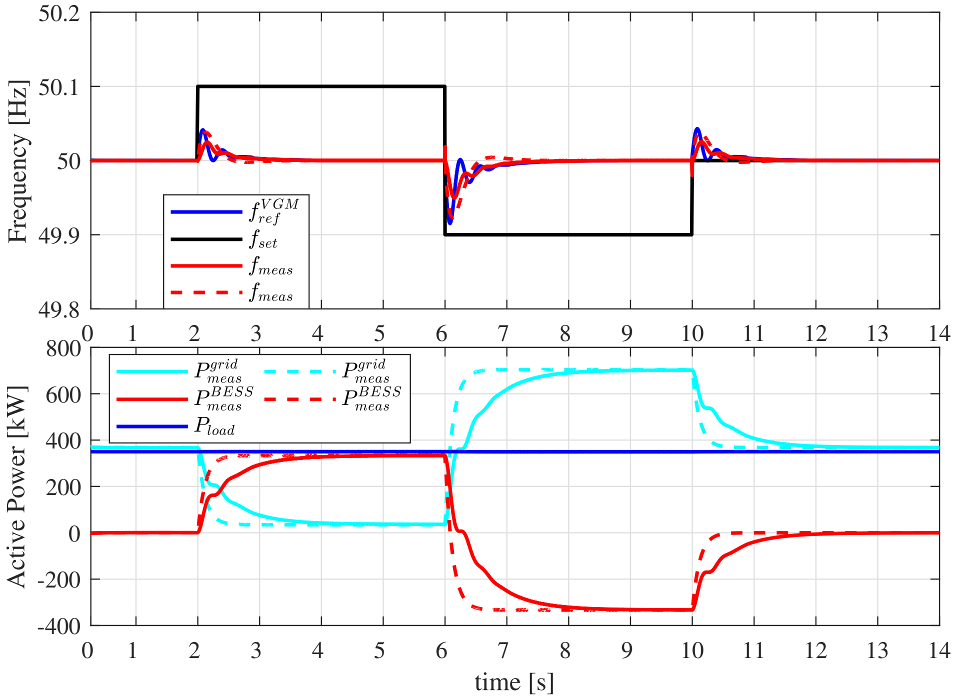

Figure 2.15: Frequency (first panel) and active powers (second panel) time profiles with frequency setpoint variations with VGM (solid lines) and conventional (dotted lines) techniques.

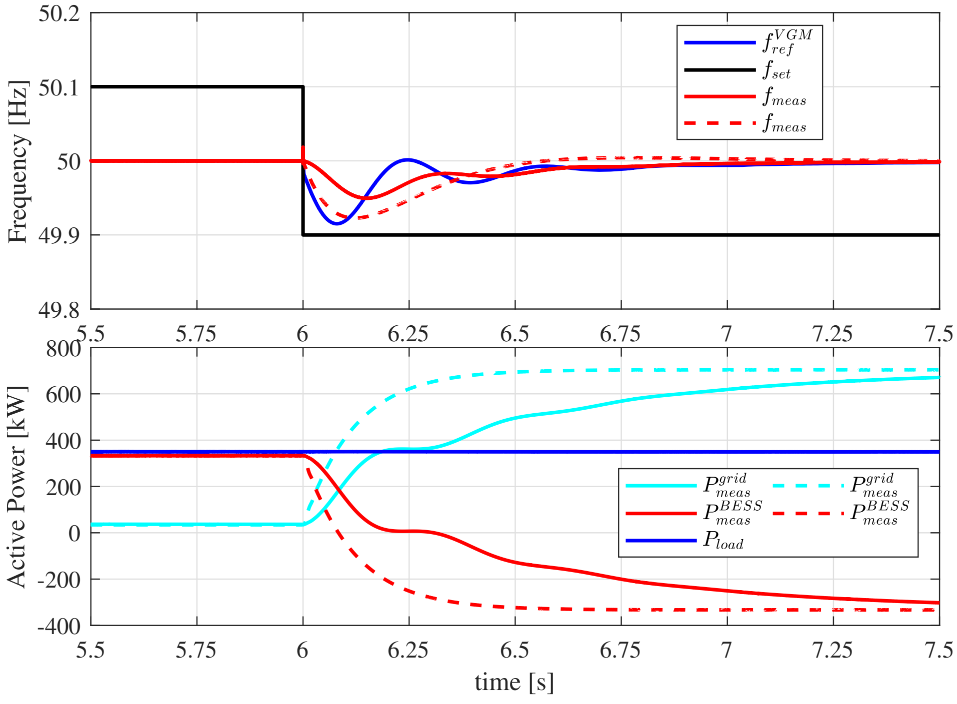

Figure 2.16: Detail on the comparison between the proposed technique (solid lines) and conventional droop control (dotted lines).

### 2.3.3 Paralleling Action and Load Sharing

The aim of this simulation is to show how the BESS converter can be connected to an islanded MG where a diesel generator is already on-line in Grid-Forming operating mode and to also show the correct power sharing functionality. As one can see from figure 2.17, at $t = 0.1s$ a live-start of the BESS converter is activated: the controlled voltage ($v_{An}^{BESS}$, $v_{Bn}^{BESS}$, $v_{Cn}^{BESS}$) starts to follow the connection bus voltages ($v_{An}^{MG}$, $v_{Bn}^{MG}$, $v_{Cn}^{MG}$) and, at $t = 0.2s$, the phase reference output of the primary control $\theta_{ref}^{VGM}$ is synchronized with the measured phase angle $\theta_{meas}$ at the connection bus to the MG. Finally, at $t = 0.25s$, the AC-breaker of the BESS converter is closed and in figure 2.18 is possible to notice a really limited power transient quantifiable in a transient current less than 1 % of the BESS-converter-rated value current. Then in order to test the proper active and reactive power sharing between the diesel generator and the BESS, a load step contingency is implemented at $t = 4s$. Figure 2.19 shows active and reactive powers time profile and it is possible to highlight the correct active and reactive power sharing according to the rated apparent power of the two units. The proper active power

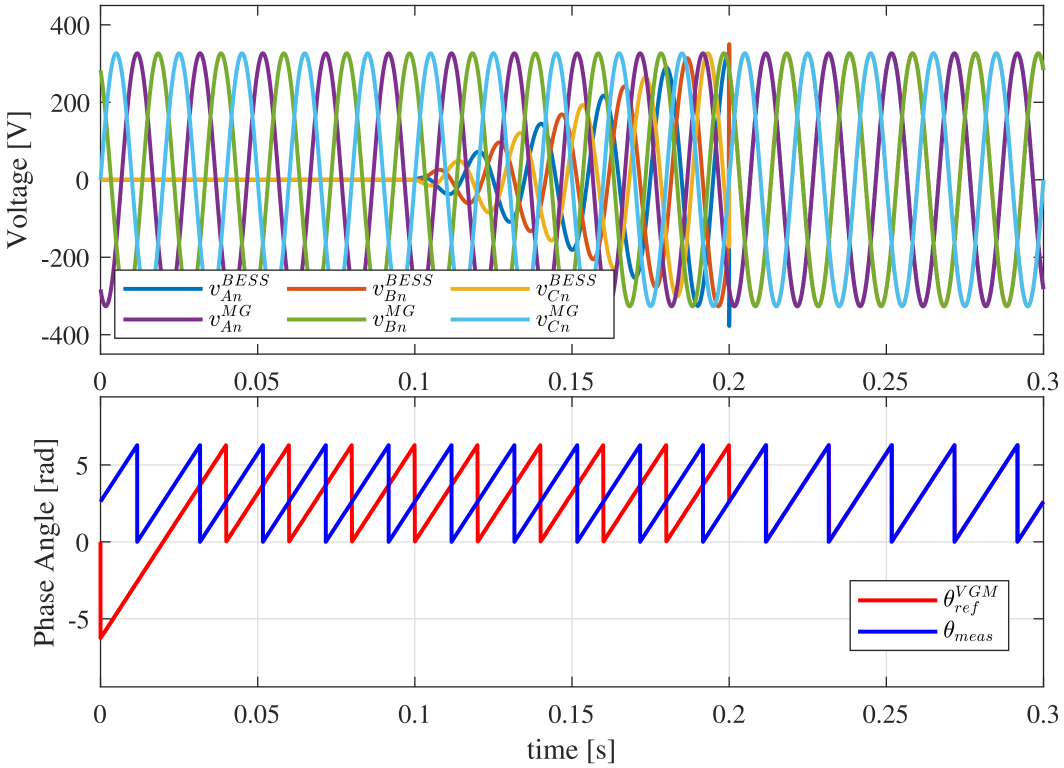

FIGURE 2.17: Voltage (first panel) and phase angles (second panel) during synchronization with MG.

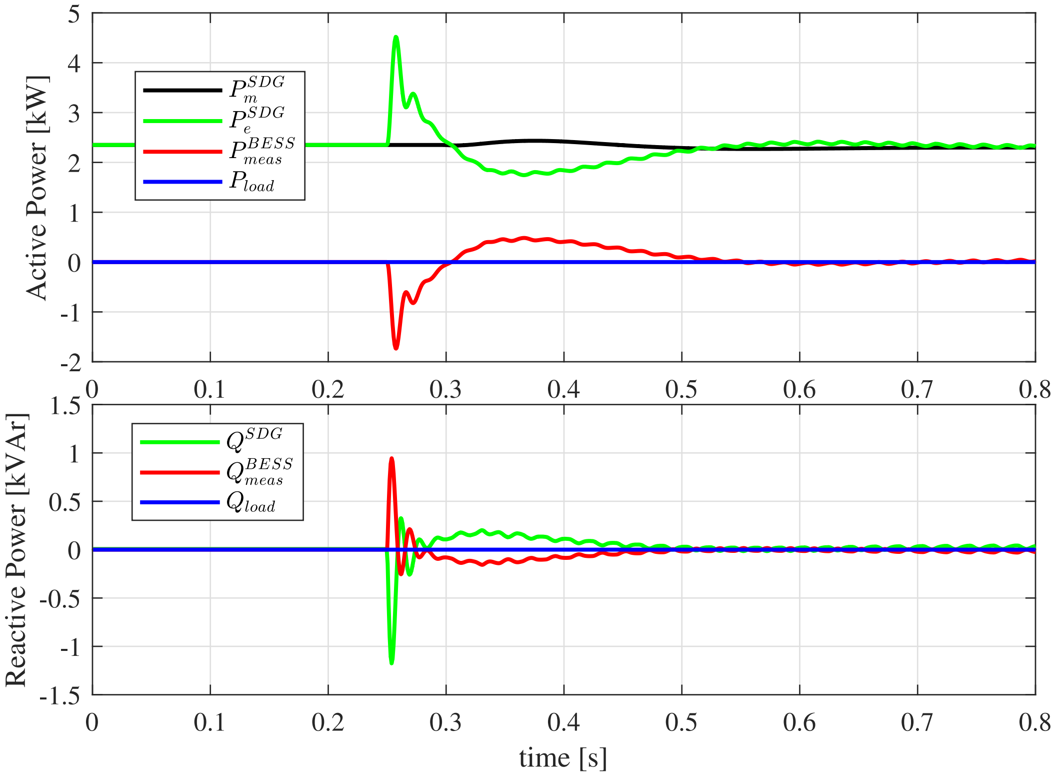

FIGURE 2.18: Active (first panel) and reactive (second panel) powers time profile during paralleling procedure.

sharing can be guaranteed by the relation $A_{BESS}mdroop = A_{SDG}f_{droop}$, while a correct reactive power sharing can be achieved if the droop factors $n_{droop}$ for the BESS and $u_{droop}$ for the diesel generator are correctly set in order to overcome the mismatch in the connection impedances to the MG of the two units. The virtual impedance $R_v + jX_v$ affects the reactive power sharing only during the transient, because in steady state its effect is nullified out by the BESS AVR regulating action on the controlled voltage $V_{meas}$. Instead, figure 2.20 shows frequencies and RMS voltages time profile during the load step contingency and it is possible to highlight the inertial behaviour of the BESS converter and voltage and frequency deviations from the respective rated values according to the droop logic in the proposed primary control.

### 2.3.4 Grid Support Action

In this subsection, the results of the BESS converter controlled in GSM operating mode are presented in detail. The first simulation is carried out in order to test the correct behaviour of the proposed primary control in *GSM-fV*, i.e., when the active/reactive

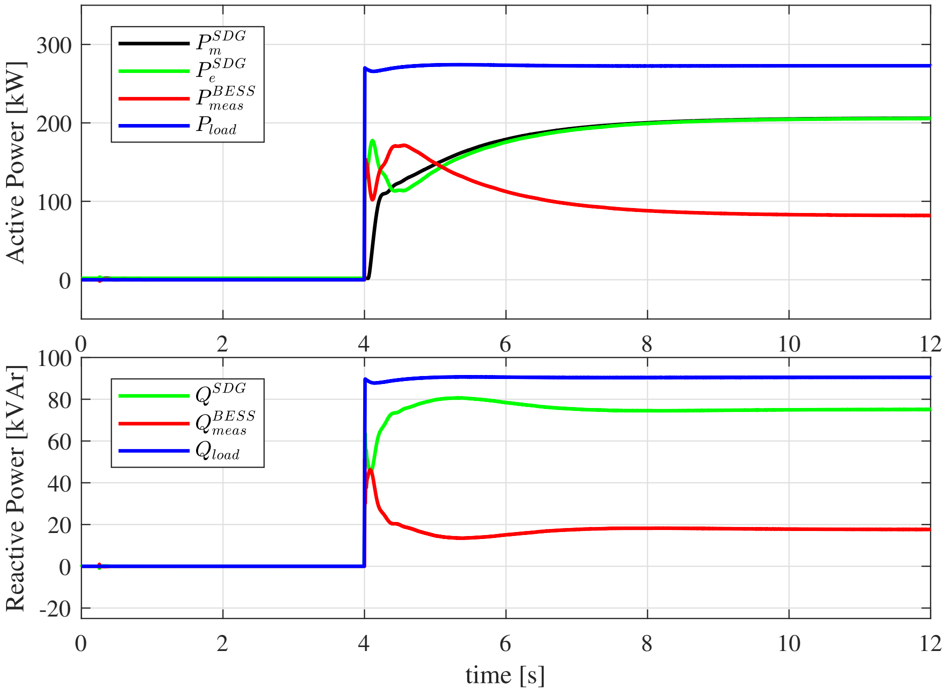

Figure 2.19: Active (first panel) and reactive (second panel) powers time during load step in paralleling configuration.

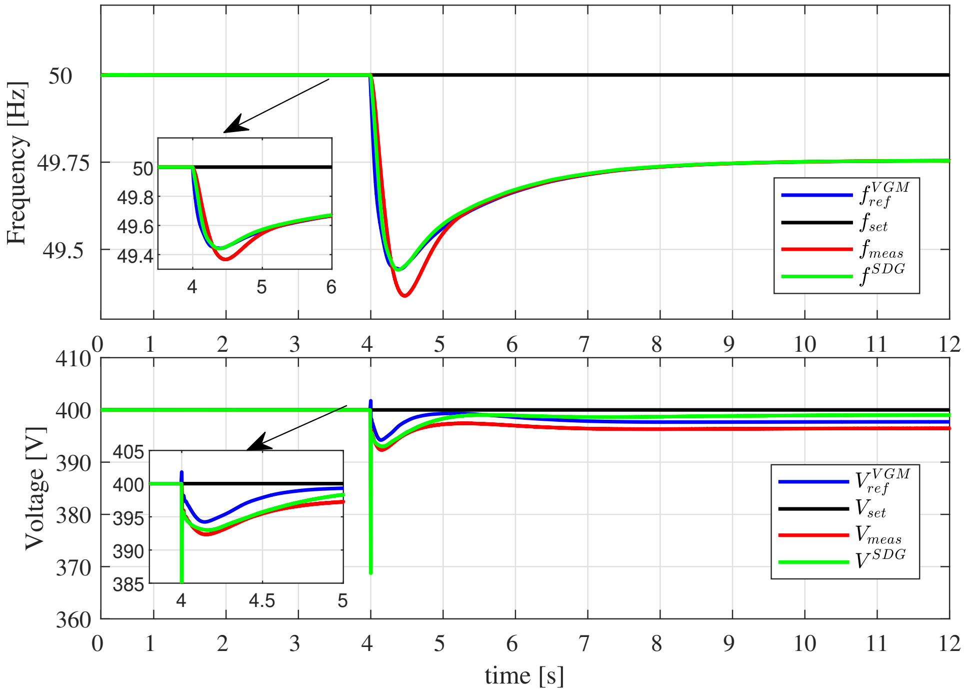

Figure 2.20: Active (first panel) and reactive (second panel) powers time profile during paralleling procedure.

power references come from the envelope curves. In order to highlight the positive effects of the BESS converter in support mode, two different MG configurations are considered:

- In the first configuration, the BESS converter is not connected to the MG. Two different loads, namely $Load_1$ and $Load_2$ are connected to the MG with $P_{load,1} = 300kW$, $Q_{load,1} = 100kVAr$ and $P_{load,2} = 50kW$ (pure resistive load). Loads are supplied by the SDG, while the main grid is disconnected.
- In the second configuration, the BESS is connected to the MG in *GSM-fV* mode ready to provide voltage and frequency support after MG contingencies. At $t = 2s$, $Load_1$ is disconnected to the MG and simulation results are depicted in figures 2.21 and 2.22.

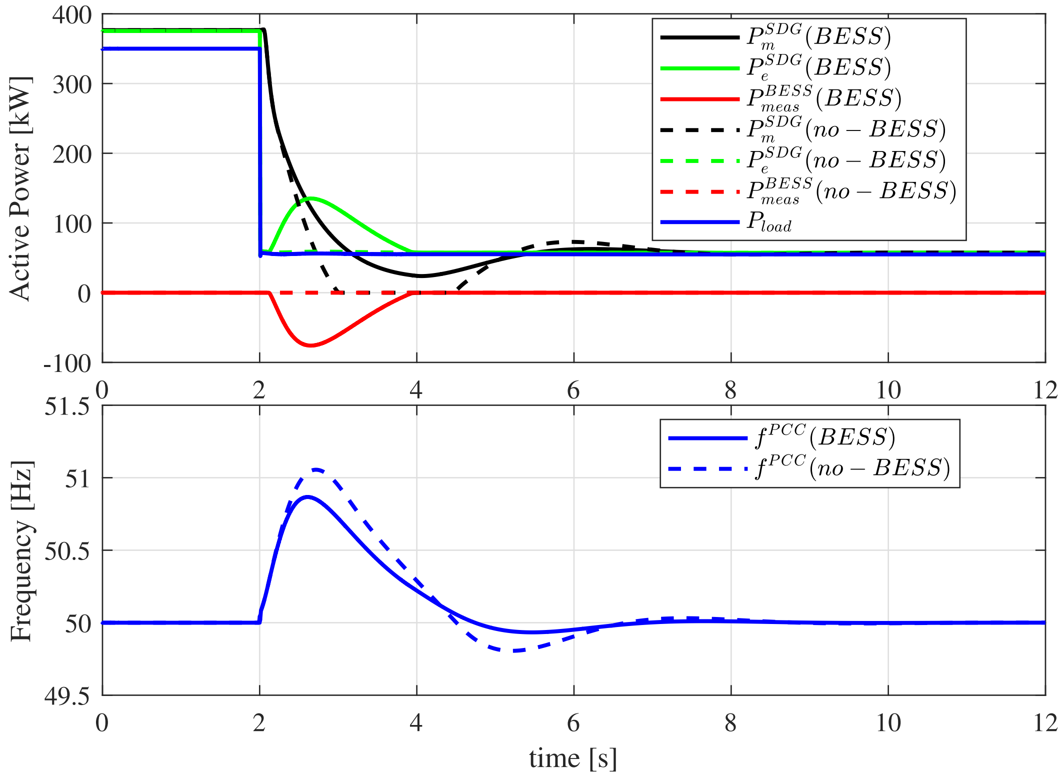

FIGURE 2.21: Active powers and Point of Common Coupling (PCC) frequency in *GSM-fV* mode.

As one can see after the load disconnection, MG frequency $f^{PCC}$ and voltage $V^{PCC}$ (measured at PCC) start to increase: if the BESS is connected in GSM mode, when voltage and frequency exceed the threshold values $\Delta f_1$ and $\Delta V_1$, respectively, the BESS

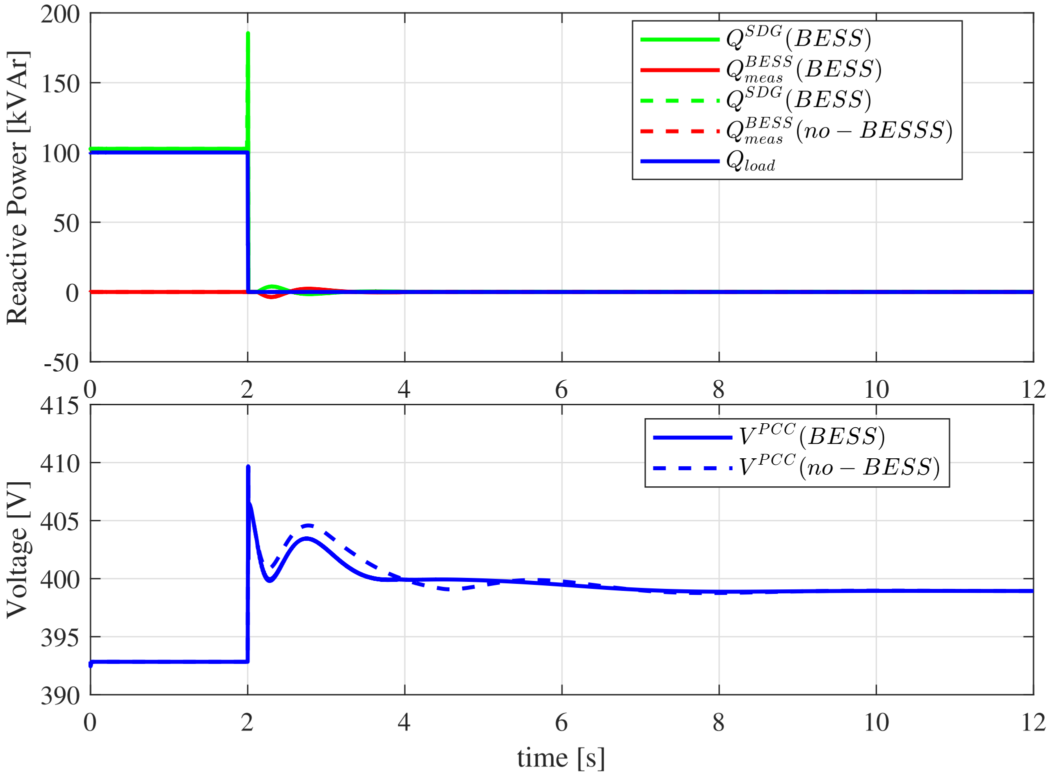

FIGURE 2.22: Reactive powers and PCC voltage in *GSM-fV* mode.

converter starts to absorb active and reactive power according the implemented envelope curves. It is easy to notice that the dynamic response in terms of frequency and voltage with BESS converter controlled in GSM-fV mode (solid lines) is better with respect to the response without BESS connected to the MG (dashed lines). Finally, figure 2.23 shows the correct response of the primary controller in *GSM-PQ* mode, i.e., when the active and reactive power references $P^{GSM-PQ}_{ref}$ and $Q^{GSM-PQ}_{ref}$ are not provided by envelope curve, but are sent by the system controller. In this configuration, the SDG is not connected, while the MG is connected to the main grid: the primary controller is able to correctly track powers references guaranteeing fast regulating actions.

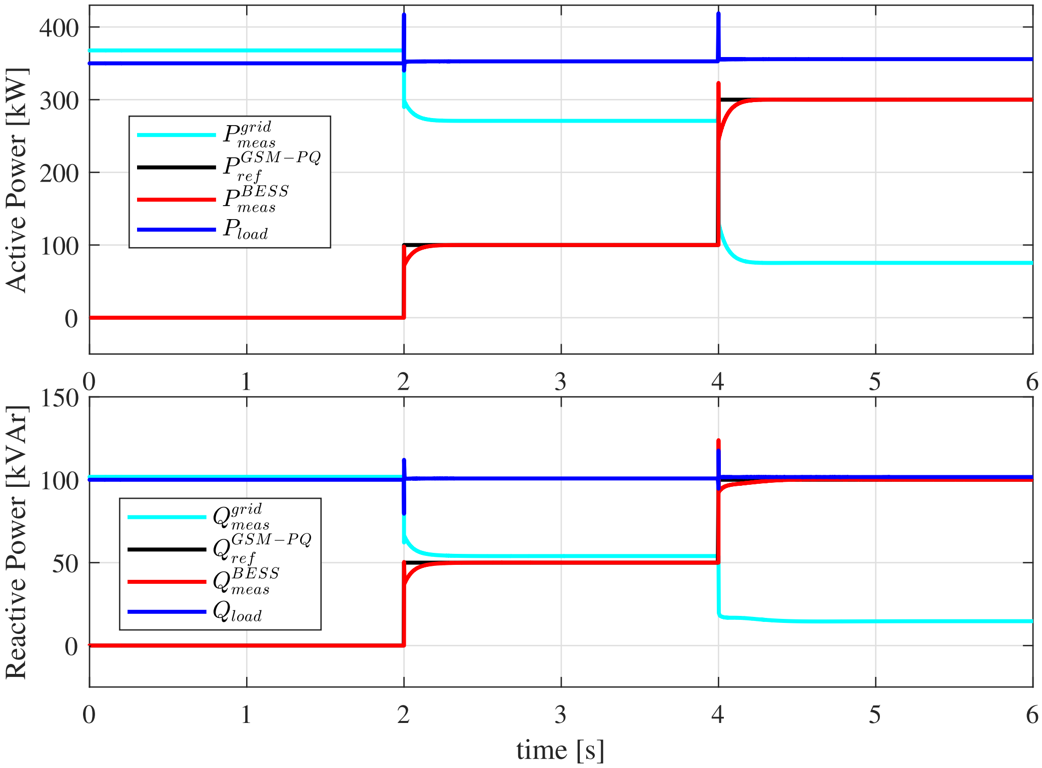

FIGURE 2.23: Active and reactive powers time profile in *GSM-PQ* mode.

## Chapter 3

# BESS converter response during faults: theory and models

**Brief:** This chapter proposes a detailed analysis of the BESS converter response during and after a symmetrical fault. In particular, the first part of this chapter is dedicated to describing inner control loops architectures able to correctly block the converter output current when a fault occurs. The primary level control, based on VGM algorithm, is then analysed in order to carry out a new control strategy to correctly manage the virtual inertia, virtual flux, Governor and AVR contributions also during external disturbances.

**Personal contribution:** I developed the conceptualization, all the part of the Simulink project and the control logic.

The aim of this chapter is to propose a VGM detailed control scheme in which multi loop inner control and the VGM algorithm can work together in order to satisfy all grid codes requirements. The first focus is the converter inner control loops functionality of properly limiting the output current value when a fault occurs. Then a strategy is presented to adapt the VGM control to the action of the multi inner control loops in the phases of fault recognition, fault and fault clearing. The BESS converter primary control and the system model are implemented in the MATLAB/Simulink environment and all the details are reported in the dedicated subsections. The choice to develop the controls and the power system model on MATLAB/Simulink and no longer on DIgSILENT was driven by the need for a powerful and versatile simulation support which offers the possibility to develop more detailed control logics than DIgSILENT PowerFactory. Moreover, a control logic developed in MATLAB/Simulink can be compiled for different targets as .ddl files and can be interfaced with DIgSILENT PowerFactory.

## 3.1 System model configuration

In this section the MG system configuration is presented in figure 3.1. The BESS converter is connected to the MG through an isolation *Dy11* transformer (primary circuit modelled by resistance $R_{1,T}$ and inductance $L_{1,T}$ and secondary circuit modelled by $R_{2,T}$ and inductance $L_{2,T}$) and a line with a resistive part $R_L$ and an inductive part $L_L$. A three phase load can be connected and disconnected to/from the MG with a three phase breaker and it is modelled as a constant impedance load with a rated active power $P_n$ and a rated reactive power $Q_n$. Moreover, an external grid is connected to PCC through a line with a with a resistive part $R_{line}$ and an inductive part $L_{line}$.

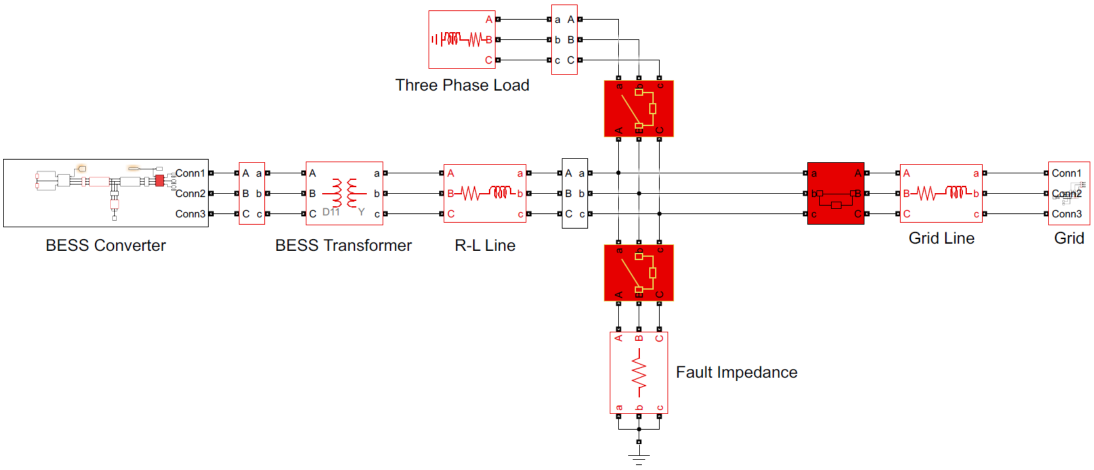

FIGURE 3.1: System model implemented in Simulink environment.

The detailed BESS converter model is depicted in figure 3.2.

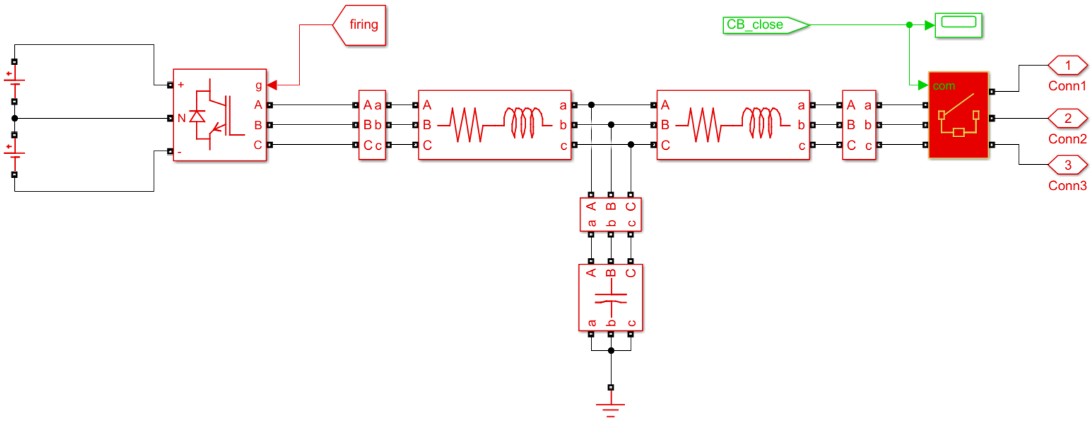

FIGURE 3.2: BESS converter model implemented in Simulink environment.

The BESS converter is a three level IGBT inverter modulated (see figure 3.3) with a carrier frequency $f_s = 5$ kHz and connected to an ideal DC voltage source $V_{dc}$, which is a common practice when the fault analysis is considered [31–33]. The converter is connected to the the grid through a LCL filter where the converter part is modelled by a resistance $R_{fc}$ and inductance $L_{fc}$, the grid part is modelled by a resistance $R_{fg}$ and inductance $L_{fg}$ and the shunt part is a capacitance $C_f$. The MG relevant data are reported in table 3.1.

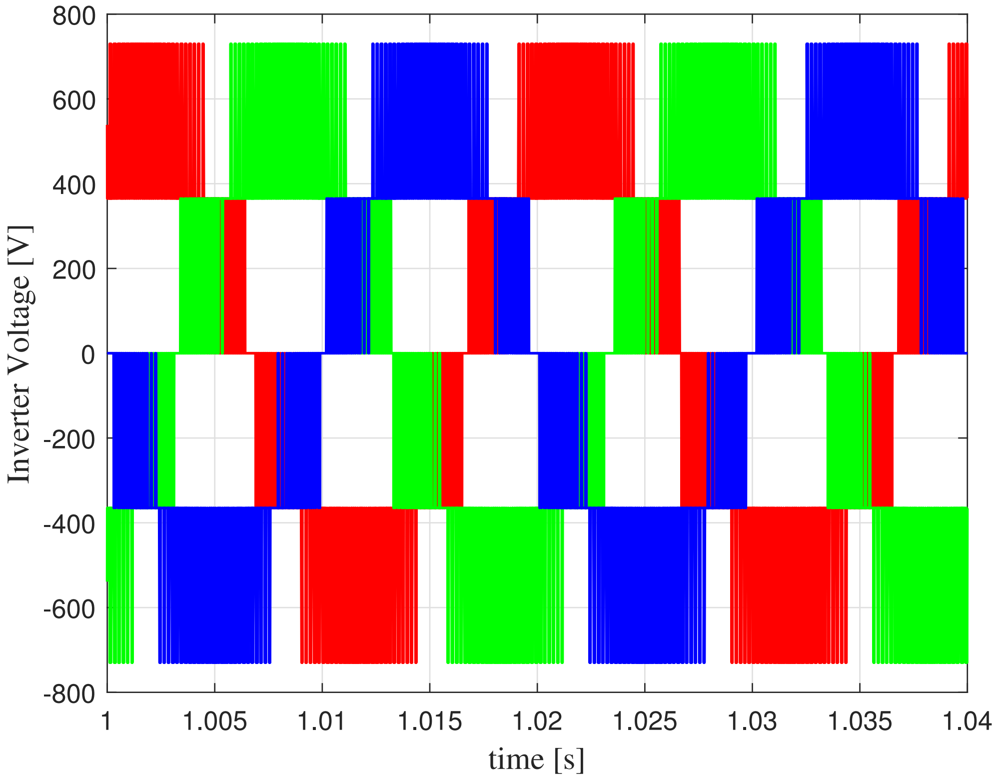

FIGURE 3.3: BESS converter output voltage.

| BESS | Load | Lines and Transformer |
|---|---|---|
| $A_{BESS}$=7.35 kVA | $P_n$=6 kW | $R_L = 0.1$ p.u.;$L_L = 0.04$ p.u. |
| $V_n$=400 V (AC-side) | $Q_n$=2 kVAr | $R_{grid} = 0.1$ p.u.;$L_{grid} = 0.04$ p.u. |
| $f_n$=50 Hz | | $R_{1,T} = 0.002$ p.u.;$L_{1,T} = 0.08$ p.u. |
| $V_{dc}$=730 V | | $R_{2,T} = 0.002$ p.u.;$L_{2,T} = 0.08$ p.u. |
| $f_s = 5$ kHz | | $V_{1n}/V_{2n} = 1$ |
| $R_{fc} = 0.005$ p.u.;$L_{fc} = 0.07$ p.u. | | Connection = *Dy11* |
| $R_{fg} = 0.005$ p.u.;$L_{fg} = 0.04$ p.u. | | |
| $C_f = 0.07$ p.u. | | |

TABLE 3.1: Test case MG parameters.

## 3.2 Inner control loops architectures

### 3.2.1 PID based inner control loops

Voltage control loop for converter connected to the grid with in LCL filter is depicted in figures 3.4 and 3.7. In this configuration, it is based on PID regulators described by proportional and integral gains. Its main control objective is to regulate the output voltage of the inverter by nullifying the error between the reference voltage, which can be created from the VGM outputs $V_{ref}$ and $\theta_{ref,VGM}$, and the measurement $v_{abc,conv}$. The outputs of the voltage controller are the inverter output current references $i_{d,ref,GFM}$ and $i_{q,ref,GFM}$, where *GFM* means Grid Forming Mode, and a signal named "$fault_{signal}$" whose functionality will be explained later on in this chapter.

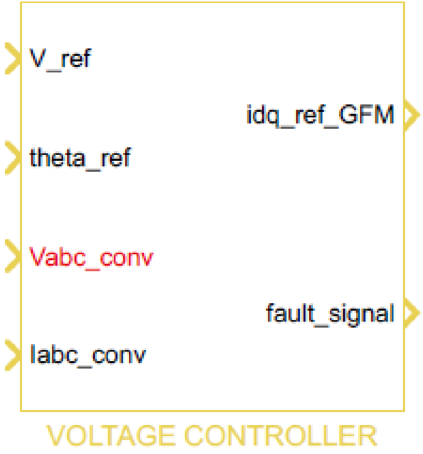

Figure 3.4: BESS converter voltage controller based on PID regulators.

The Park transform adopted, depicted in figure 3.5, is the one which has the rotating frame aligned with $a$-axis as reported below:

$$K(\theta_p) = \frac{2}{3}\begin{bmatrix} \cos(\theta_p) & \cos\left(\theta_p - \frac{2}{3}\pi\right) & \cos\left(\theta_p + \frac{2}{3}\pi\right) \\ -\sin(\theta_p) & -\sin\left(\theta_p - \frac{2}{3}\pi\right) & -\sin\left(\theta_p + \frac{2}{3}\pi\right) \\ \frac{1}{2} & \frac{1}{2} & \frac{1}{2} \end{bmatrix} \tag{3.1}$$

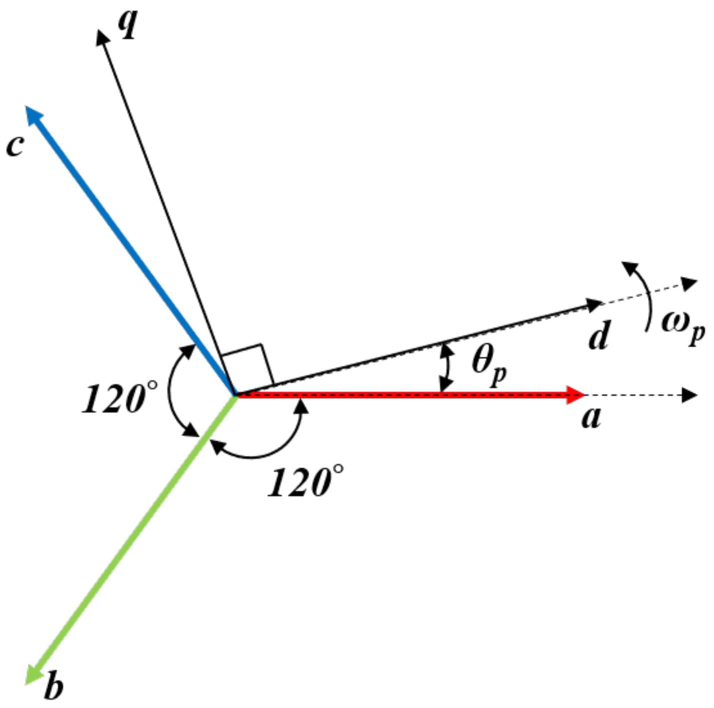

FIGURE 3.5: Park transform orientation.

From the VGM output is possible to construct the $d$-$q$ axis voltage references $v_d^{ref,v}$ and $v_{q,v}^{ref}$ as follows:

$$v_{abc,ref}(t) = \begin{bmatrix} \frac{V_{ref}\sqrt{2}}{\sqrt{3}} \sin\left(\theta_{ref,VGM}\right) \\ \frac{V_{ref}\sqrt{2}}{\sqrt{3}} \sin\left(\theta_{ref,VGM} - \frac{2\pi}{3}\right) \\ \frac{V_{ref}\sqrt{2}}{\sqrt{3}} \sin\left(\theta_{ref,VGM} + \frac{2\pi}{3}\right) \end{bmatrix} \tag{3.2}$$

Let's now consider the Clarke transformation reported below:

$$K_{abc\rightarrow\alpha\beta\gamma} = \frac{2}{3}\begin{bmatrix} 1 & -\frac{1}{2} & -\frac{1}{2} \\ 0 & \frac{\sqrt{3}}{2} & -\frac{\sqrt{3}}{2} \\ \frac{1}{2} & \frac{1}{2} & \frac{1}{2} \end{bmatrix} \tag{3.3}$$

It is possible to use it on relations (3.2) and on the measured currents at the filter output $i_{abc,conv}$, and so the virtual impedance algorithm is implemented as follows:

$$v_\alpha^{ref,v} = v_\alpha^{ref} - \left(R_v i_\alpha^{conv} - X_v i_\beta^{conv}\right) \tag{3.4}$$

$$v_\beta^{ref,v} = v_\beta^{ref} - \left(R_v i_\beta^{conv} + X_v i_\alpha^{conv}\right) \tag{3.5}$$

and consequently:

$$v_d^{ref,v} = v_\alpha^{ref,v}\cos\left(\theta_{ref,VGM}\right) + v_\beta^{ref,v}\sin\left(\theta_{ref,VGM}\right) \tag{3.6}$$

$$v_q^{ref,v} = -v_\alpha^{ref,v}\sin\left(\theta_{ref,VGM}\right) + v_\beta^{ref,v}\cos\left(\theta_{ref,VGM}\right) \tag{3.7}$$

As already done for the LC filter structure presented in the previous chapter, in order to decouple the *d*-*q* axis in the voltage controller it is necessary to insert some feed-forwards actions; considering the voltage-current relation for the filter capacitor $C_f$ below, where $v_{abc,cap}$ is the voltage measured at filter capacitor terminals and $i_{abc,inv}$ is the current measured at the inverter output.

$$C_f\frac{dv_{abc,cap}}{dt} = i_{abc,inv} - i_{abc,conv} \tag{3.8}$$

It is possible to perform the Park transformation as follows:

$$K(\theta_p)C_f\frac{dK^{-1}(\theta_p)v_{dq0}^{cap}}{dt} = K(\theta_p)\left(i_{abc,inv} - i_{abc,conv}\right) \tag{3.9}$$

and after some calculations, it is possible to write:

$$C_f\frac{dv_{dq0}^{cap}}{dt} + \omega_n C_f\begin{bmatrix}0 & -1 & 0\\ 1 & 0 & 0\\ 0 & 0 & 0\end{bmatrix}v_{dq0}^{cap} = i_{dq0}^{inv} - i_{dq0}^{conv} \tag{3.10}$$

and consequently:

$$C_f\frac{dv_d^{cap}}{dt} = i_d^{inv} - i_d^{conv} + \omega_n C_f v_q^{cap} \tag{3.11}$$

$$C_f\frac{dv_q^{cap}}{dt} = i_q^{inv} - i_q^{conv} - \omega_n C_f v_d^{conv} \tag{3.12}$$

Considering equations (3.11) and (3.12) it is possible to write the two feed-forward actions $i_{ff,d}$ and $i_{ff,q}$ for the two regulating channels:

$$i_{ff,d} = i_d^{conv} - \omega_n C_f v_q^{cap} \tag{3.13}$$

$$i_{ff,q} = i_q^{conv} + \omega_n C_f v_d^{cap} \tag{3.14}$$

Finally, the PID control action can be easily described by the following equations:

$$i_{d,ref,GFM} = K_{PV}\left(v_d^{ref} - v_d^{conv}\right) + K_{IV}\int\left(v_d^{ref,v} - v_d^{conv}\right)dt + i_{ff,d} \tag{3.15}$$

$$i_{q,ref,GFM} = K_{PV}\left(v_q^{ref} - v_q^{conv}\right) + K_{IV}\int\left(v_q^{ref,v} - v_q^{conv}\right)dt + i_{ff,q} \tag{3.16}$$

Therefore, there is the necessity to implement a current limiting strategy in order to avoid over-currents during a fault events which may cause converter circuit breaker tripping and/or semiconductors damage. In this work the current limiting strategy is based on a scaling factor named Current Limiting Factor (CLF) that is used to modify the voltage controller output $i_{d,ref,GFM}$ and $i_{q,ref,GFM}$ when a fault occurs, i.e.:

$$i'_{d,ref,GFM} = CLF \quad i_{d,ref,GFM} \tag{3.17}$$

$$i'_{q,ref,GFM} = CLF \quad i_{q,ref,GFM} \tag{3.18}$$

This factor can be easily calculated with the following procedure: If the RMS value of the current references $\sqrt{i^2_{d,ref,GFM} + i^2_{q,ref,GFM}}$ exceeds the threshold value $I_{fault,th}$, the scaling factor can be calculated as $CLF = \frac{I_{fault,th}}{\sqrt{i^2_{d,ref,GFM} + i^2_{q,ref,GFM}}}$, otherwise $CLF = 1$. As one can see from figure 3.7, the scaled current reference values $i'_{d,ref,GFM}$ and $i'_{q,ref,GFM}$ are saturated: the reason for this is that a temporary limiting strategy is required to protect the inverter against large currents from over-currents start to the proposed method activation instant. After activation of the proposed limiting strategy, as the current reference is limited, the instantaneous saturation limit does not affect this reference, but an anti wind-up method is implemented in the PID regulators in order to discharge the PID internal integrator when the controller hits the saturation limits and enters non-linear operation.

BESS converter current regulator is depicted in figures 3.6 and 3.8. The current controller is based on PI regulators described by proportional gain $K_{PC}$ and integral gain $K_{IC}$ and it acts on the system in order to control the converter output current by minimizing the errors between the references coming from the voltage controller and the measured current described by $i_{abc,inv}$. The outputs of the current controller are the inverter voltage modulation signals in the d-q reference frame $v_{d,inv,ref}$ and $v_{q,inv,ref}$.

Also in this case there is the need to decouple the two regulating channels, so the first

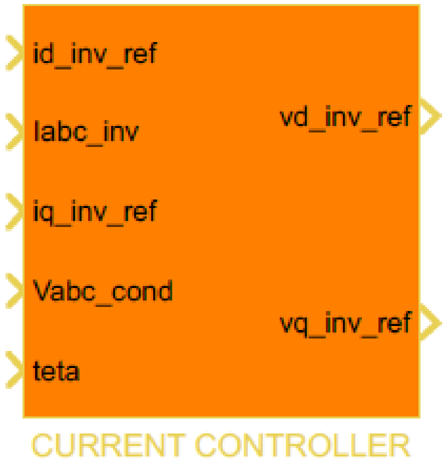

FIGURE 3.6: BESS converter current controller based on PID regulators.

step is to write the Kirchhoff law for the LCL filter:

$$L_{fc}\frac{di_{abc,inv}}{dt} = v_{abc,inv} - R_{fc}i_{abc,inv} - v_{abc,cap} \tag{3.19}$$

performing the Park transform as follows:

$$K(\theta_p)L_{fc}\frac{dK^{-1}(\theta_p)i_{dq0}^{inv}}{dt} = K(\theta_p)\left(v_{abc,inv} - R_{fc}i_{abc,inv} - v_{abc,cap}\right) \tag{3.20}$$

and after some calculations as done for the voltage controller is possible to write:

$$L_{fc}\frac{di_d^{inv}}{dt} = v_d^{inv} - R_{fc}i_d^{inv} - v_d^{cap} + \omega_n L_{fc}i_q^{inv} \tag{3.21}$$

$$L_{fc}\frac{di_q^{inv}}{dt} = v_q^{inv} - R_{fc}i_q^{inv} - v_q^{cap} - \omega_n L_{fc}i_d^{inv} \tag{3.22}$$

Considering equations (3.21) and (3.22) it is possible to write the two feed-forward actions $v_{ff,d}$ and $v_{ff,q}$ for the two regulating channels:

$$v_{ff,d} = v_d^{cap} - \omega_n L_{fc}i_q^{inv} \tag{3.23}$$

$$v_{ff,q} = v_q^{cap} + \omega_n L_{fc}i_d^{inv} \tag{3.24}$$

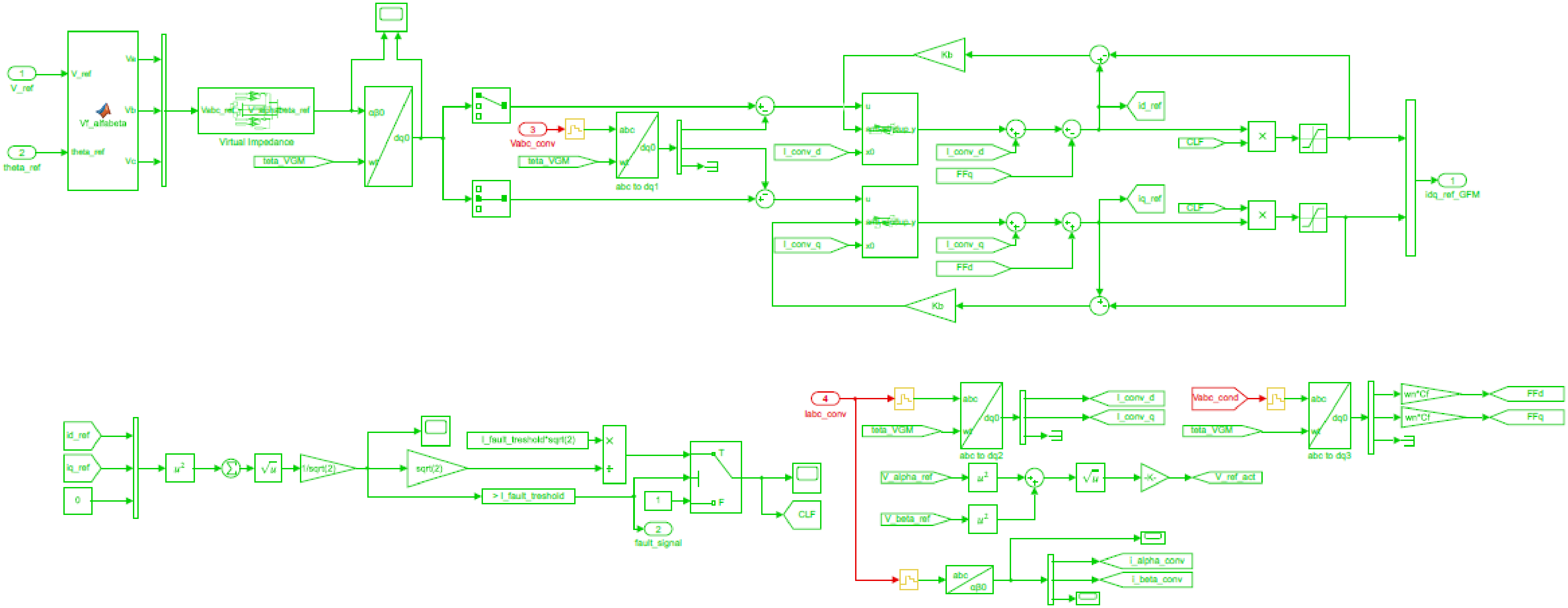

FIGURE 3.7: Detailed BESS converter voltage controller based on PID regulators.

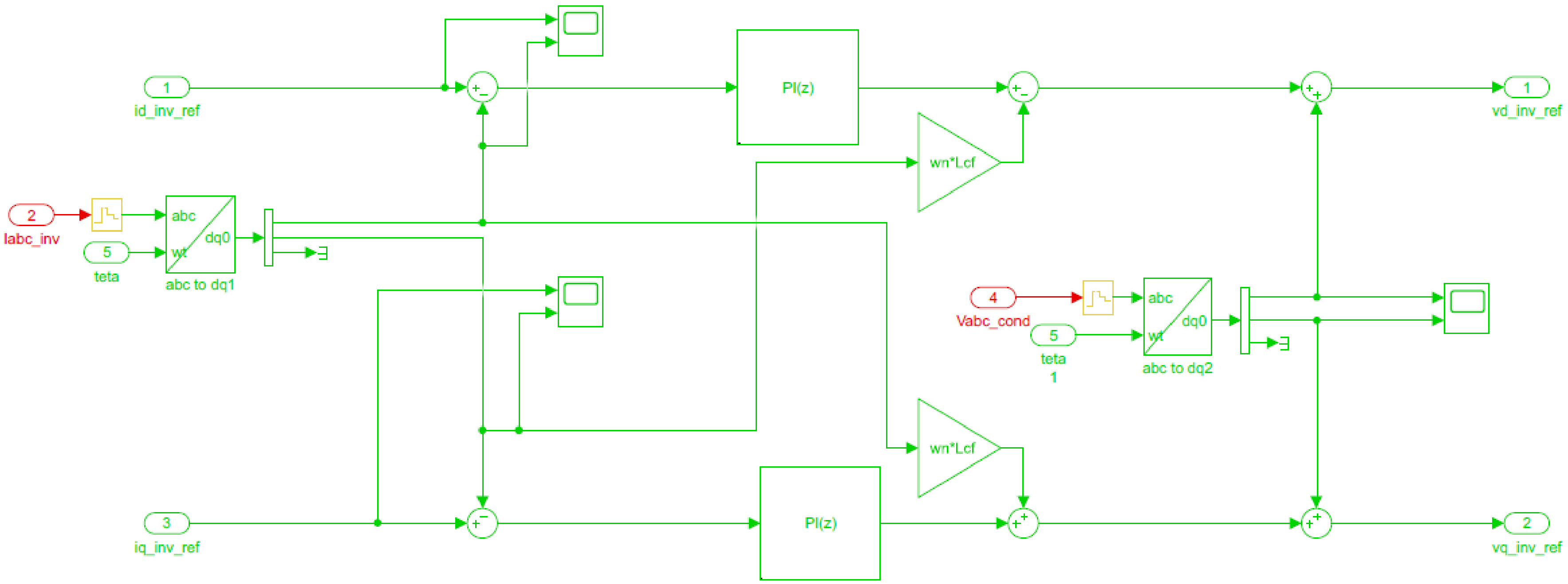

FIGURE 3.8: Detailed BESS converter current controller based on PID regulators.

### 3.2.2 Resonant controller based inner control loops

In this section a different inner control loops architecture is presented. In general, three phase stationary frame regulators are regarded as being unsatisfactory for AC voltage and current regulations since a conventional PID regulator in this reference frame suffers from significant steady-state amplitude and phase errors. In contrast, synchronous frame – regulators can achieve zero steady-state error by acting on DC signals in the rotating reference frame, and are therefore usually considered to be superior to stationary frame regulators. However, a synchronous frame regulator is more complex, as it requires a means of transforming a measured stationary frame AC quantities (or error) to rotating frame DC ones, and transforming the resultant control action back to the stationary frame for execution. These transformations can introduce errors if the synchronous frame identification is not accurate. The transfer function of a resonant controller can be expressed as follows:

$$G(s) = K_p + \frac{2K_i\omega_c s}{s^2 + 2\omega_c s + \omega_o^2} \tag{3.25}$$

where $K_p$ is the proportional gain, $K_i$ is the integral gain, $\omega_c$ is the resonant bandwidth and $\omega_o$ is the resonant frequency. Constructing the current regulator in the stationary reference frame $\alpha - \beta$ has the advantage of requiring much less signal processing than the synchronous frame demodulation approaches, and it is also less sensitive to noise. Bode diagram is depicted in figure 3.9, while the response when varying the term $\omega_c$ is depicted in figure 3.10. The implementation of the resonant controllers in Simscape environment is depicted in figures 3.11 and 3.12. The voltage controller provide the reference currents for the current regulator in the $\alpha - \beta$ reference frame and the current controller provides the reference voltages for the converter modulation. The logic for the fault current limitation is the same as the implemented in the PID approach.

In figure 3.13 it is possible to see a comparison between the two proposed architectures when a fault event occurs. Both PID and Proportional-Resonant (P-R) controllers are able to limit the converter current (this simulation is performed in islanded configuration), and it is possible to see that the P-R controllers are able to guarantee a reduced peak current compared to the PID ones. In figure 3.14 it is possible to see the dynamic of the CLF, i.e. it is equal to 1 when there are no fault conditions, while it has its dynamic when the limitation logic is activated by the reference currents from the voltage controller.

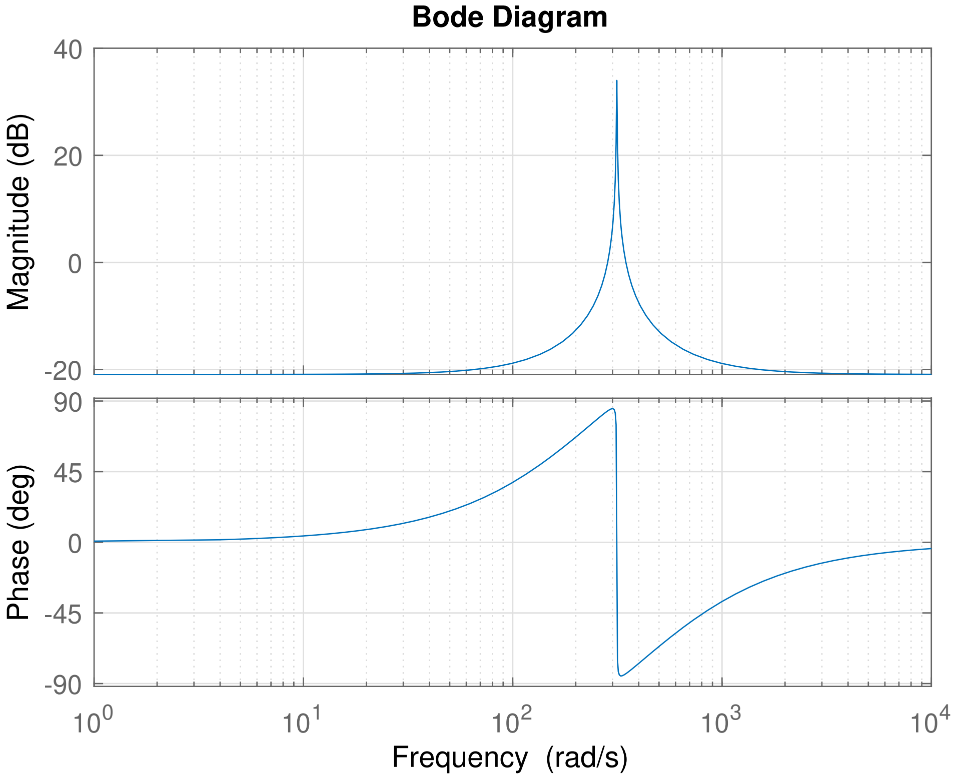

FIGURE 3.9: Bode plot of a resonant controller

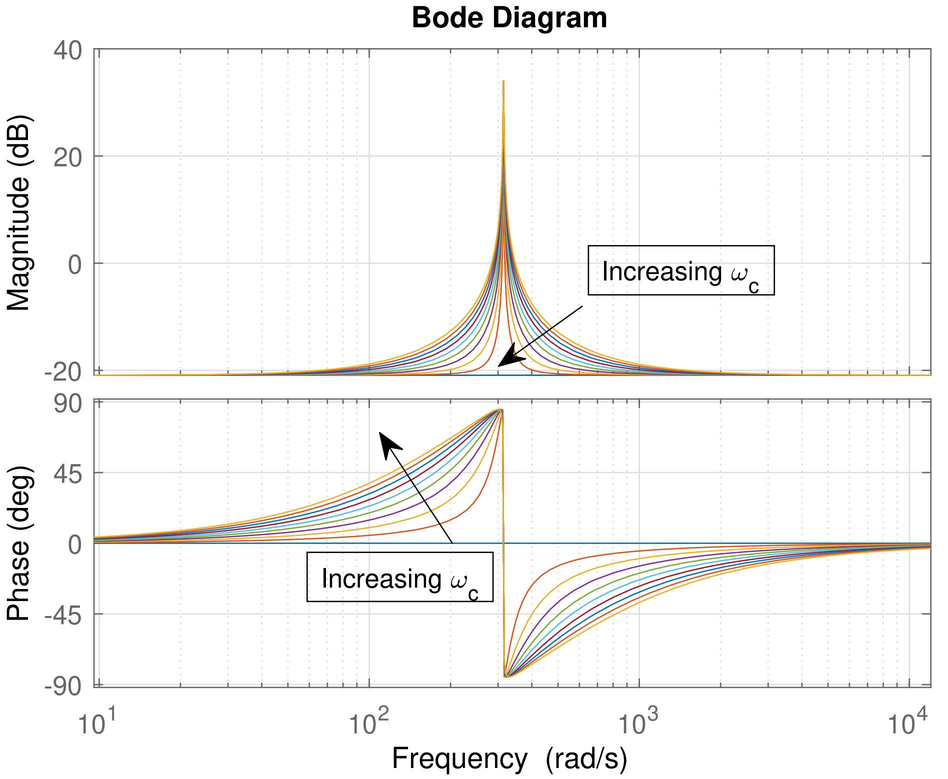

FIGURE 3.10: Bode response of the resonant term for variation in $\omega_c$

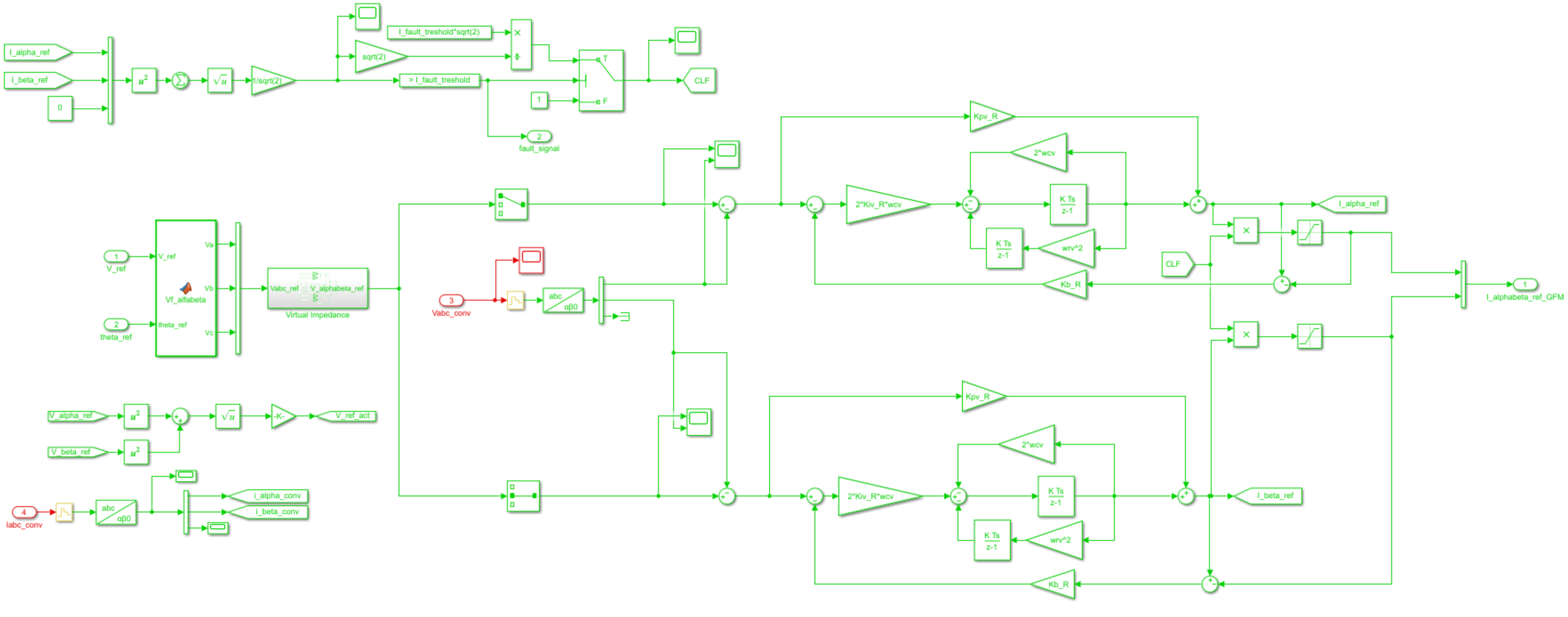

FIGURE 3.11: Detailed BESS converter voltage controller based on resonant regulators.

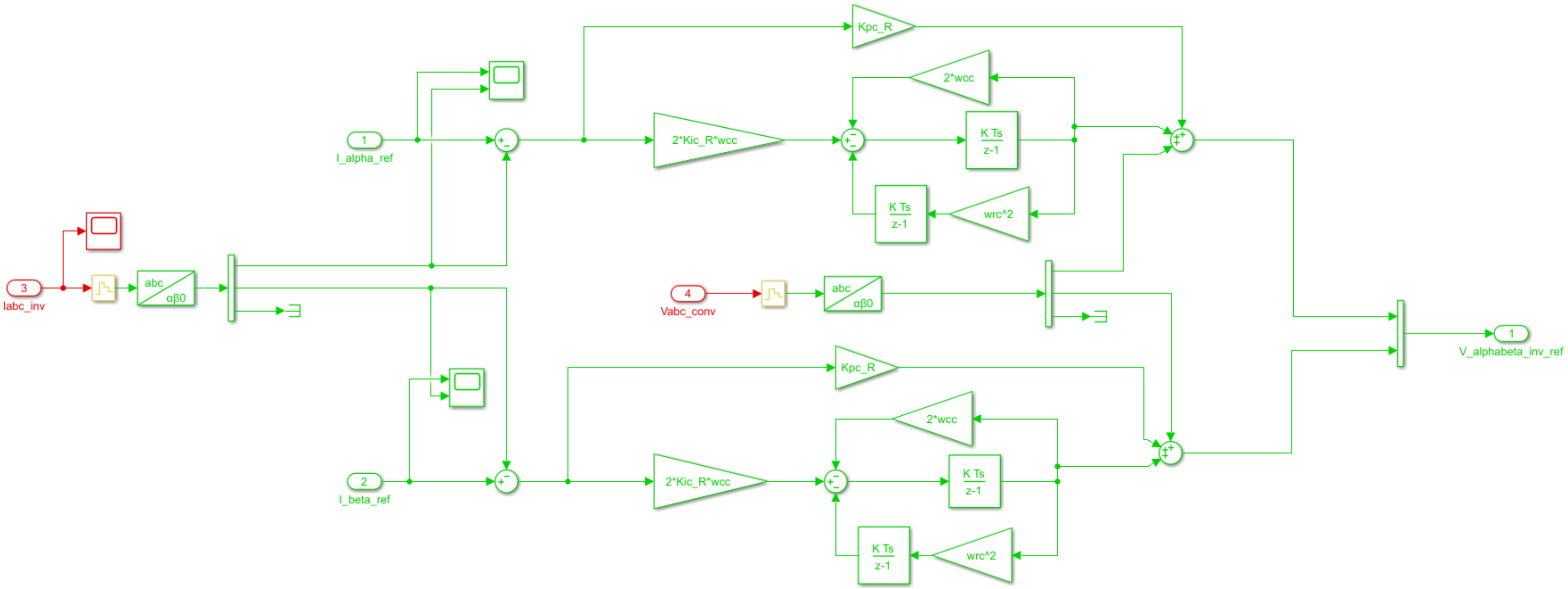

FIGURE 3.12: Detailed BESS converter current controller based on resonant regulators.

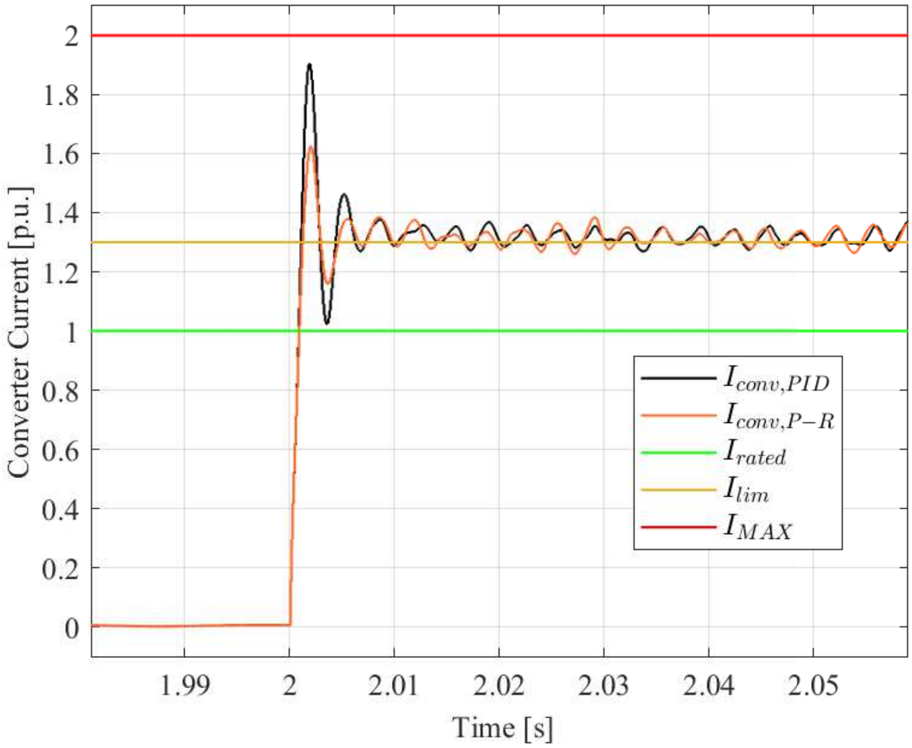

FIGURE 3.13: Converter current during fault.

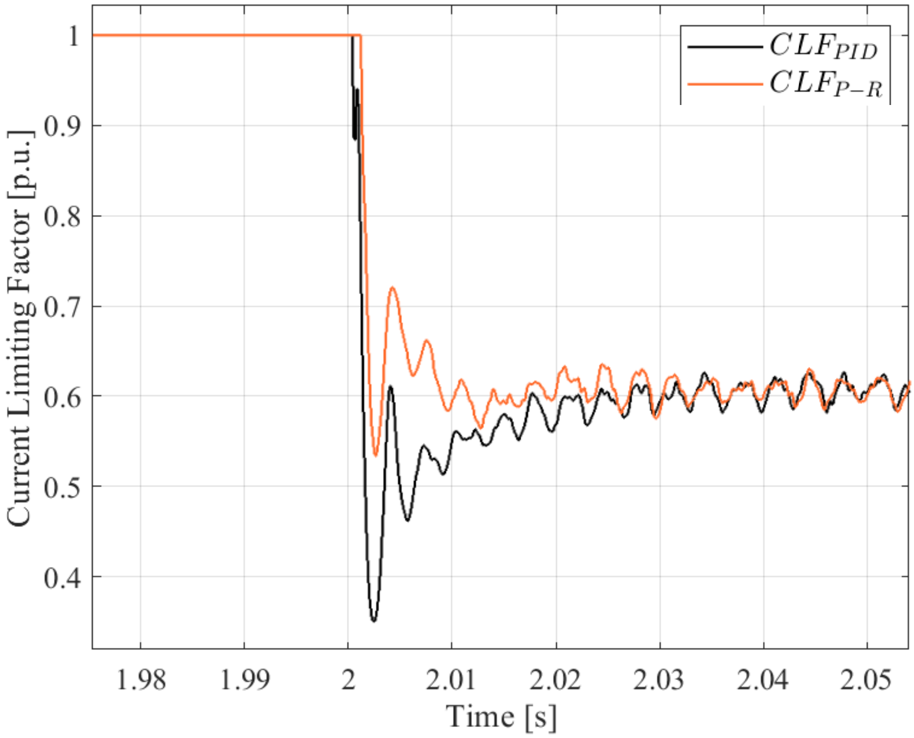

FIGURE 3.14: Current Limiting Factor during fault.

## 3.3 Virtual Generator algorithm for fault conditions

In the last chapter the VGM algorithm was presented considering normal operation scenarios. In the present section this control technique is modified in order to proper manage the fault contingencies in different operating mode and in order to correct manage the current limiting action implemented in the voltage inner control loop. The complete model implemented in Simscape environment is depicted in figure 3.15. The input of the proposed primary controller are the voltage set point $V_{ref}$, the frequency set point $f_{ref}$, active and reactive powers measurement, respectively $P_{meas}$ and $Q_{meas}$, frequency and voltage measurements $f_{meas}$ and $V_{meas}$, the voltage angle $\theta$ for the synchronization phase and finally a logic signal named $fault_{signal}$ which comes from the voltage controller. The outputs are the voltage reference $V_{ref,VGM}$ and the angle reference $\theta_{ref,VGM}$.

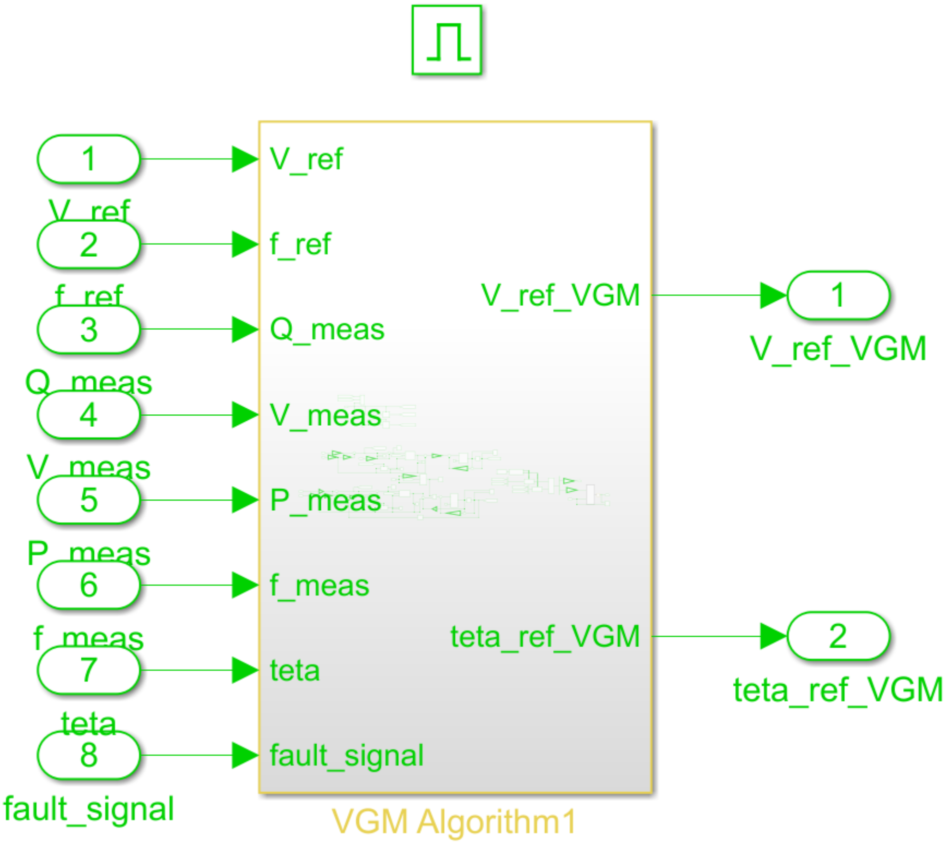

FIGURE 3.15: Virtual Generator algorithm in Simscape environment.

As explained in the last chapter the VGM algorithm proposed in this work consists of four macro parts: (*i*) the Governor model, (*ii*) the AVR model, (*iii*) the Inertia model and (*iv*) the Rotor Flux model. The equations which describe the four macro parts are:

- $$P_{GOV}^{BESS} = K_{P,GOV}\left(f_{ref} - f_{meas}\right) + K_{I,GOV}\int_0^t \left(f_{ref} - f_{meas}\right) d\tau \tag{3.26}$$

- $$Q_{AVR}^{BESS} = K_{P,AVR}\left(V_{ref} - V_{meas}\right) + K_{I,AVR}\int_0^t \left(V_{ref} - V_{meas}\right) d\tau \tag{3.27}$$

- $$\theta_{ref,VGM} = \int_0^t \int_0^t K_H \left(P_{GOV}^{BESS} - P_{meas} - K_d f_{ref,VGM}\right) d^2\tau \tag{3.28}$$

- $$V_{ref,VGM} = \int_0^t K_\Psi \left(Q_{AVR}^{BESS} - Q_{meas}\right) d\tau \tag{3.29}$$

When a fault occurs it produces a voltage sag in $V_{meas}$ and a modification in the measured frequency $f_{meas}$ and, as can be seen from equations (3.26) and (3.27), this produces a variation on the Governor and AVR outputs $P_{GOV}^{BESS}$ and $Q_{AVR}^{BESS}$ respectively. From equations (3.28) and (3.29) it is possible to see that the Governor and AVR regulating action during fault causes a variation in VGM algorithm output $\theta_{ref,VGM}$ and $V_{ref,VGM}$ and this variation is modulated by the inertia constant $K_H$ and the rotor flux constant $K_\Psi$.

Now, in order to have an example that acts as a guiding thread in the theoretical treatment of this chapter, from this point forward, let us consider a resistive fault event at $t = 4s$ located at the PCC bus in islanded configuration. It is possible to see the VGM regulating actions in figure 3.16. As one can see the voltage sag imposed by the symmetrical fault causes a reduction of active power and the Governor try to reduce the reference $P_{GOV}^{BESS}$ in order to restore the rated frequency. Moreover, the voltage sag causes a fast variation in the AVR output $Q_{AVR}^{BESS}$ which is limited to $1.2p.u.$ and the error between $Q_{AVR}^{BESS}$ and the measured reactive power $Q_{meas}$ produces a fast increase of the VGM reference voltage $V_{ref,VGM}$ which reaches is maximum value of $1.1p.u.$. These dynamics cause a poor restoring phase when the fault is cleared, and, as it will be shown in the next chapter, in the islanded configuration the VGM can cause a slow and oscillatory response, while in the grid-connected one can cause voltage and frequency instability.

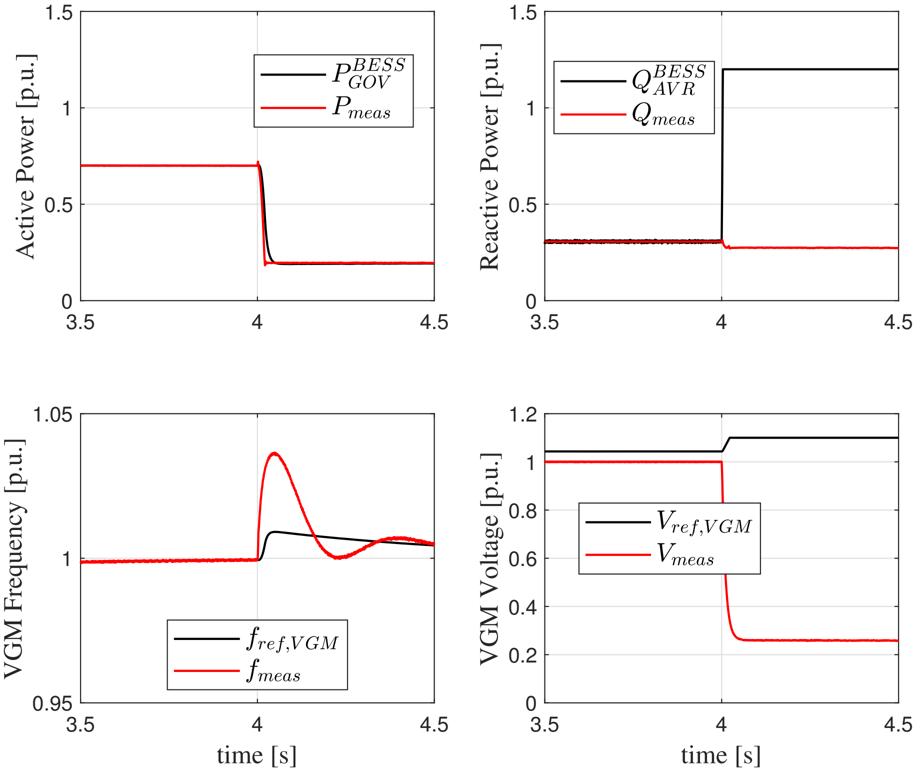

FIGURE 3.16: VGM regulating actions during a fault event.

These considerations on VGM algorithm dynamic behaviour lead to the fact of having to implement a corrective logic that allows the control to properly manage the regulating variables in order to ensure compliance with the requirements imposed by grid codes. The basic idea is to exploit the possibilities given by the intrinsic nature of a virtual generator, i.e. all the four macro parts are configurable and can be adapted when a specific contingency is detected. For this reason, a modification on the inertia constant $K_H$ and to rotor flux constant $K_\Psi$ is implemented when a fault is detected as this strategy, proposed in the present work, is called *adaptive VGM*. If these two parameters are modified by reducing their rated value $(RV)$ of a factor named *Fault constant (*$F_c < 1$*)* when the fault event is detected by the voltage controller as follows:

$$K_H, K_\Psi = \begin{cases} RV & if \quad t < t_{fault} \\ RV * F_c & if \quad t_{fault} < t < t_{clearing} \\ RV & if \quad t > t_{clearing} \end{cases} \tag{3.30}$$

it is possible to guarantee stiff dynamics in the VGM output as depicted in figure 3.17.

Moreover, another modification of the proposed VGM algorithm can be implemented in order improve the performance during a fault event. This improvement consists in the possibility given by the virtual synchronous generator of freezing the regulating actions of Governor and AVR when a fault is detected, i.e. the outputs of Governor and AVR $P_{GOV}^{BESS}$ and $Q_{AVR}^{BESS}$ respectively are fixed to the values previous fault. Defining $e_{GOV}$ the error between the reference frequency $f_{ref}$ and the measured one $f_{meas}$ and $e_{AVR}$ the error between the reference voltage $V_{ref}$ and the measured one $V_{meas}$, the freezing actions can be described as:

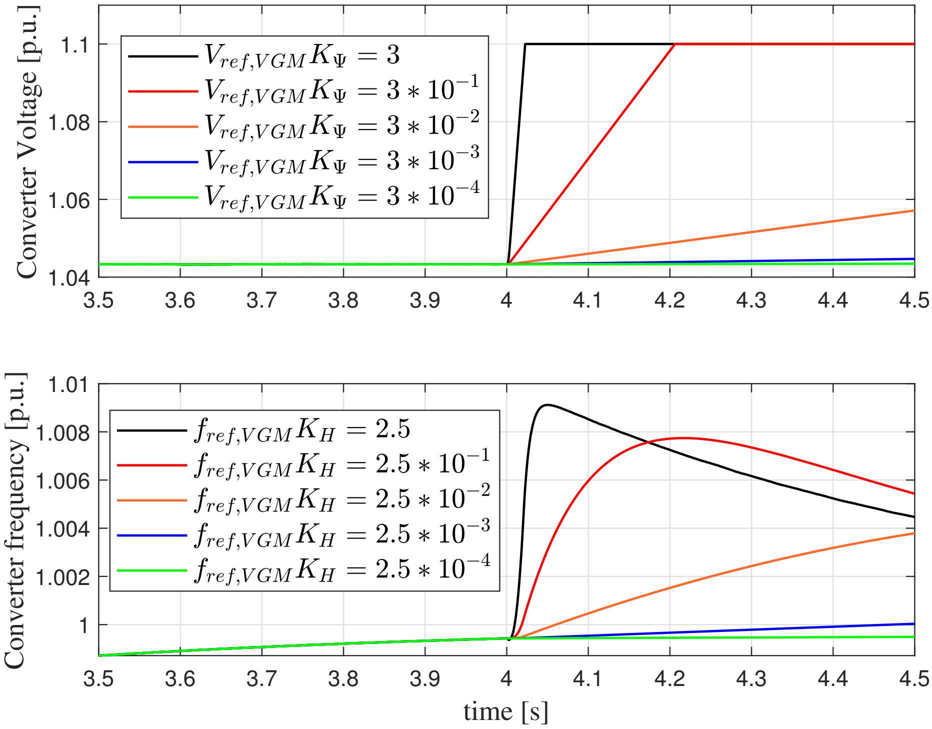

FIGURE 3.17: Comparison between VGM outputs with different parameter modifications.

$$e_{GOV} = \begin{cases} f_{ref} - f_{meas} & if \quad t < t_{fault} \\ 0 & if \quad t_{fault} < t < t_{clearing} \\ f_{ref} - f_{meas} & if \quad t > t_{clearing} \end{cases} \tag{3.31}$$

$$e_{AVR} = \begin{cases} V_{ref} - V_{meas} & if \quad t < t_{fault} \\ 0 & if \quad t_{fault} < t < t_{clearing} \\ V_{ref} - V_{meas} & if \quad t > t_{clearing} \end{cases} \tag{3.32}$$

Therefore the implementation of *adaptive VGM* and the freezing actions on Governor and AVR improve the transient response of the BESS converter when a fault occurs as depicted in figure 3.18.

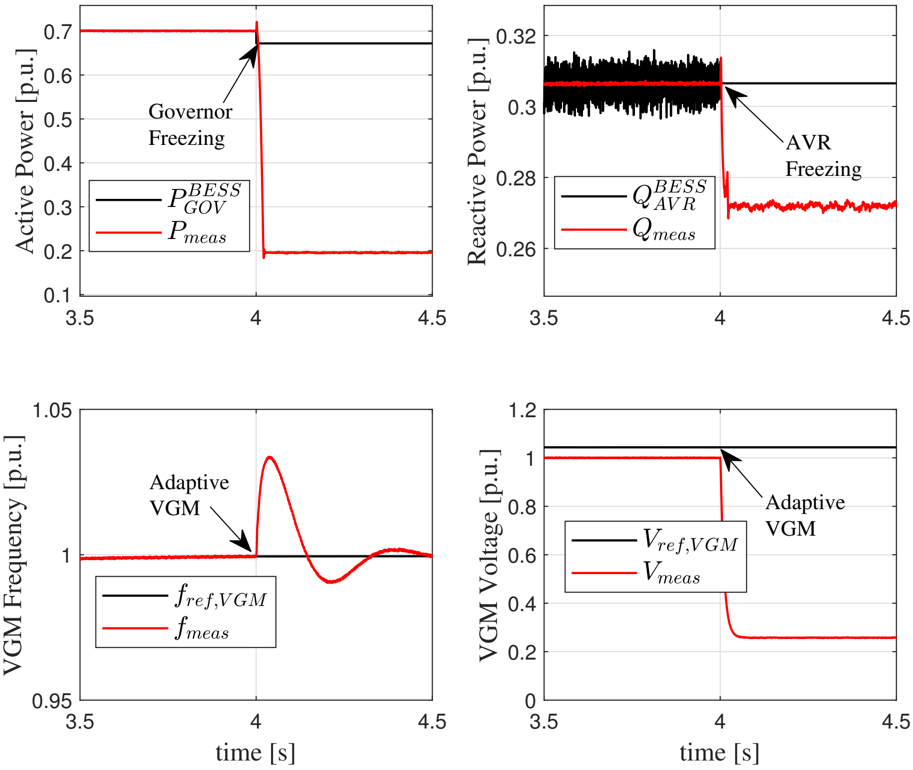

FIGURE 3.18: Effects of *adaptive VGM* and Governor and AVR freezing.

Now, another important aspect regarding the modification of the proposed VGM algorithm is the fault signal sent from the voltage controller. Of course the faster the fault event is detected the more efficient are the strategies of *adaptive VGM* and Governor and AVR freezing, but the same thing is not true for the clearing phase. In fact it can be demonstrated that if a short intentional delay on the fault signal is added for the clearing phase, a relevant improvement in terms of recovery time and system variable overshoots can be achieved. The intentional delay is expressed as a multiple $k$ of the control time step $T_s$, so relations (3.30), (3.31) and (3.32) are modified as follows:

$$K_H, K_\Psi = \begin{cases} RV & if \quad t < t_{fault} \\ RV * F_c & if \quad t_{fault} < t < t_{clearing} + kT_s \\ RV & if \quad t > t_{clearing} + kT_s \end{cases} \tag{3.33}$$

$$e_{GOV} = \begin{cases} f_{ref} - f_{meas} & if \quad t < t_{fault} \\ 0 & if \quad t_{fault} < t < t_{clearing} + kT_s \\ f_{ref} - f_{meas} & if \quad t > t_{clearing} + kT_s \end{cases} \tag{3.34}$$

$$e_{AVR} = \begin{cases} V_{ref} - V_{meas} & if \quad t < t_{fault} \\ 0 & if \quad t_{fault} < t < t_{clearing} + kT_s \\ V_{ref} - V_{meas} & if \quad t > t_{clearing} + kT_s \end{cases} \tag{3.35}$$

The positive effects of the intentional delay on the clearing phase can be appreciated in figures 3.19 and 3.20 where the VGM variables and the BESS converter RMS current is depicted for different values of the control time step multiple $k$. More precisely it is possible to see the dynamic behaviour with no intentional delay and with three different values of $k$, and the greater the value is the better performances can be guaranteed. Of course there is a compromise between the length of $k$, which can not be too long, and the ability of restoring the variables previous the fault event and, as shown in the figures below, a correct choice is $k = 1000$, which corresponds to a delay of $100ms$ (i.e. 5 cycles at the fundamental frequency).

For sake of completeness, the performances of the VGM algorithm with the implementation of relations (3.33), (3.34) and (3.35) in grid connected configuration considering a fault event at the PCC bus, can be appreciated in figures 3.21 and 3.22, but a exhaustive set of simulations will be presented in the following chapter.

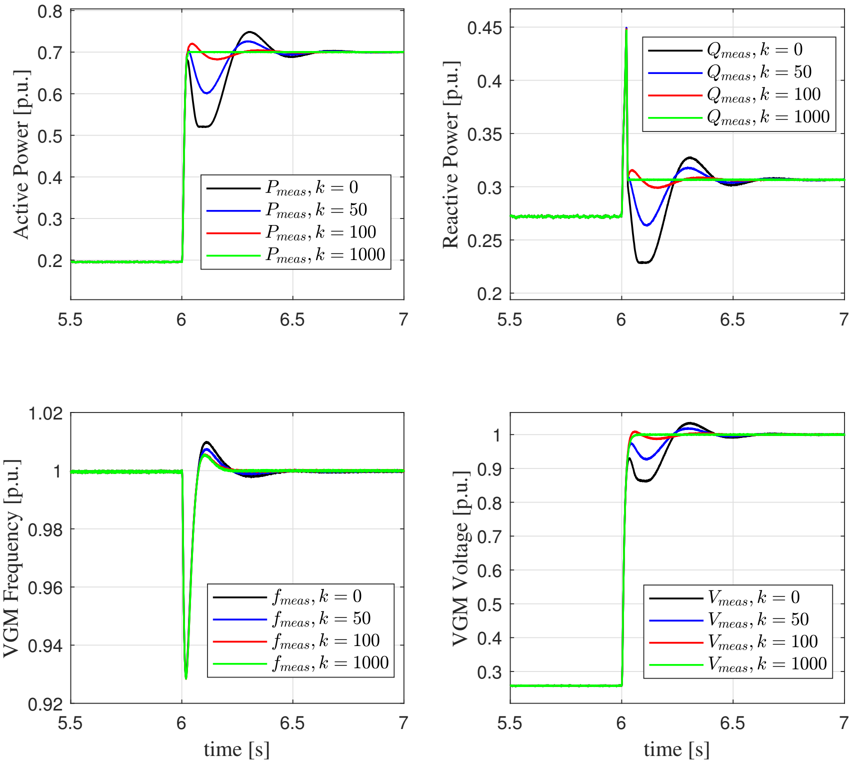

FIGURE 3.19: Effect of delay length $k$ on the VGM variables.

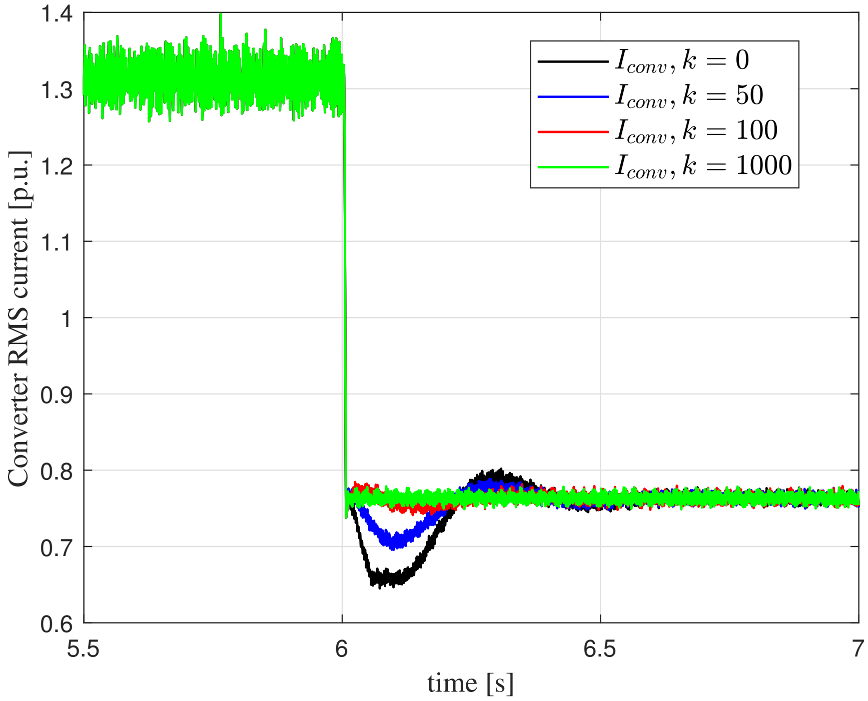

FIGURE 3.20: Effect of delay length $k$ on BESS RMS current.

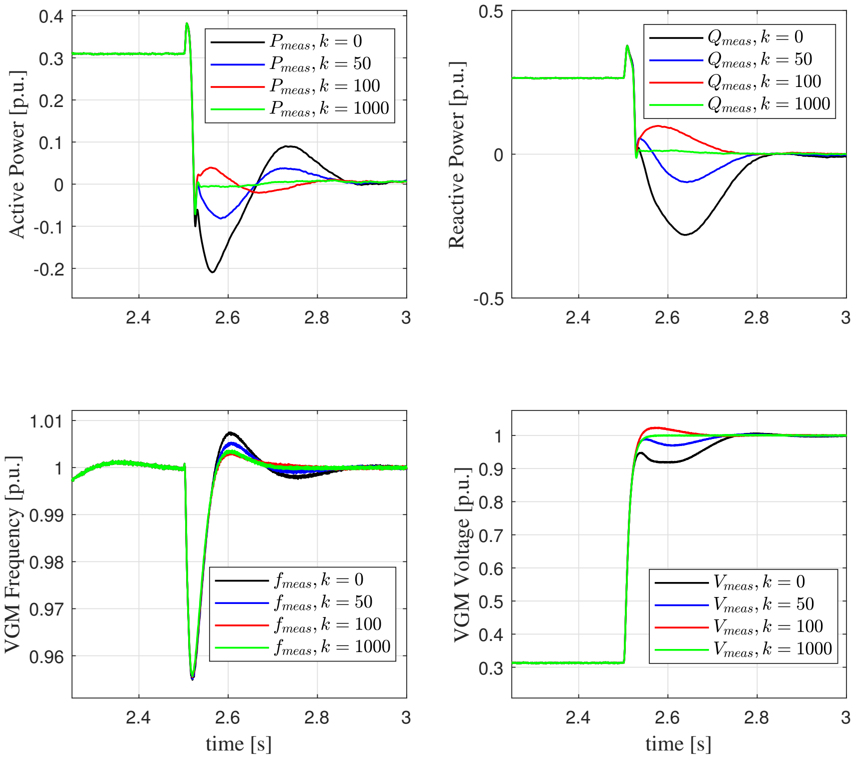

FIGURE 3.21: Effect of delay length $k$ on the VGM variables in grid connected configuration.

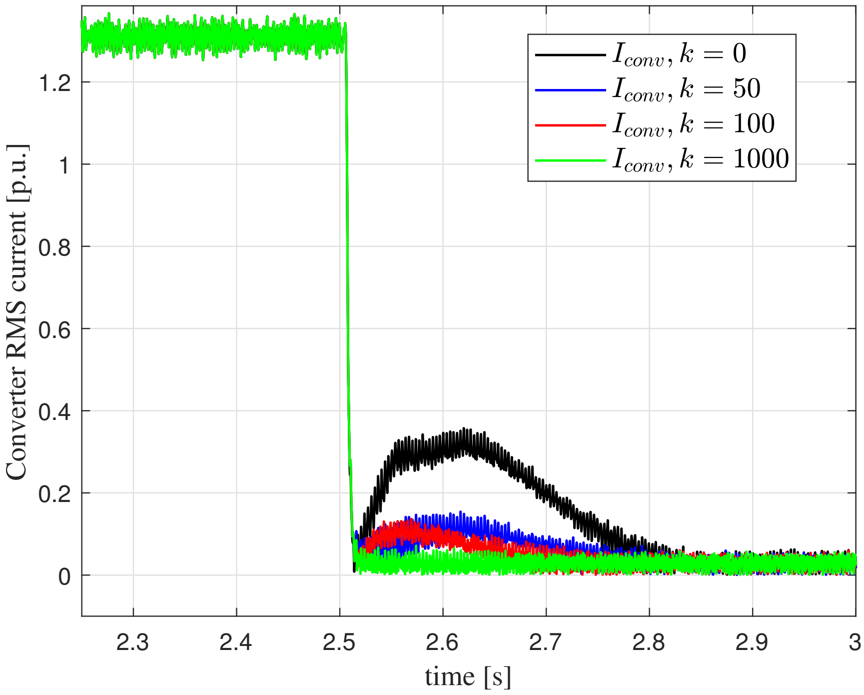

FIGURE 3.22: Effect of delay length $k$ on BESS RMS current in grid connected configuration.

For sake of clarity the conceptual final control scheme of the proposed modified VGM algorithm implemented in MATLAB/Simscape environment is reported in figure 3.23.

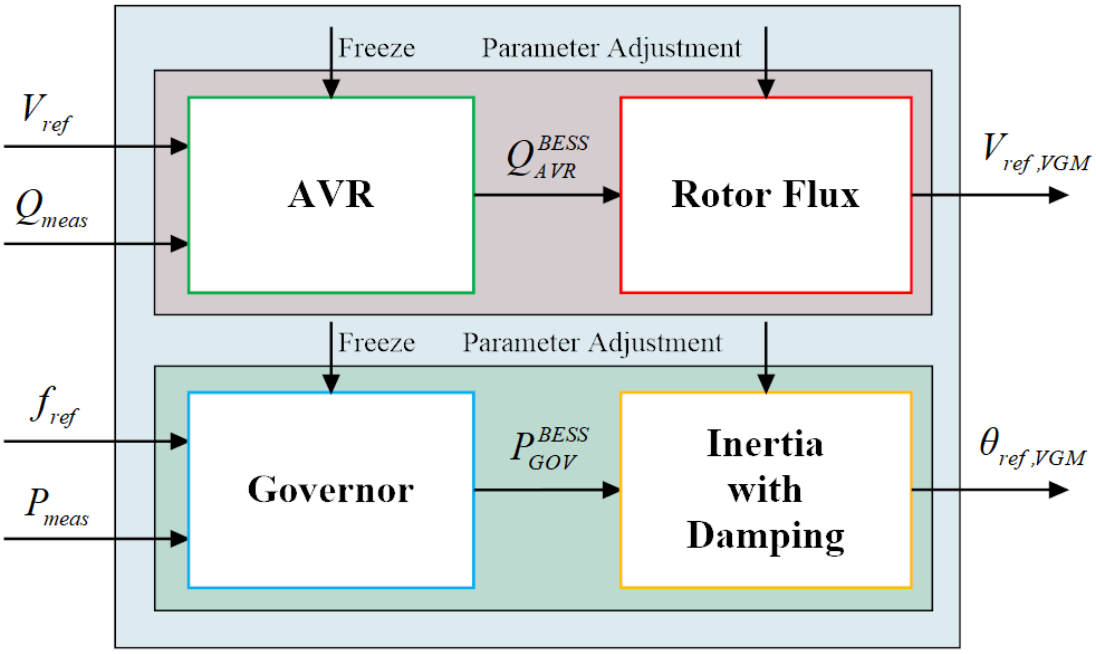

Figure 3.23: Conceptual scheme of Virtual Generator algorithm in Simscape environment.

# Chapter 4

# BESS converter response during faults: simulation results

**Brief:** This Chapter proposes a complete set of simulations in order to test in different relevant operating scenarios the performances of the BESS control algorithm presented in the previous chapter. The VGM algorithm is tested both in islanded configuration and grid connected one in order to show the ability of a proper resynchronization. In the grid connected configuration also the BESS pre-load is considered.
**Personal contribution:** I have developed all the MATLAB/Simulink model, the control tuning and I have chosen all the scenarios to test the proposed control scheme. I have performed all the simulations.

## 4.1 Islanded Configuration

In this operating scenario the BESS converter is in islanded configuration, at $t = 2s$ a three phase load is connected to the converter, while at $t = 4s$ a three phase symmetrical fault occurs at the common busbar. A previous load connection is implemented in order to stress the control algorithm, i.e., a pre-load configuration brings to have Governor and AVR working with active and reactive powers respectively and this can reduce the possibility of the converter to manage properly the fault event. In order to show the proper performance of the proposed algorithm four different test cases are considered:

- **Test Case A**: Inertia and Rotor Flux parameters are not modified when the fault is detected and Governor and AVR outputs are not frozen when the fault is detected. This is the situation with a standard virtual synchronous generator algorithm;

- **Test Case B**: Inertia and Rotor Flux parameters are not modified when the fault is detected while Governor and AVR outputs are frozen when the fault is detected. The freezing control action, as explained in the previous chapter, consists in putting to zero the Governor and AVR input as described by relations (3.31) and (3.32);
- **Test Case C**: Inertia and Rotor Flux parameters are modified when the fault is detected while Governor and AVR outputs are not frozen when the fault is detected;
- **Test Case D**: Inertia and Rotor Flux parameters are modified when the fault is detected and Governor and AVR outputs are frozen when the fault is detected;

### 4.1.1 Test Case A - The base case

In this configuration the Inertia and Rotor Flux values are the standard one and freezing actions of Governor and AVR are not implemented. The currents time profile is reported in figure 4.1 and in figure 4.2 it is possible to see that without correcting actions, voltage $V_{meas}$ and frequency $f_{meas}$ are restored after a long transient of $1s$ and $1.5s$ respectively and this is due to the fact that, as can be easily seen, VGM output $V_{ref,VGM}$ and $f_{ref,VGM}$ have their dynamics because no corrective actions are implemented.

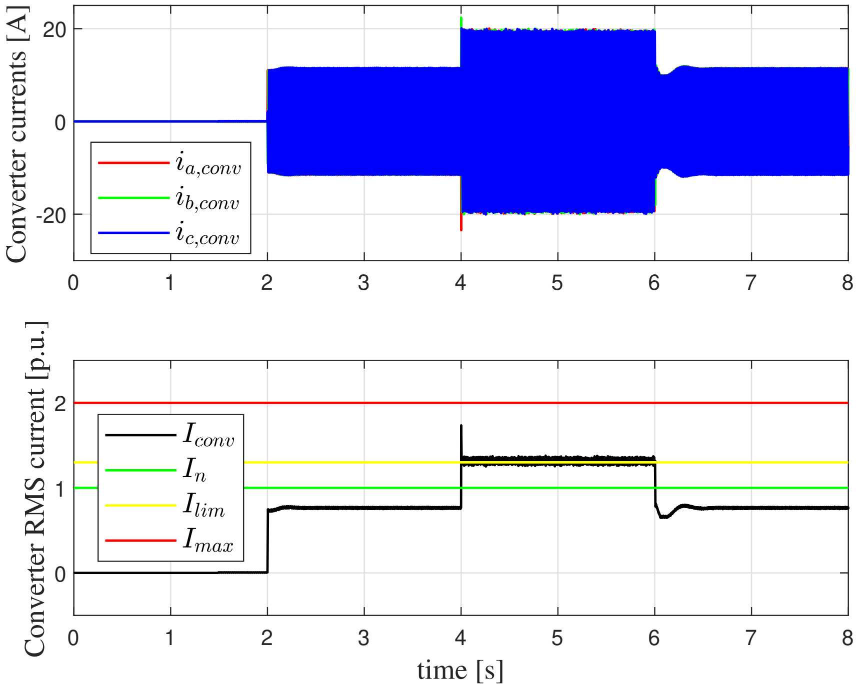

FIGURE 4.1: Currents during faults in Test Case A.

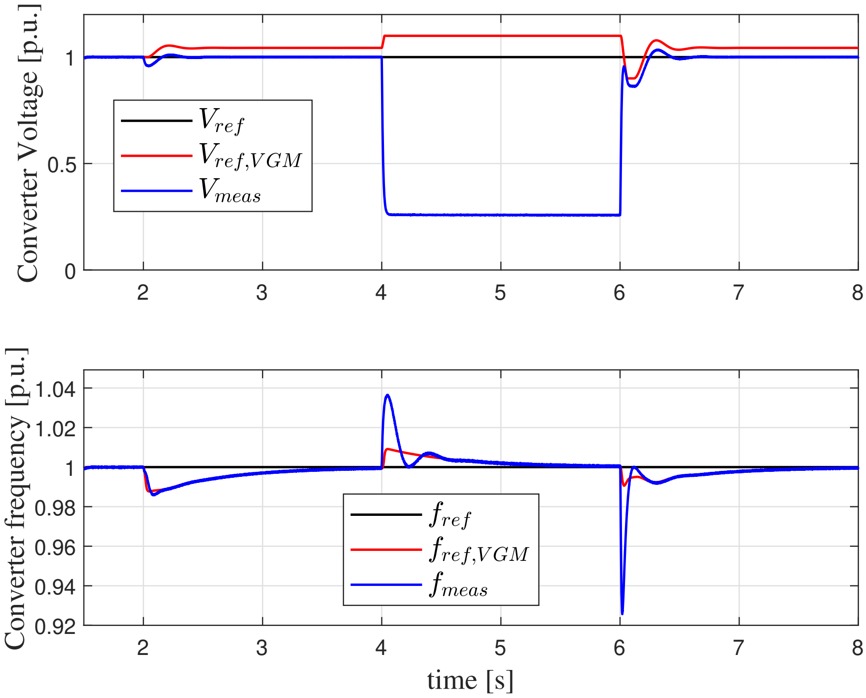

FIGURE 4.2: Voltage and current during faults in Test Case A.

### 4.1.2 Test Case B - Freezing actions case

In this configuration the Inertia and Rotor Flux values are the standard one, but freezing actions of Governor and AVR are implemented. The currents time profile is reported in figure 4.3 and in figure 4.4 it is possible to see that only with freezing actions, voltage $V_{meas}$ and frequency $f_{meas}$ are restored after a long transient and this is due to the fact that, as can be easily seen, VGM output $V_{ref,VGM}$ and $f_{ref,VGM}$ are not blocked when the fault is detected and moreover they reach their respective maximum limits which is only accepted in the islanded stand-alone case. If the BESS converter is running islanded in parallel with a conventional synchronous generator it would desynchronise surely.

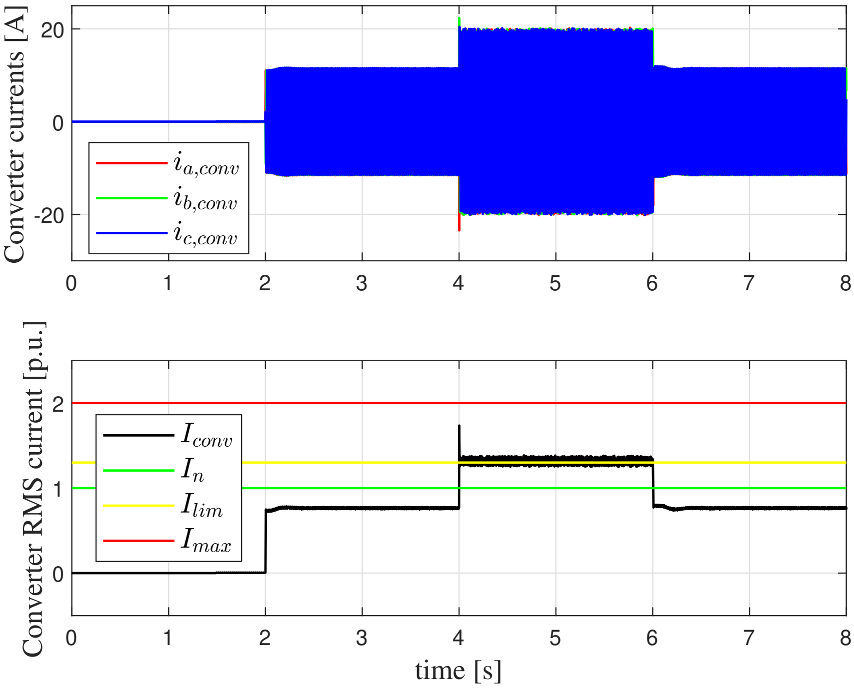

FIGURE 4.3: Currents during faults in Test Case B.

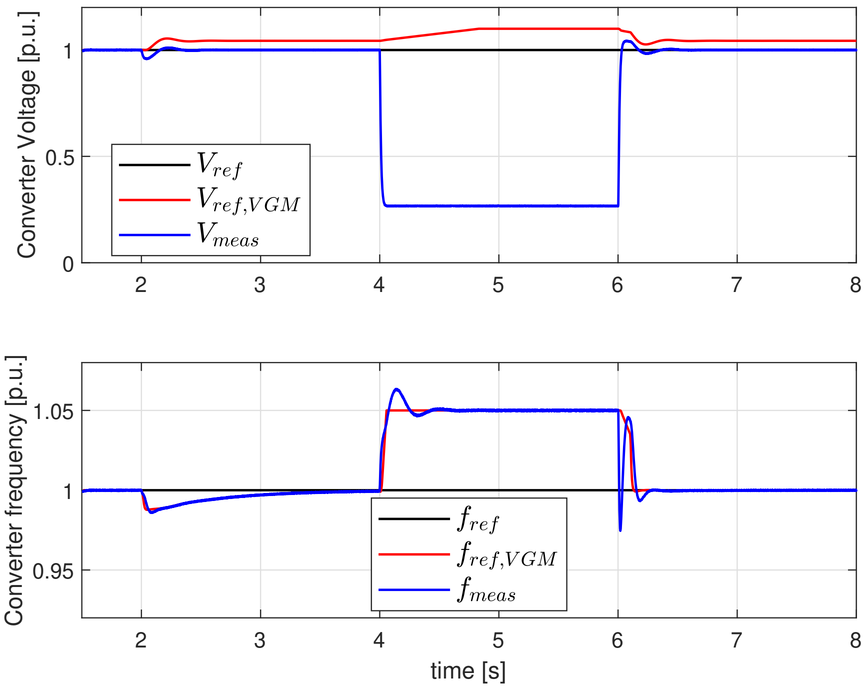

FIGURE 4.4: Voltage and current during faults in Test Case B.

### 4.1.3 Test Case C - Parameters modification case

In this configuration the Inertia and Rotor Flux values are modified, but freezing actions of Governor and AVR are not implemented. The currents time profile is reported in figure 4.5 and in figure 4.6 it is possible to see that only with parameters modification, voltage $V_{meas}$ and frequency $f_{meas}$ are restored after a long transient but shorter than test case A.

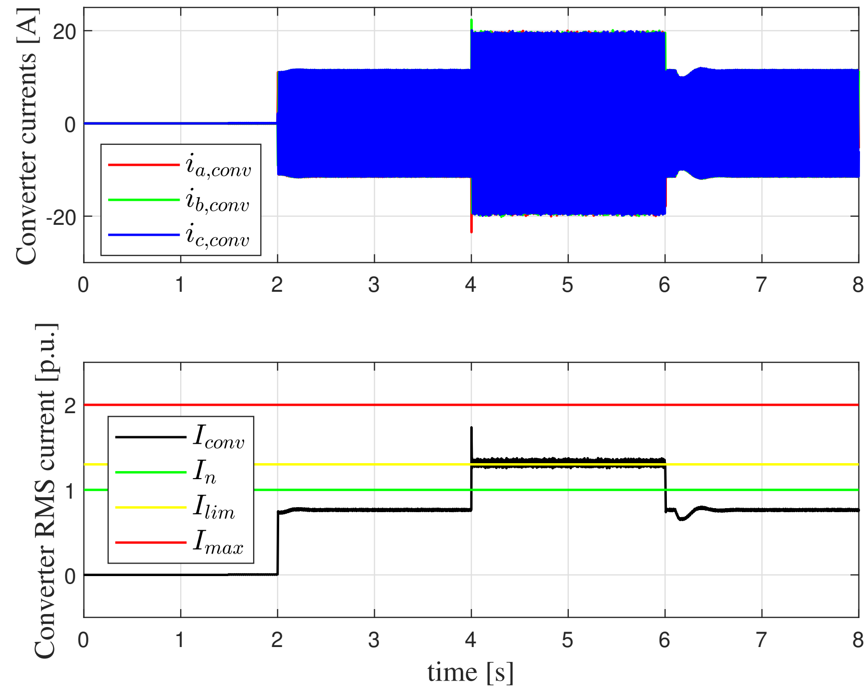

FIGURE 4.5: Currents during faults in Test Case C.

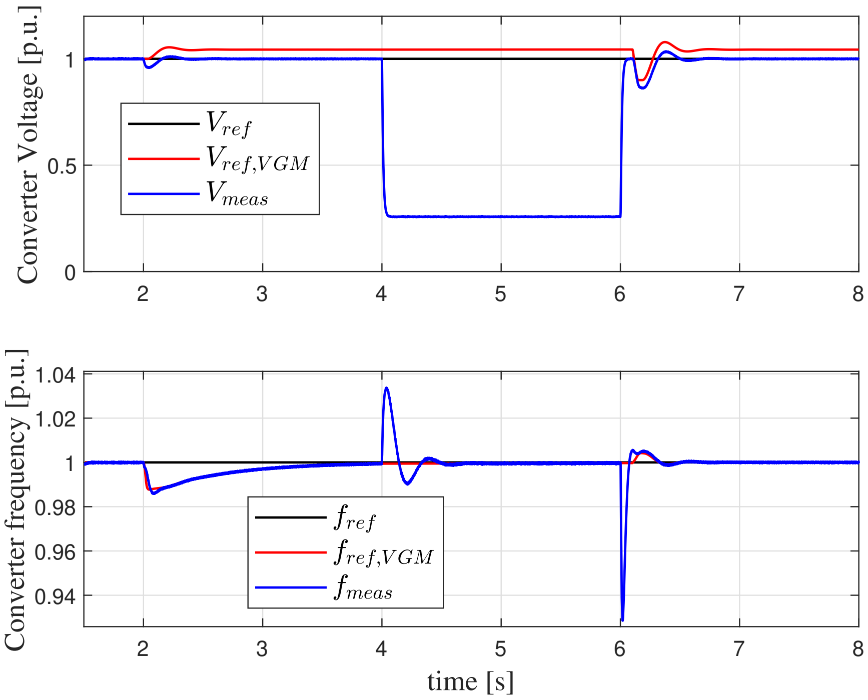

FIGURE 4.6: Voltage and current during faults in Test Case C.

### 4.1.4 Test Case D - Complete case

In this configuration the Inertia and Rotor Flux values are modified, freezing actions of Governor and AVR outputs are implemented. The currents time profile is reported in figure 4.7 and in figure 4.8 it is possible to see that with the combination of the two strategies, voltage ($V_{meas}$) and frequency ($f_{meas}$) are restored with fast and smooth transient, more precisely the frequency is restored in $250ms$ while the voltage in $150ms$.

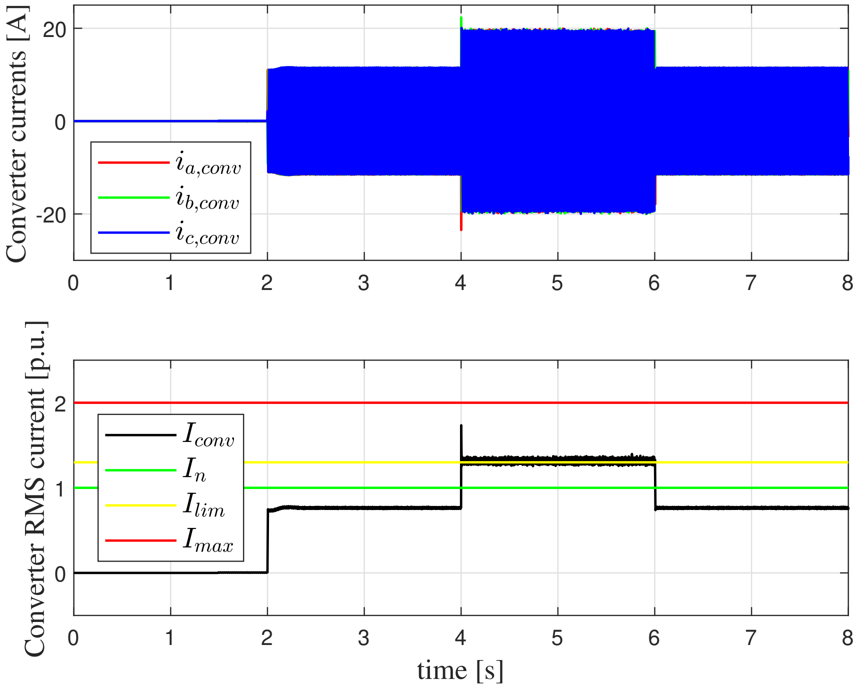

FIGURE 4.7: Currents during faults in Test Case D.

A comparison between the four test cases in terms of measured frequencies is reported in figure 4.9, while a comparison between converter voltage after the fault clearing is reported in figure 4.10.

As one can see the strategy implemented in *Test Case D* proposes better performances compared to *Test Case A*, *Test Case B* and *Test Case C*. Considering *Test Case D* converter RMS voltage is restored in about $70ms$ without undershoots or overshoots and also the frequency returns to the previous value in approximately $250ms$ as stated before. Finally, a quantitative comparison in terms of recovery times (r.t.) is reported in table 4.1.

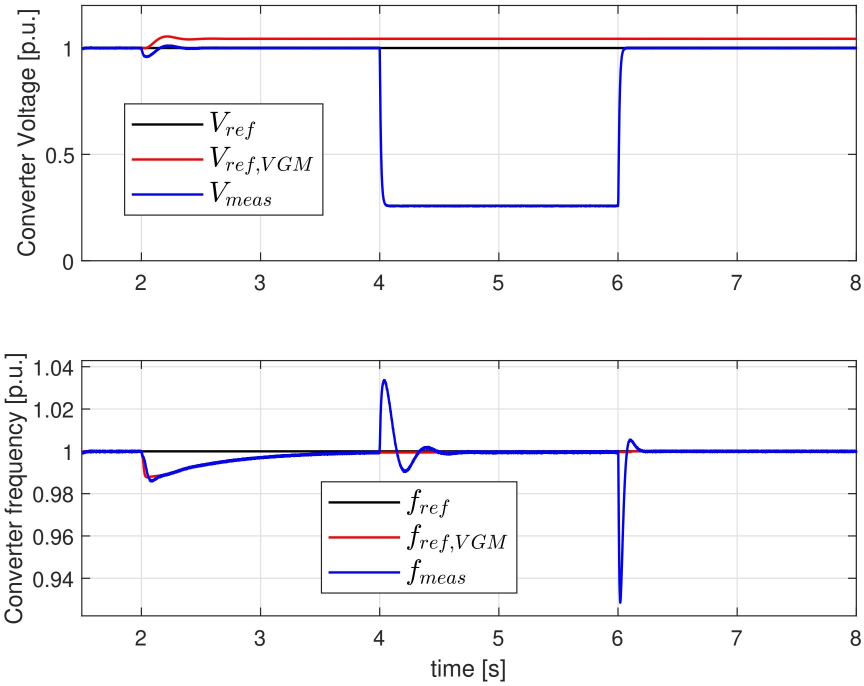

FIGURE 4.8: Voltage and current during faults in Test Case D.

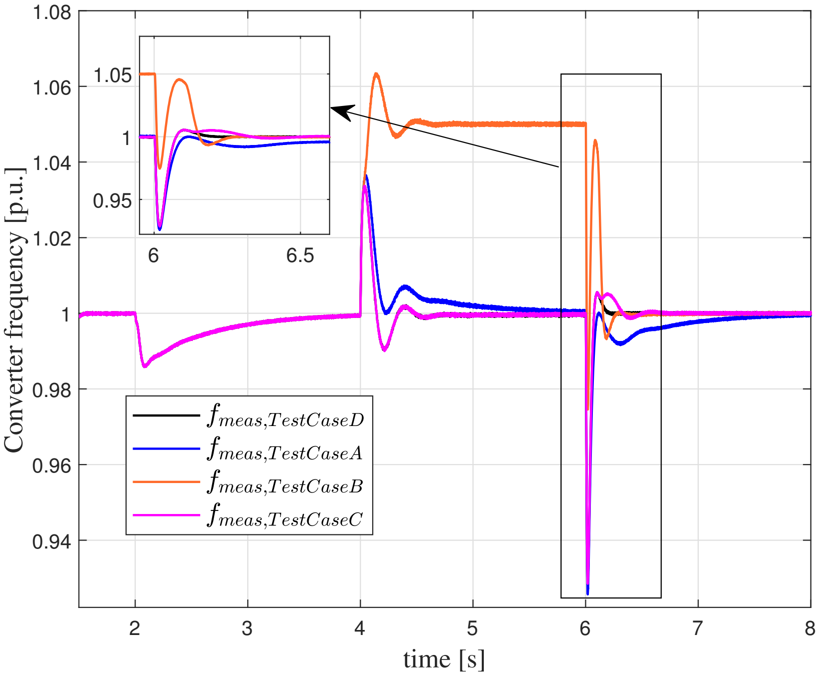

FIGURE 4.9: Frequency during faults: comparison between test cases.

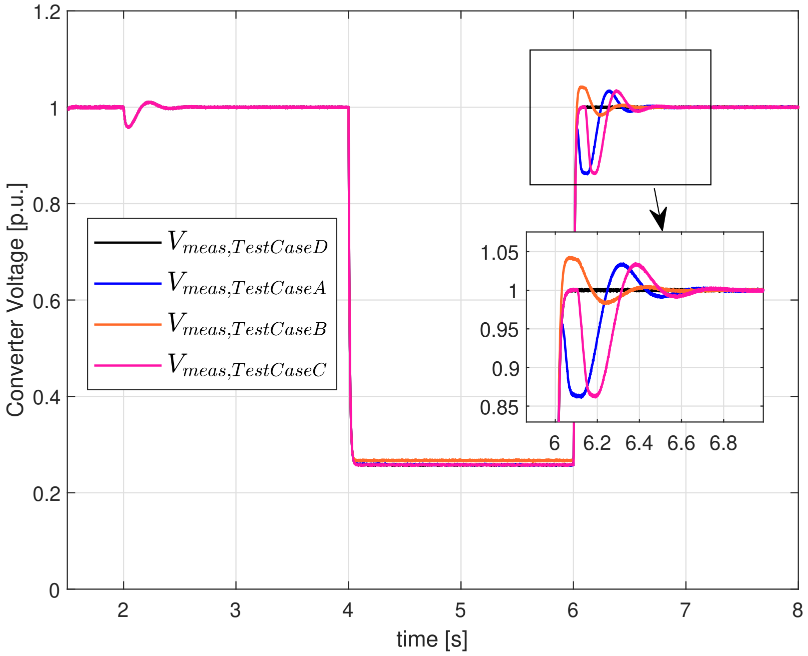

FIGURE 4.10: Voltage during faults: comparison between test cases.

| | **RMS Current r.t.** | **RMS Voltage r.t.** | **Frequency r.t.** |
|---|---|---|---|
| **Test Case A** | $800ms$ | $1s$ | $1.5s$ |
| **Test Case B** | $600ms$ | $600ms$ | $600ms$ |
| **Test Case C** | $800ms$ | $1s$ | $800ms$ |
| **Test Case D** | $40ms$ | $70ms$ | $250ms$ |

TABLE 4.1: Comparative analysis in islanded configuration.

## 4.2 Grid-Connected Configuration

In order to test the correct behaviour of the BESS converter during fault in a Grid-Connected configuration, a non-deal external grid is considered as one can see in the voltage time profile depicted in figure 4.11. The grid voltage contains a $7^{th}$ harmonic with an amplitude of 10 V and a $13^{th}$ harmonic with an amplitude of 20 V. Moreover, a random noise voltage $(NV)$ limited between $-10$ V and $+10$ V is added to each phases as reported in (4.1).

$$v_{abc,grid}(t) = \begin{bmatrix} \frac{V_n\sqrt{2}}{\sqrt{3}}\sin\left(\omega_n t\right) + 10\sin\left(7\omega_n t\right) + 20\sin\left(13\omega_n t\right) + NV \\ \frac{V_n\sqrt{2}}{\sqrt{3}}\sin\left(\omega_n t - \frac{2\pi}{3}\right) + 10\sin\left(7\omega_n t - \frac{2\pi}{3}\right) + 20\sin\left(13\omega_n t - \frac{2\pi}{3}\right) + NV \\ \frac{V_n\sqrt{2}}{\sqrt{3}}\sin\left(\omega_n t + \frac{2\pi}{3}\right) + 10\sin\left(7\omega_n t + \frac{2\pi}{3}\right) + 20\sin\left(13\omega_n t + \frac{2\pi}{3}\right) + NV \end{bmatrix} \tag{4.1}$$

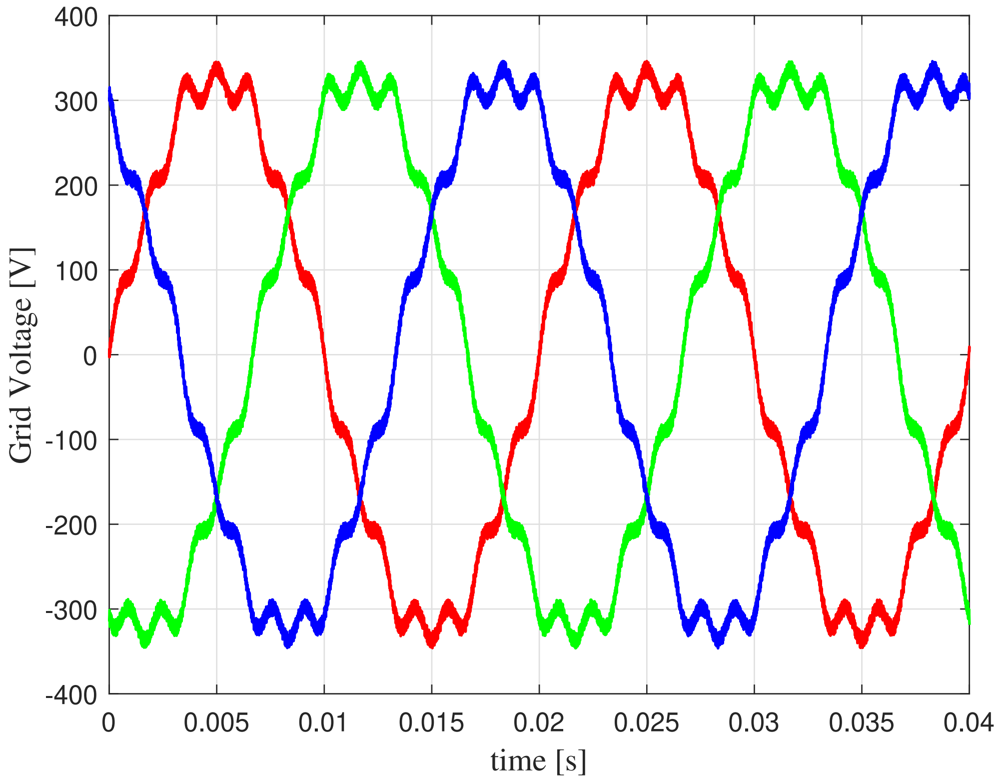

FIGURE 4.11: External grid voltage time profile.

As in the previous section for the islanded configuration, the test cases are organized as follows:

- **Test Case A**: Inertia and Rotor Flux parameters are not modified when the fault is detected and Governor and AVR outputs are not frozen when the fault is detected;
- **Test Case B**: Inertia and Rotor Flux parameters are not modified when the fault is detected while Governor and AVR outputs are frozen when the fault is detected;

- **Test Case C**: Inertia and Rotor Flux parameters are modified when the fault is detected while Governor and AVR outputs are not frozen when the fault is detected;
- **Test Case D**: Inertia and Rotor Flux parameters are modified when the fault is detected and Governor and AVR outputs are frozen when the fault is detected;

### 4.2.1 Test Case A - The base case

In this configuration the converter is connected to an external grid (with noise and harmonics in order to test to robustness of the proposed controller and strategy). A symmetrical three-phase fault occurs at $t = 2s$ and it is removed after $0.5s$. The inertia and rotor flux values are the standard one and Governor and AVR outputs are not frozen when the fault is detected. In figure 4.12 it is possible to see that in this configuration the converter is able to restore the current previous the fault but with a long transient of about $0.5s$. This transient resynchronizing current duration is not admissible, in fact several standard require that the transient resynchronising current in grid connected configuration to be over within $100ms$. Moreover is possible to see that the converter is still in current limit also after $60ms$ from the fault clearance because when the fault is cleared, the converter is not synchronized with the external main grid. Even if voltage and frequency level are restored, see figure 4.13, a transient of $0.5s$ for the voltage and $0.6s$ for the frequency are not acceptable because it can lead to a severe MG instability.

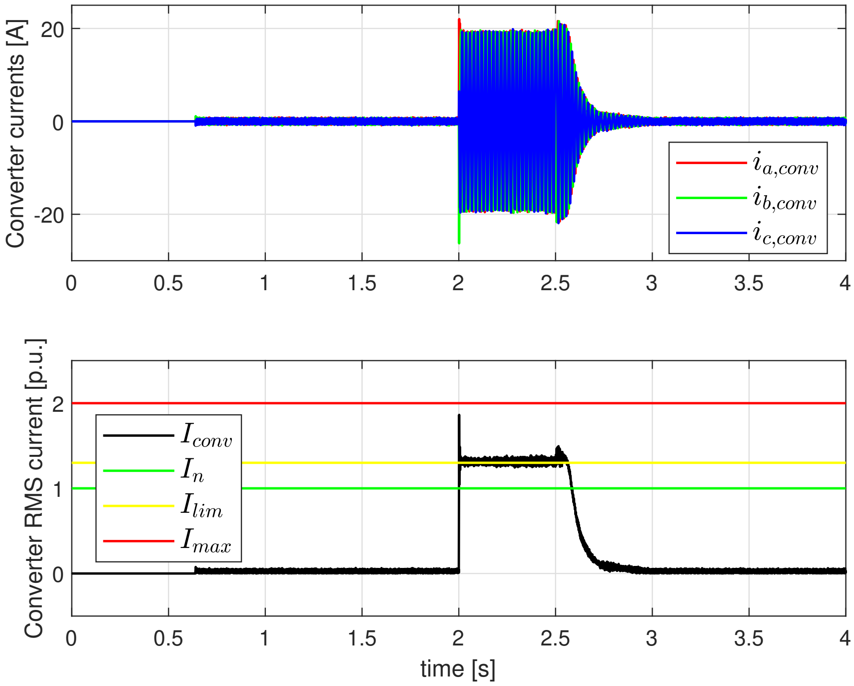

FIGURE 4.12: Currents during faults in Test Case A.

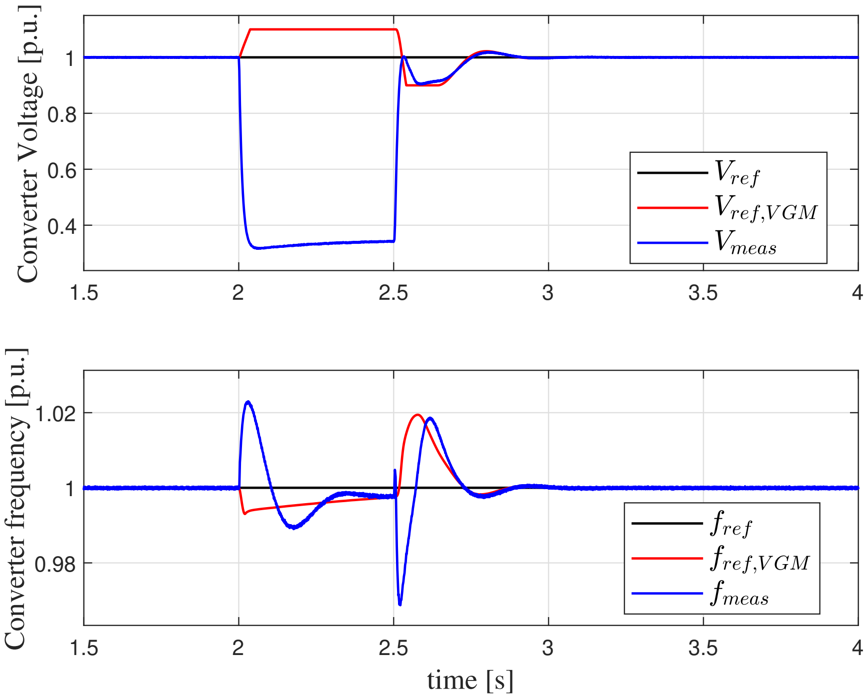

FIGURE 4.13: Voltage and current during faults in Test Case A.

The resynchronization with the external grid can be properly shown considering the angle difference between the VGM out $\theta_{ref,VGM}$ and the grid angle measured at the end of the grid line $\theta_{grid}$. The VGM algorithm is able to resynchronize with the external grid only after a long transient that is not acceptable as it is shown in figure 4.14. The long transient is due to the fact that during fault the VGM frequency $f_{ref,VGM}$ decreases because the inertia value is not modified, and this produce a fast variation in the angle $\theta_{ref,VGM}$ and so in the angle difference. The problem of the resynchronization can be also appreciated in the active and reactive powers dynamic as depicted in figure 4.15.

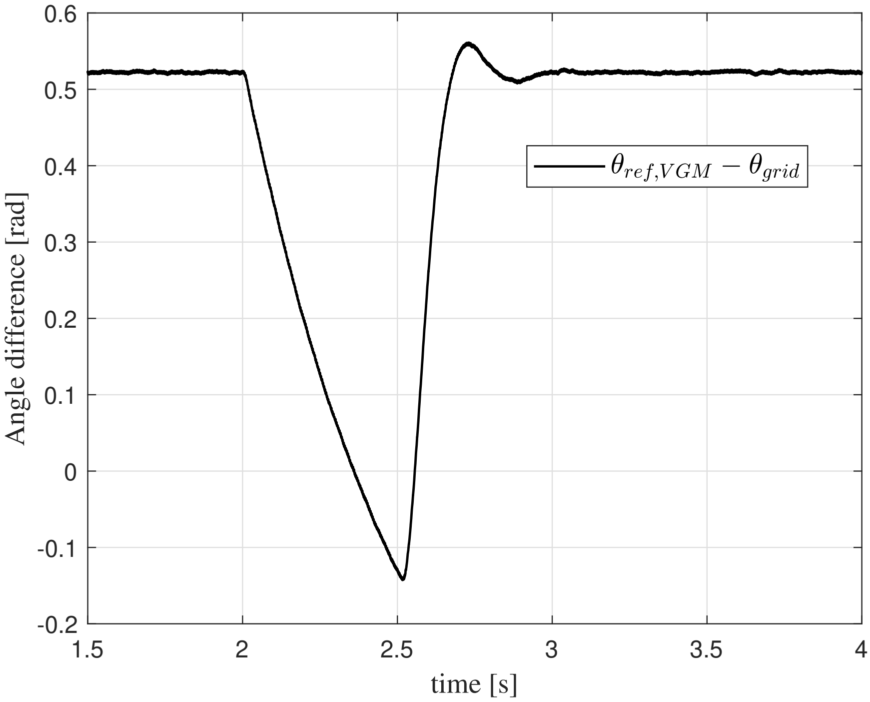

FIGURE 4.14: Angle during faults in Test Case A

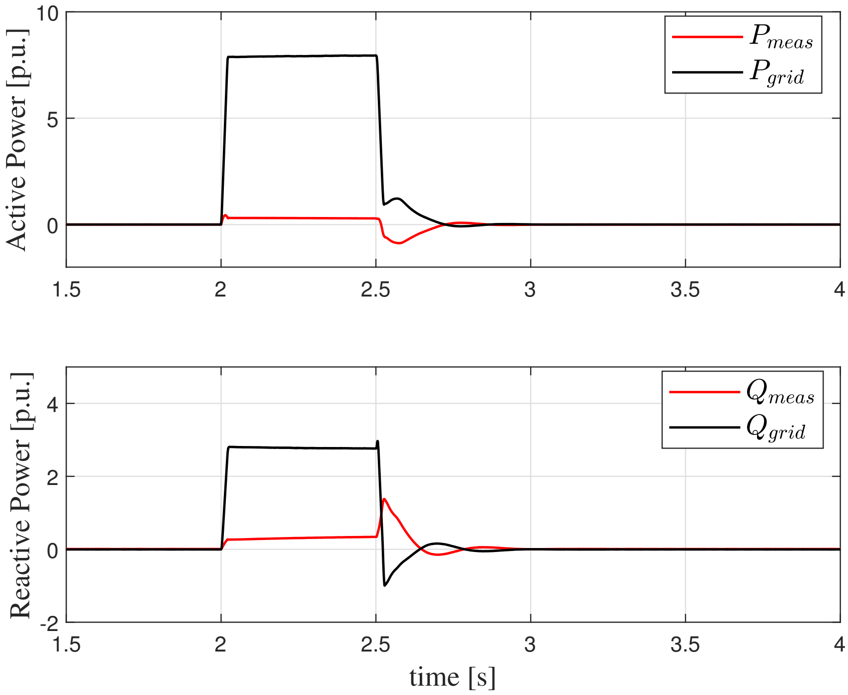

FIGURE 4.15: Active and reactive powers during faults in Test Case A (powers are measured at the output of the converter and at the external grid connection.)

### 4.2.2 Test Case B - Freezing actions case

In this configuration the converter is connected to an external grid. A symmetrical three-phase fault occurs at $t = 2s$ and it is removed after $0.5s$. The Inertia and Rotor Flux values are the standard ones while Governor and AVR outputs are frozen when the fault is detected. In figure 4.16 it is possible to see that in this configuration the converter is not able to restore the current previous the fault and the requirement of a transient duration lower than $100ms$ is not guaranteed. Voltage and frequency time profiles are reported in 4.17 and, as one can see both the VGM output $V_{ref,VGM}$ and $f_{ref,VGM}$ reach their lower limits of $0.9p.u.$ and $0.95p.u.$ when the fault occurs. This is due to the fact that when the fault is detected the Governor and AVR outputs $P_{GOV}^{BESS}$ and $Q_{AVR}^{BESS}$ are frozen to respective their values previous the fault according to relations (3.31) and (3.32) and this produces a strong variation on the VGM output because the inertia and rotor flux constant $K_H$ and $K_\Psi$ are not modified. Of course this huge variations during the fault are not acceptable for the resynchronization with the external grid, in fact this simulation presents a *pole slipping* event as depicted in figure 4.18 and this is the cause of the different RMS current when the fault is cleared.

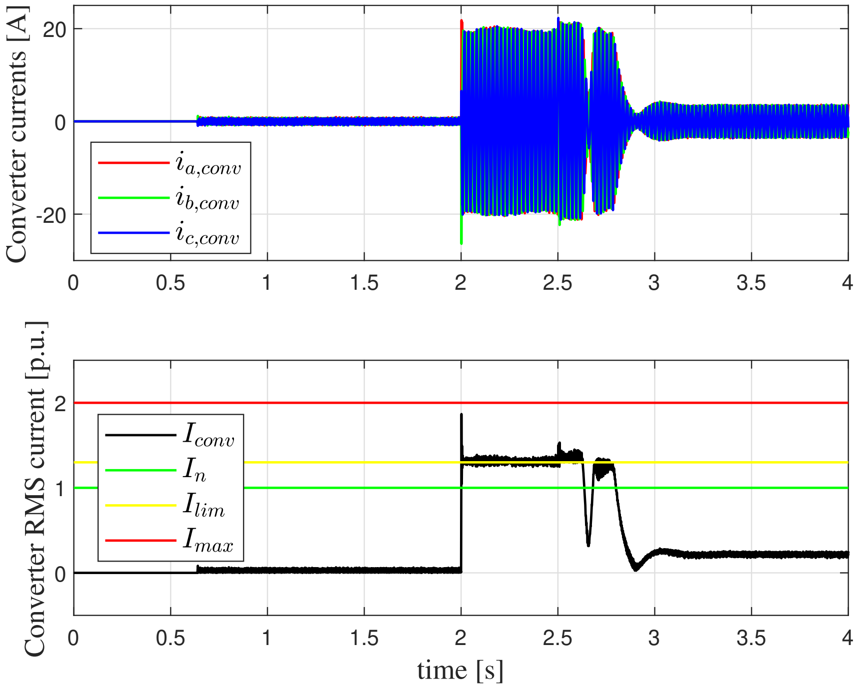

FIGURE 4.16: Currents during faults in Test Case B.

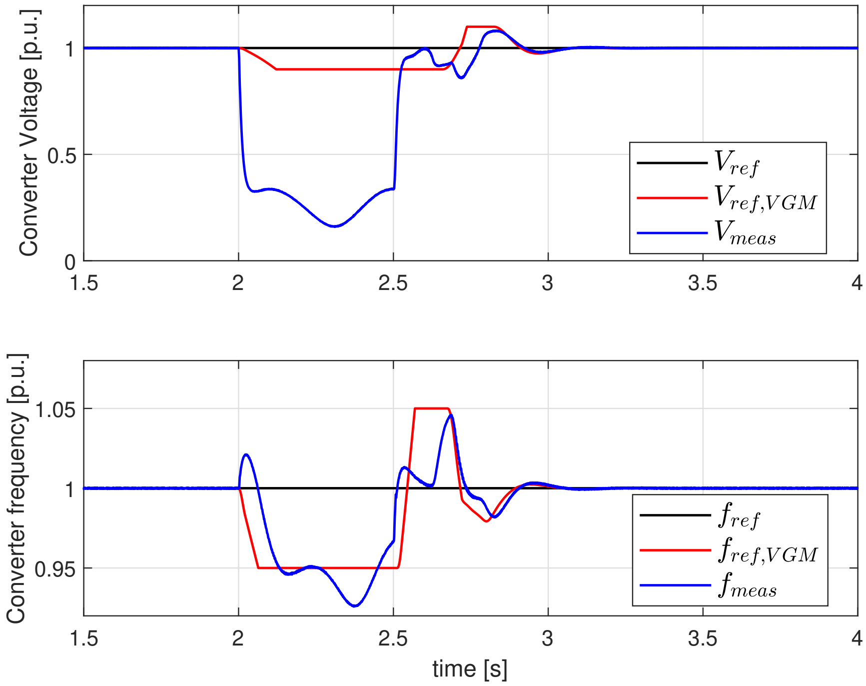

FIGURE 4.17: Voltage and frequency during faults in Test Case B.

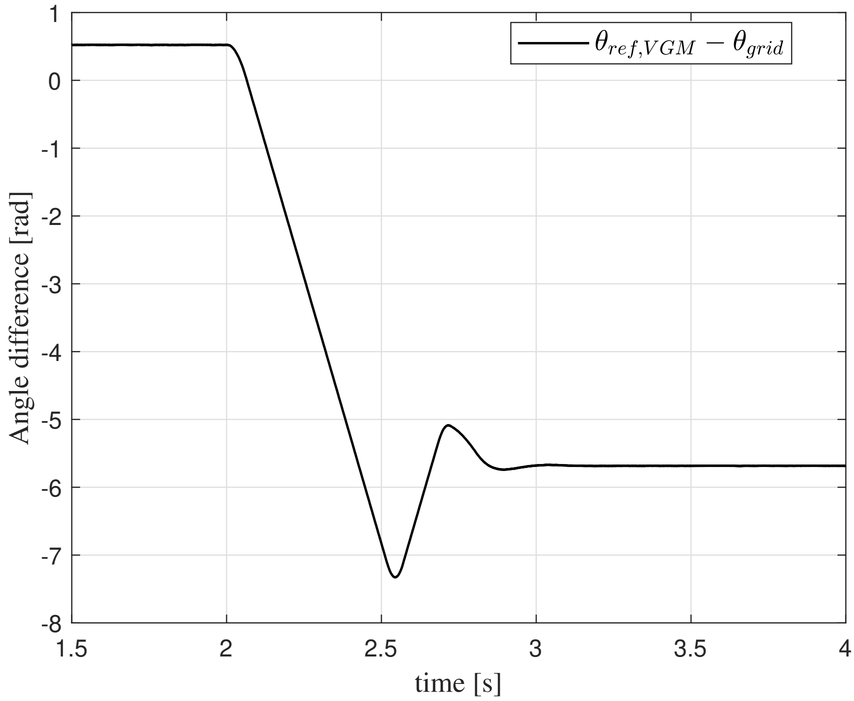

FIGURE 4.18: Angle difference during faults in Test Case B.

### 4.2.3 Test Case C - Parameters modification case

In this configuration the converter is connected to an external grid. A symmetrical three-phase fault occurs at $t = 2s$ and it is removed after $0.5s$. The Inertia and Rotor Flux values are modified when the fault is detected while Governor and AVR outputs are not frozen when the fault is detected. In figure 4.19 it is possible to see the dynamic behaviour of converter currents: as can be easily seen in $30ms$ after the fault clearing the converter current return at the previous value but at $2.6s$ it is possible to see a bump in the currents. This is due to the fact that at $2.6s$ inertia and rotor flux variables $K_H$ and $K_\Psi$ return to their rated values but the actions of Governor and AVR are not blocked, i.e. outputs $P_{GOV}^{BESS}$ and $Q_{AVR}^{BESS}$ are not frozen to respective their values previous the fault and so this current bump is imposed by the control when $K_H$ and $H_\Psi$ return to their rated values and by the Governor and AVR input $e_{GOV}$ and $e_{AVR}$ that are non-zero. The effect of this parameter modification is also visible in voltage and frequency time profiles reported in figure 4.20, and in the angle difference depicted in figure 4.21.

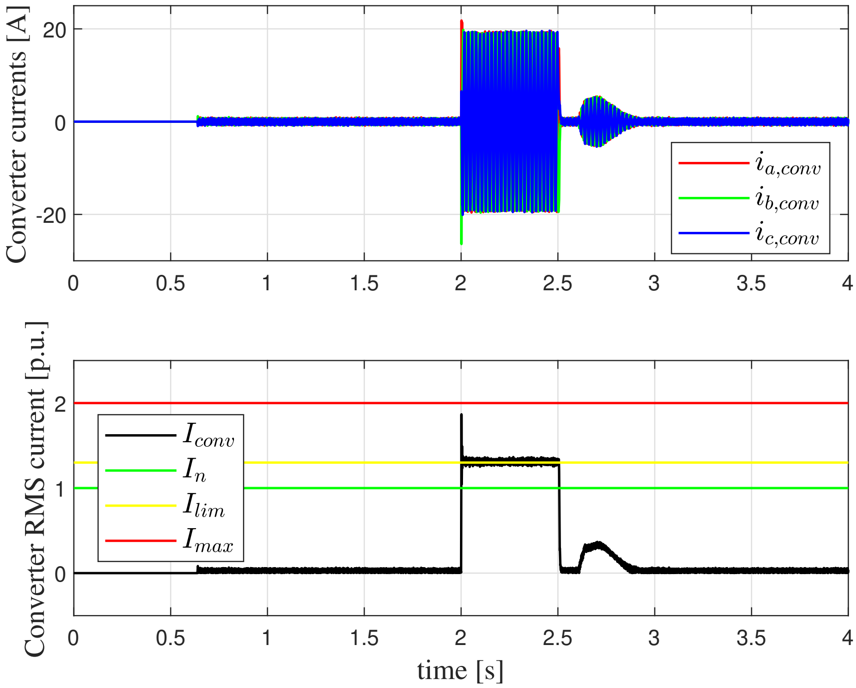

FIGURE 4.19: Currents during faults in Test Case C.

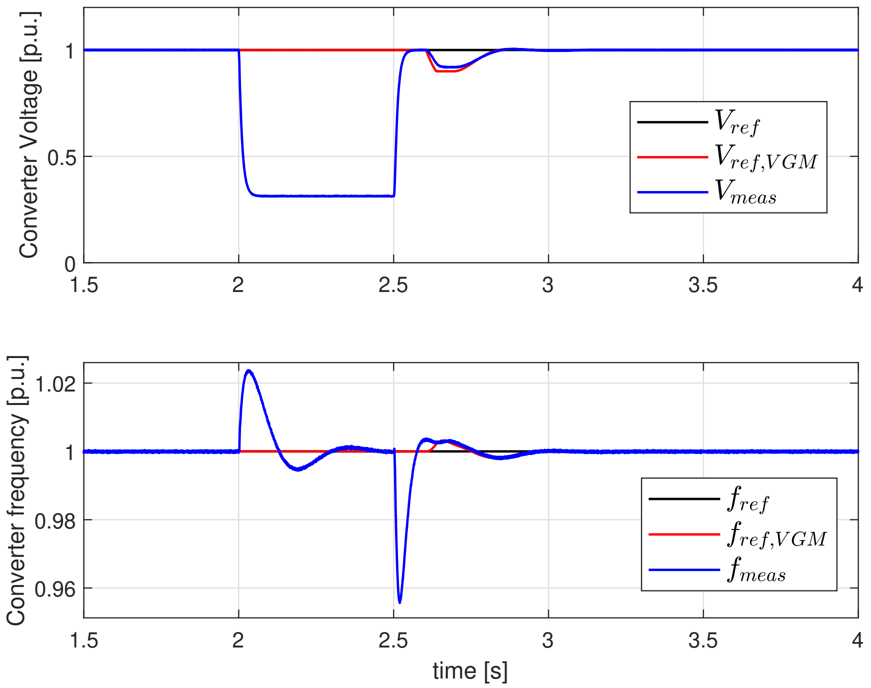

FIGURE 4.20: Voltage and frequency during faults in Test Case C.

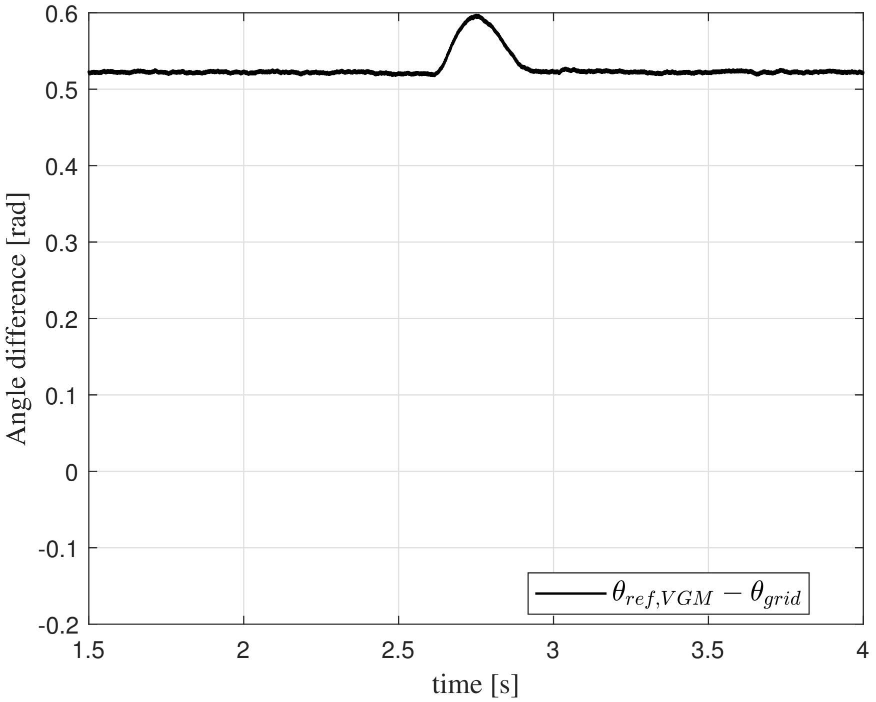

FIGURE 4.21: Angle difference during faults in Test Case C.

### 4.2.4 Test Case D - Complete case

In this configuration the converter is connected to an external grid. A symmetrical three-phase fault occurs at $t = 2s$ and it is removed after $0.5s$. The Inertia and Rotor Flux values are modified when the fault is detected and Governor and AVR outputs are frozen when the fault is detected. In figure 4.22 it is possible to see that in this configuration the converter is able to restore with fast and smooth dynamics the current previous fault in less than $30ms$ as depicted in figure 4.23 and comparison with the other test cases is depicted in 4.24. Voltage and frequency level are restored after a short transient, see figure 4.25. More precisely the RMS voltage $V_{meas}$ is restored in less than $100ms$ while the measured frequency $f_{meas}$ after $250ms$. It is possible to see also an overshoot in $f_{meas}$ up to $1.004p.u.$ during the clearing phase: this is due to the dynamic of the PLL, and not to the control algorithm. Moreover, a comparison in terms of the voltage recovery between test cases is depicted in figure 4.26 and the best performance can be appreciated in *Test Case D*. The VGM algorithm is able to resynchronize with the external grid after a very short dynamic as it is shown in figure 4.27 in terms of angle difference. A quantitative comparison in terms of r.t. is reported in table 4.2.

| | **RMS Current r.t.** | **RMS Voltage r.t.** | **Frequency r.t.** |
|---|---|---|---|
| **Test Case A** | $500ms$ | $500ms$ | $600ms$ |
| **Test Case B** | $900ms$ | $900ms$ | $900ms$ |
| **Test Case C** | $500ms$ | $800ms$ | $800ms$ |
| **Test Case D** | $30ms$ | $100ms$ | $250ms$ |

Table 4.2: Comparative analysis in grid connected configuration.

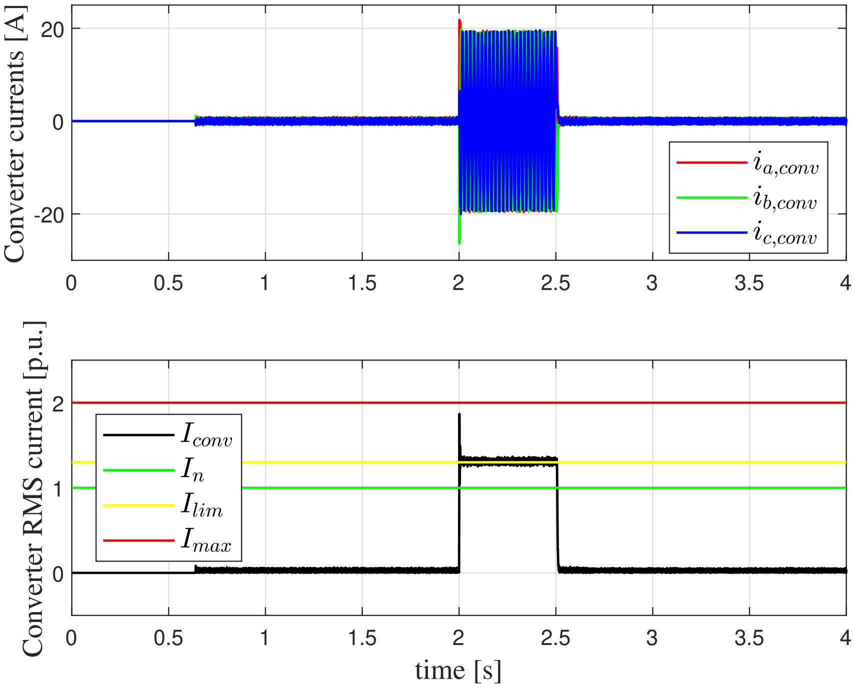

FIGURE 4.22: Currents during faults in Test Case D.

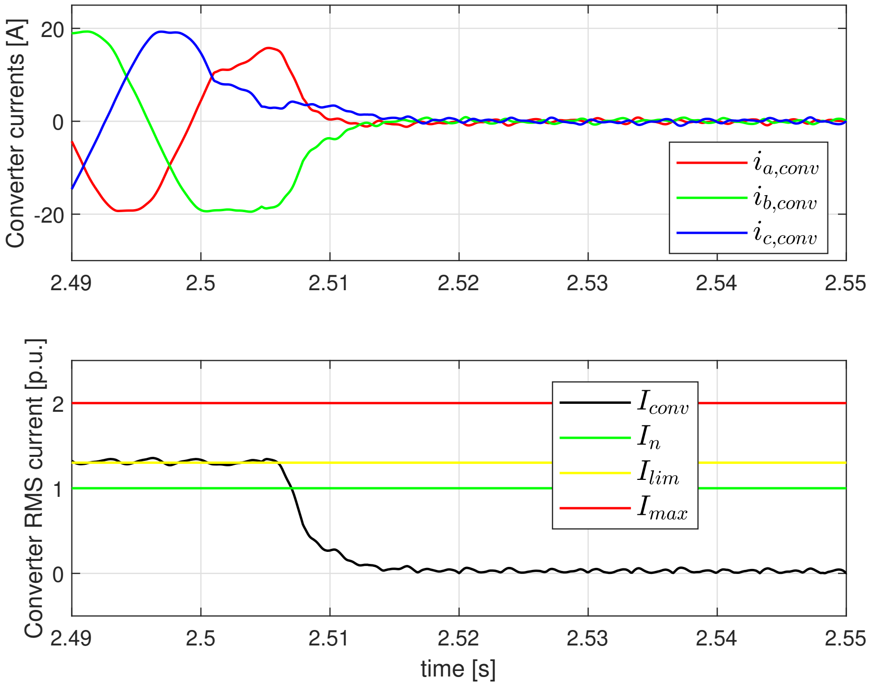

FIGURE 4.23: Currents during faults in Test Case D: detail on resynchronization phase.

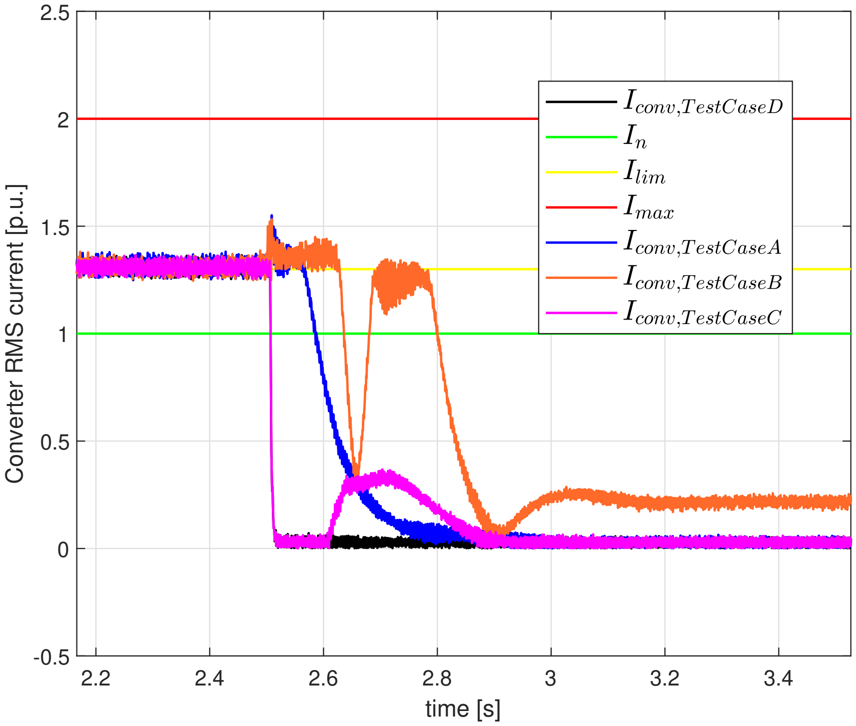

FIGURE 4.24: Currents during faults: comparison between test cases.

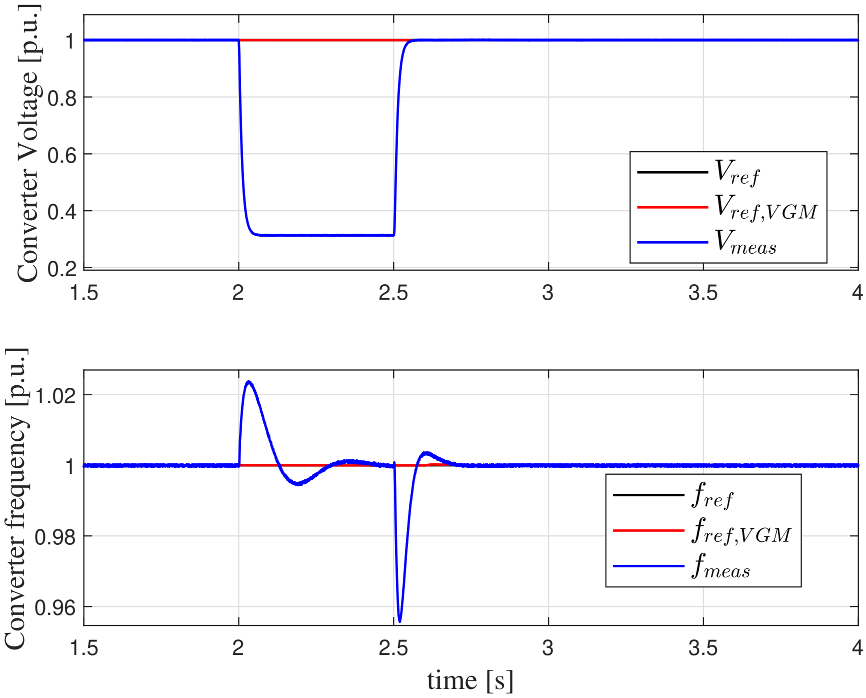

FIGURE 4.25: Voltage and frequency during faults in Test Case D.

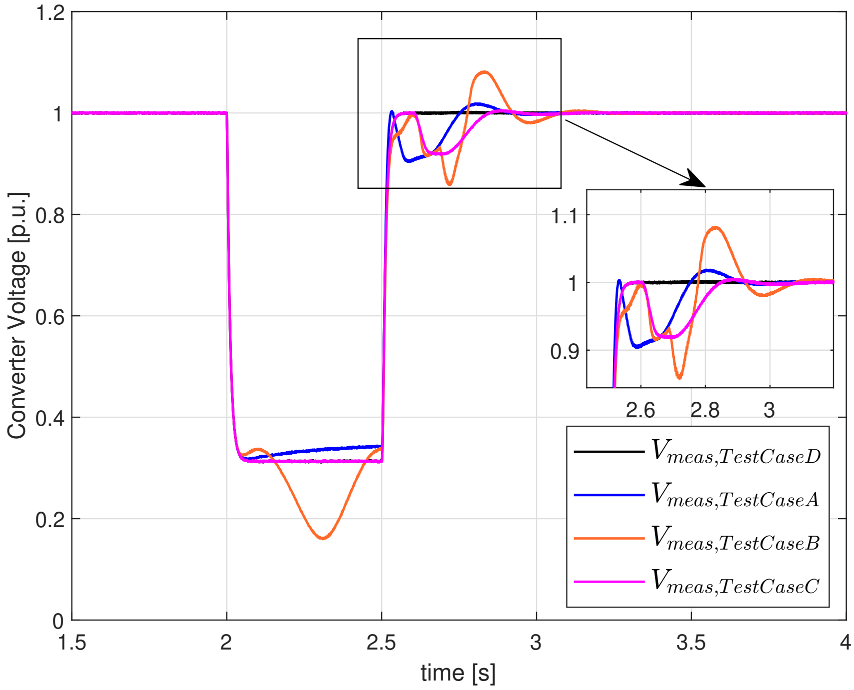

FIGURE 4.26: RMS Voltages during faults: comparison between test cases.

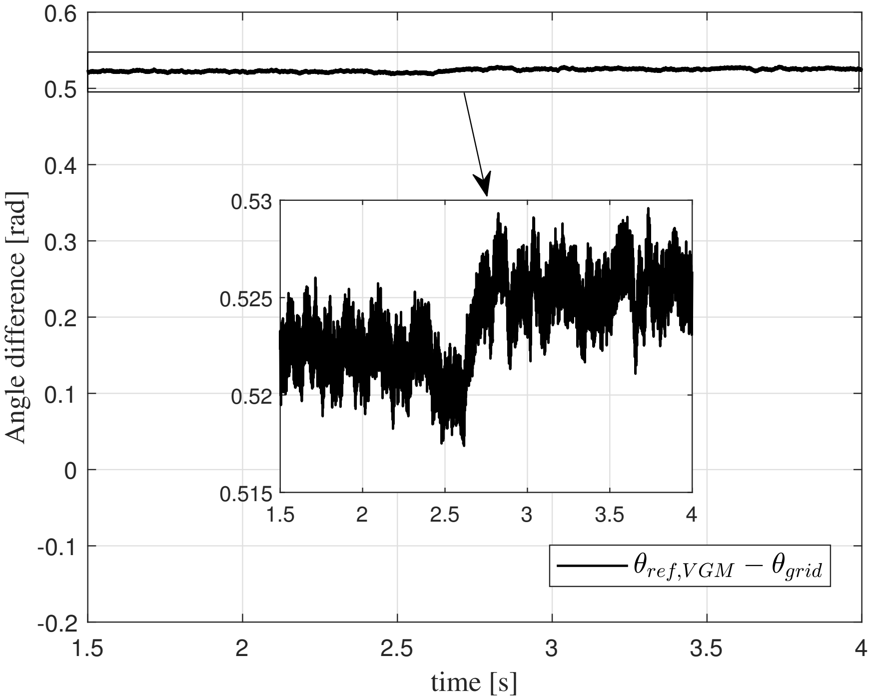

FIGURE 4.27: Angle difference during faults in Test Case D.

## 4.3 Grid-Connected Configuration: BESS pre-load producing power

In this subsection another interesting scenario is analysed when a fault event occurs. In this scenario the BESS converter is in a grid connected configuration but the initial working point is not a no-load, i.e. the converter is in the pre-load configuration, more precisely a pre load of $+0.3p.u.$ active power and of $-0.2p.u.$ reactive power. This is a challenging test case to prove the correct behaviour of the proposed VGM algorithm in terms of current limiting and resynchronization capability. Also this section is organized according to the four different test cases, namely *Test Case A*, *Test Case B*, *Test Case C* and *Test Case D* and in every test cases the active power production of the BESS is performed with a variation of the VGM algorithm input signal $f_{ref}$ at $t = 2s$ from 50 Hz to 50.5 Hz and having the active power droop parameter $m_{droop}$ non-zero.

### 4.3.1 Test Case A - The base case

In this configuration the converter is connected to an external grid. A symmetrical three-phase fault occurs at $t = 6s$ and it is removed after $0.5s$. The inertia and rotor flux values are the standard one and Governor and AVR outputs are not frozen when the fault is detected. In figure 4.28 it is possible to see that in this configuration the converter is able to restore the current previous the fault but with a long transient. This is due to the fact that in this simulation no corrective actions are implemented, so the Governor and AVR try to control frequency and voltage respectively during the fault and this aspect does not guarantee a fast current restoration, more precisely the current in this base case is restored in $600ms$, i.e. six times greater than the maximum acceptable time. Even if voltage and frequency level are restored, see figure 4.29, the VGM algorithm is able to resynchronize with the external grid only after a long transient that is not acceptable as it is shown in figure 4.30. As one can see when the fault occurs the angle difference $\theta_{ref,VGM} - \theta_{grid}$ starts to decrease because the VGM output $f_{ref,VGM}$ decreases quickly because the inertia parameter $K_H$ is not modified in this base case. This decrease is the main cause of the slowness of the resynchronization phase.

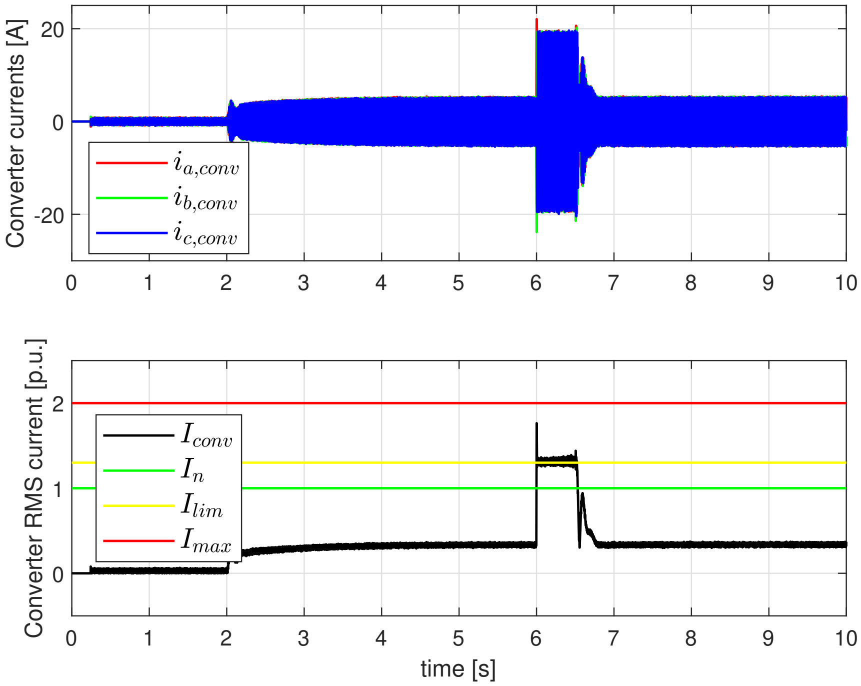

FIGURE 4.28: Currents during faults in Test Case A.

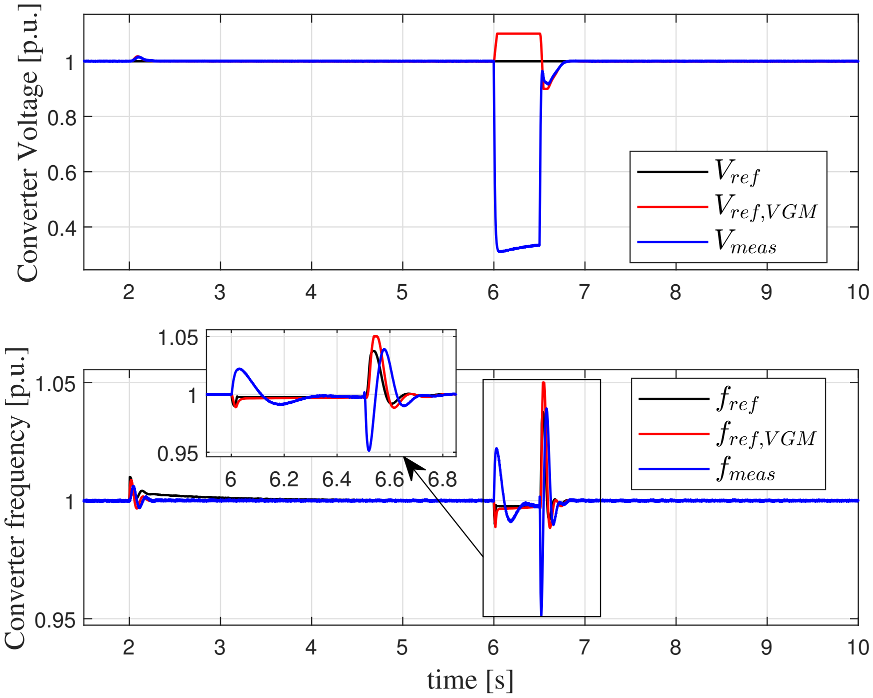

FIGURE 4.29: Voltage and frequency during faults in Test Case A.

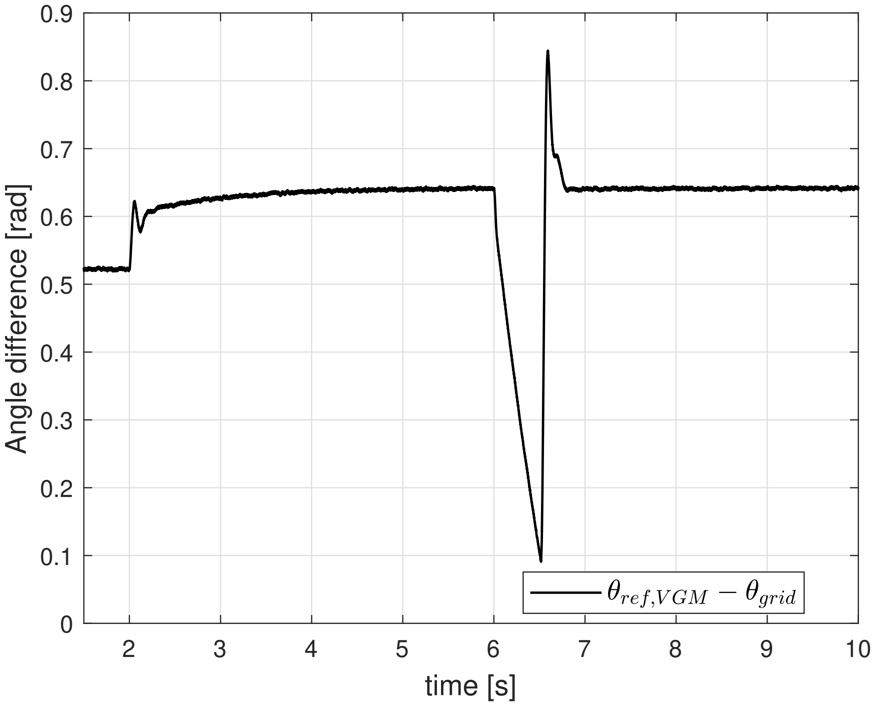

FIGURE 4.30: Angle difference during faults in Test Case A.

### 4.3.2 Test Case B - Freezing actions case

In this configuration the converter is connected to an external grid. A symmetrical three-phase fault occurs at $t = 6s$ and it is removed after $0.5s$. The Inertia and Rotor Flux values are the standard ones and Governor and AVR outputs are frozen when the fault is detected. In figure 4.31 it is possible to see that in this configuration the converter is not able to restore the current previous the fault with fast dynamics. It is possible to see that the converter returns in current limit when Governor and AVR star to regulate again after the freezing actions an it stays in current limit again for $250ms$. This is due to the fact that when the fault is detected the VGM output frequency $f_{ref,VGM}$ starts to decrease quickly because the parameter $K_H$ is not modified and so, when Governor and AVR are reactivated, the converter is not synchronized with the external grid and this cause this long and not acceptable transient. Voltage and frequency time profiles are reported in figure 4.32, and it is possible to see that the voltage output $V_{ref,VGM}$ reach it maximum and minimum value and the same thing can be observed for the frequency output $f_{ref,VGM}$. The incorrect resynchronization phase can be observed in terms of angle difference in figure 4.33.

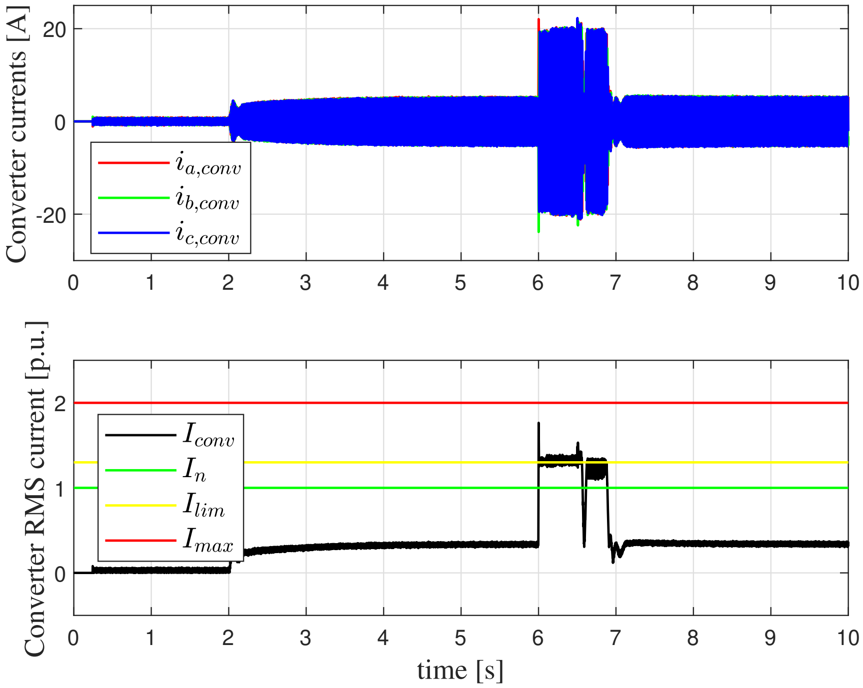

FIGURE 4.31: Currents during faults in Test Case B.

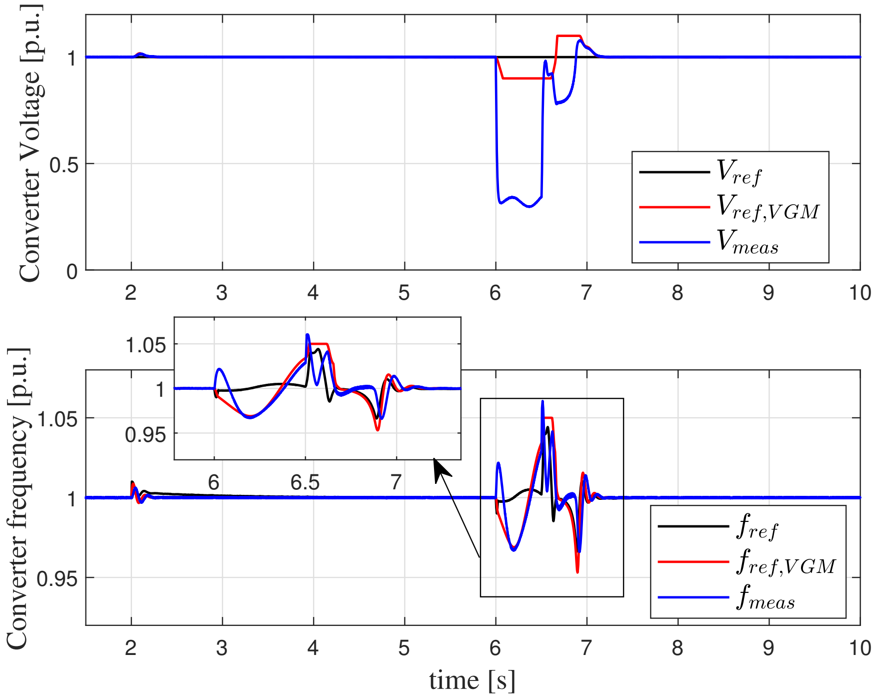

FIGURE 4.32: Voltage and frequency during faults in Test Case B.

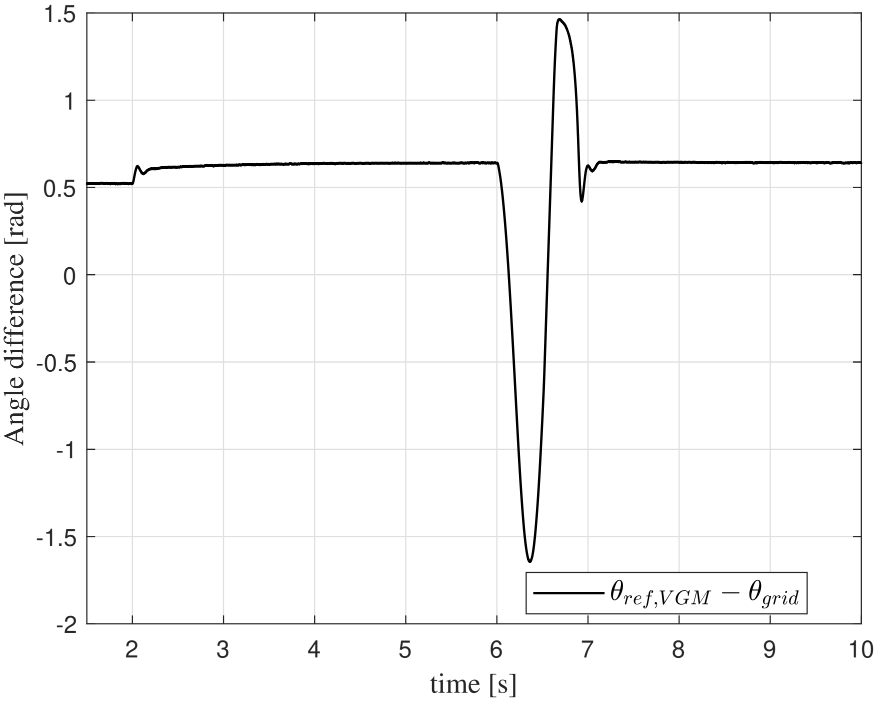

FIGURE 4.33: Angle difference during faults in Test Case B.

### 4.3.3 Test Case C - Parameters modification case

In this configuration the converter is connected to an external grid. A symmetrical three-phase fault occurs at $t = 6s$ and it is removed after $0.5s$. The Inertia and Rotor Flux values are modified when the fault is detected while Governor and AVR outputs are not frozen when the fault is detected. In figure 4.34 it is possible to see the current time profile. Here there something similar to Test Case C in grid connected configuration but with no pre-loading. In $30ms$ after the fault clearing the converter current return at the previous value but at $6.6s$ it is possible to see a bump in the currents. This is due to the fact that at $6.6s$ inertia and rotor flux variables $K_H$ and $H_\Psi$ return to their rated values but the actions of Governor and AVR are not frozen, i.e. outputs $P_{GOV}^{BESS}$ and $Q_{AVR}^{BESS}$ are not blocked to respective their values previous the fault and so this current bump is imposed by the control when $K_H$ and $K_\Psi$ return to their rated values and by the Governor and AVR input $e_{GOV}$ and $e_{AVR}$ that are non-zero. Voltage and frequency time profiles are reported in figure 4.35 and also here it is possible to see the effect of the parameter control modification. The resynchronization with the external grid is depicted in figure 4.36 and it can be appreciated the fact that, when the fault occurs, the angle difference does not decrease and this is due to the modification of the inertia parameter $K_H$.

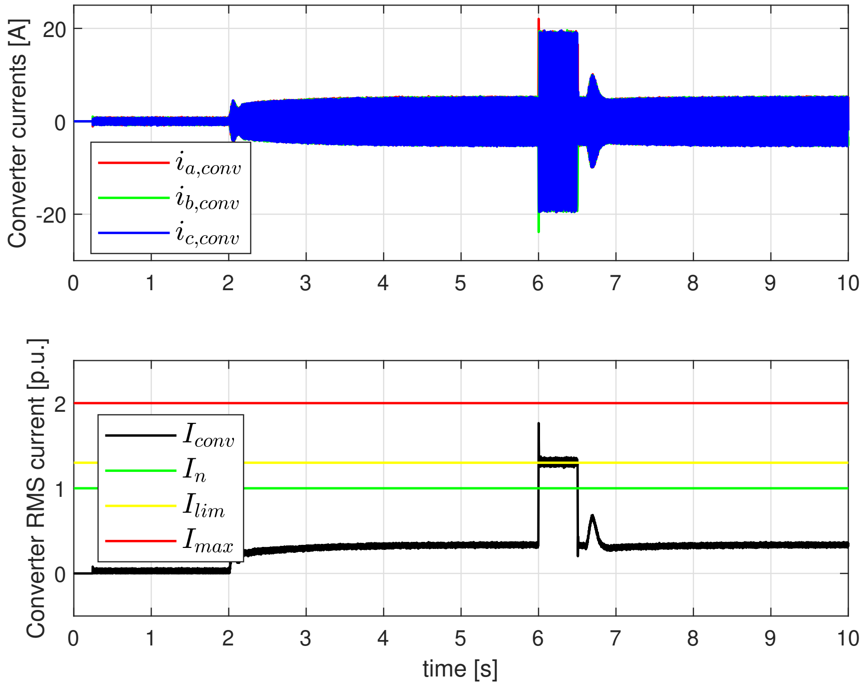

FIGURE 4.34: Currents during faults in Test Case C.

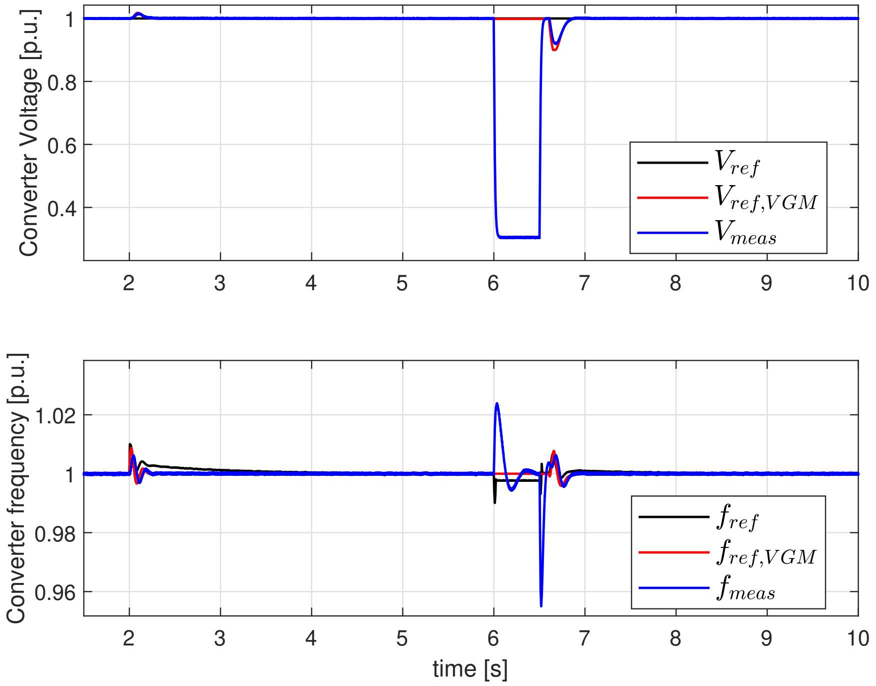

FIGURE 4.35: Voltage and frequency during faults in Test Case C.

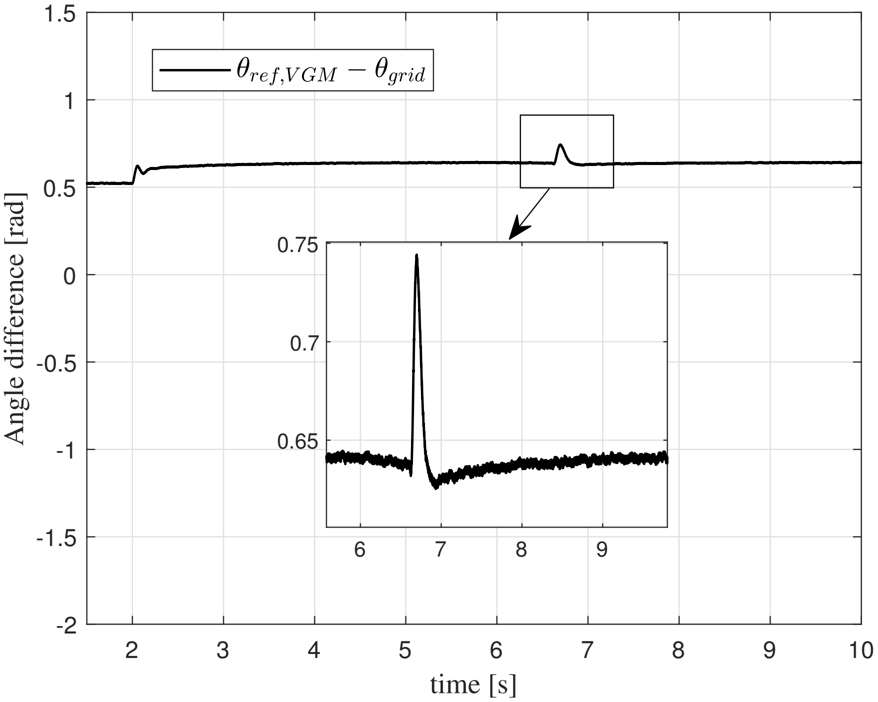

Figure 4.36: Angle difference during faults in Test Case C.

### 4.3.4 Test Case D - Complete case

In this configuration the converter is connected to an external grid. A symmetrical three-phase fault occurs at $t = 6s$ and it is removed after $0.5s$. The Inertia and Rotor Flux values are modified when the fault is detected and Governor and AVR outputs are frozen when the fault is detected. In figure 4.37 it is possible to see that in this configuration the converter is able to restore with fast and smooth dynamics the current previous fault in less than $30ms$ as depicted in figure 4.38 and comparison with the other test cases is depicted in figure 4.39. This speed in the regulation during the resynchronization phase is guaranteed by the joint action of the modification on inertia and rotor flux parameters and by the freezing actions on Governor and AVR as completely described in the previous chapter.

Voltage and frequency level are restored after a short transient as depicted in figure 4.40, more precisely the RMS voltage $V_{meas}$ is restored in less than $100ms$ while the measured frequency $f_{meas}$ after $250ms$. A comparison in terms of the voltage recovery between test cases is depicted in figure 4.41 and the best performance are guaranteed by this last test case. The VGM algorithm is able to resynchronize with the external grid after a very short dynamic as it is shown in figure 4.42. A quantitative comparison in terms of r.t. is reported in table 4.3.

| | **RMS Current r.t.** | **RMS Voltage r.t.** | **Frequency r.t.** |
|---|---|---|---|
| **Test Case A** | $600ms$ | $500ms$ | $500ms$ |
| **Test Case B** | $800ms$ | $800ms$ | $800ms$ |
| **Test Case C** | $800ms$ | $600ms$ | $500ms$ |
| **Test Case D** | $30ms$ | $100ms$ | $250ms$ |

TABLE 4.3: Comparative analysis in grid connected configuration with pre-load producing power.

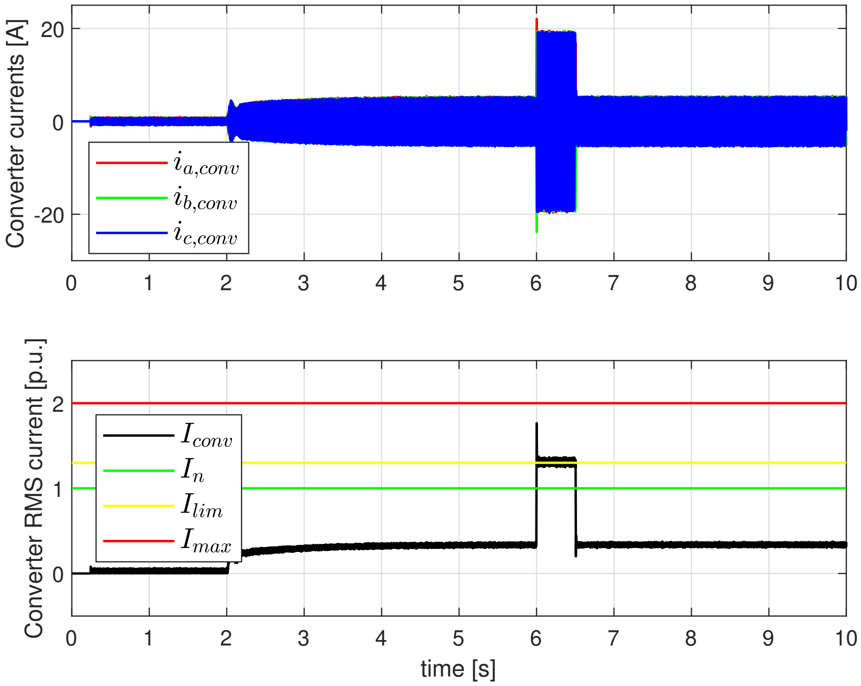

FIGURE 4.37: Currents during faults in Test Case D.

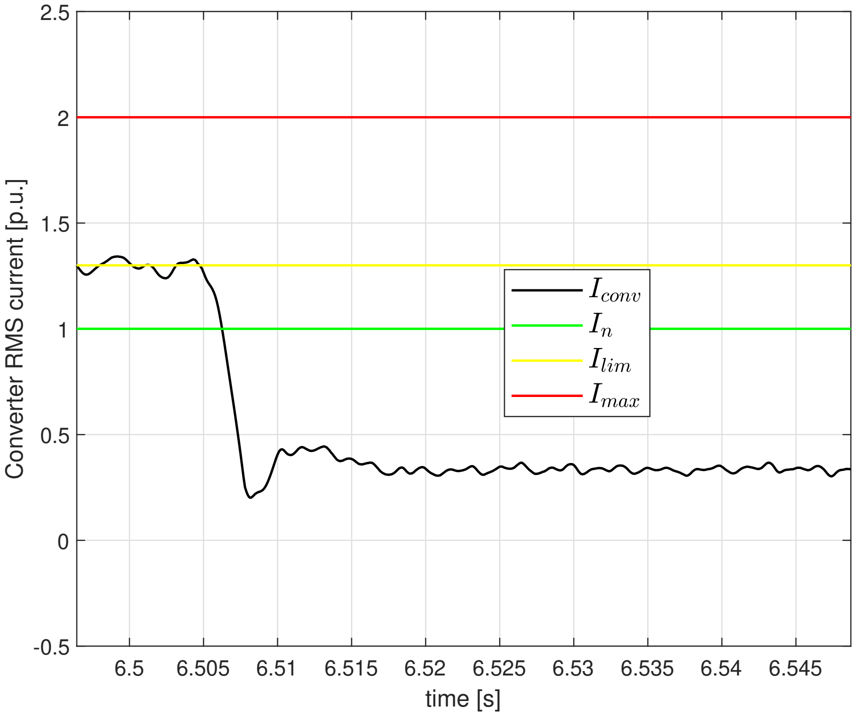

FIGURE 4.38: Currents during faults in Test Case D: detail on resynchronization phase.

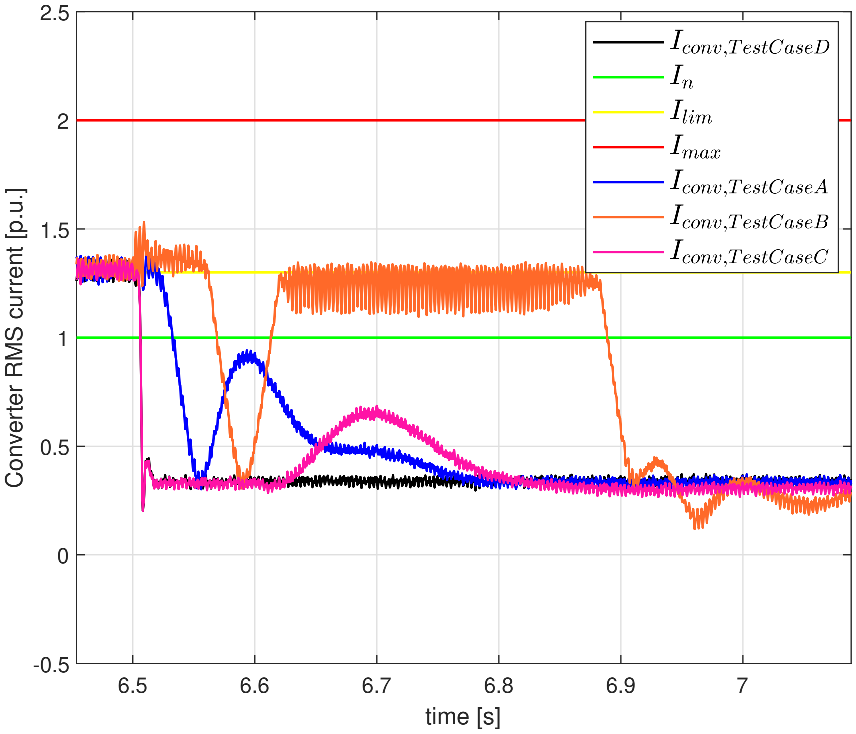

FIGURE 4.39: Currents during faults: comparison between test cases.

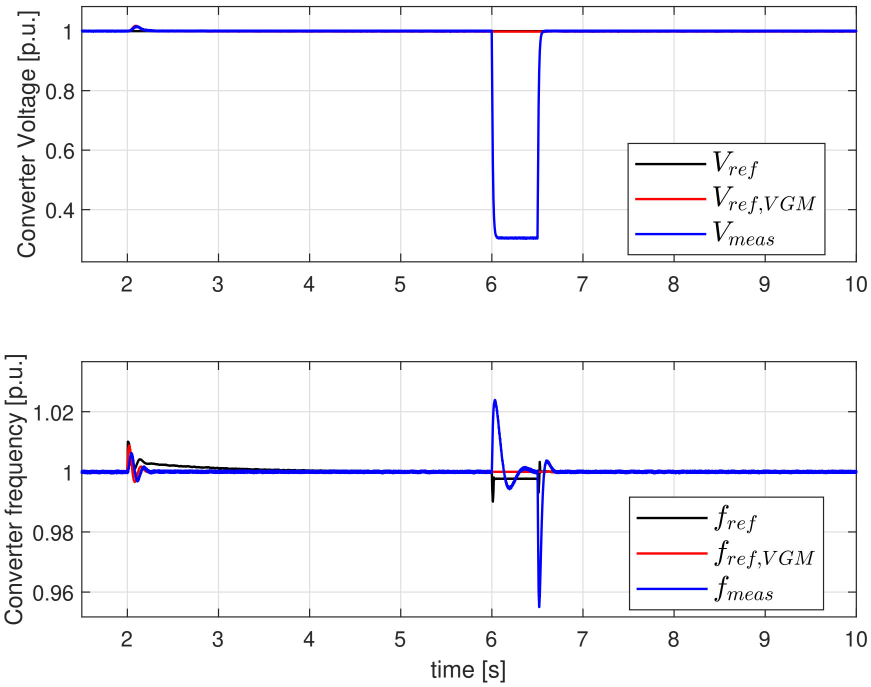

FIGURE 4.40: Voltage and frequency during faults in Test Case D.

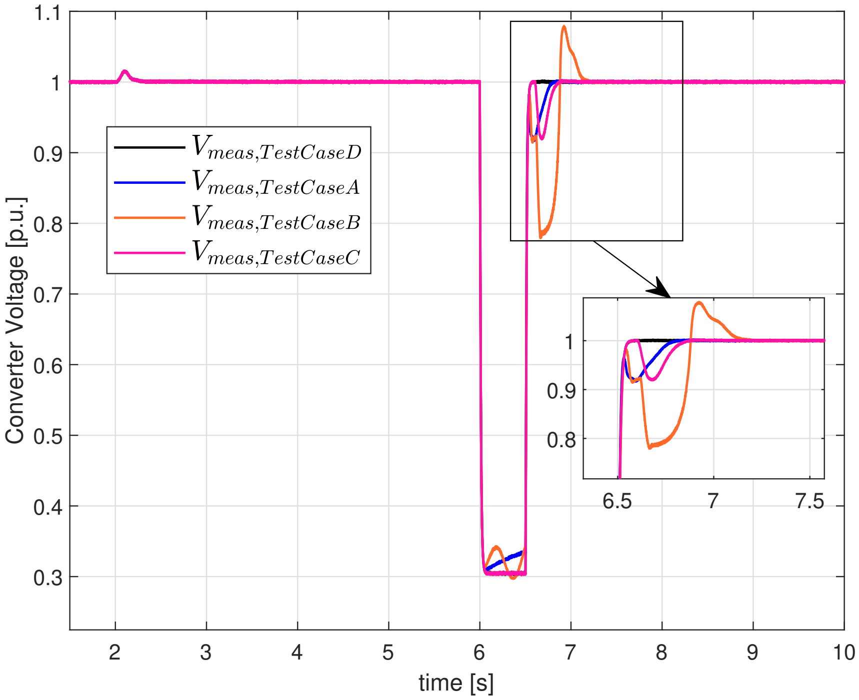

FIGURE 4.41: RMS Voltages during faults: comparison between test cases.

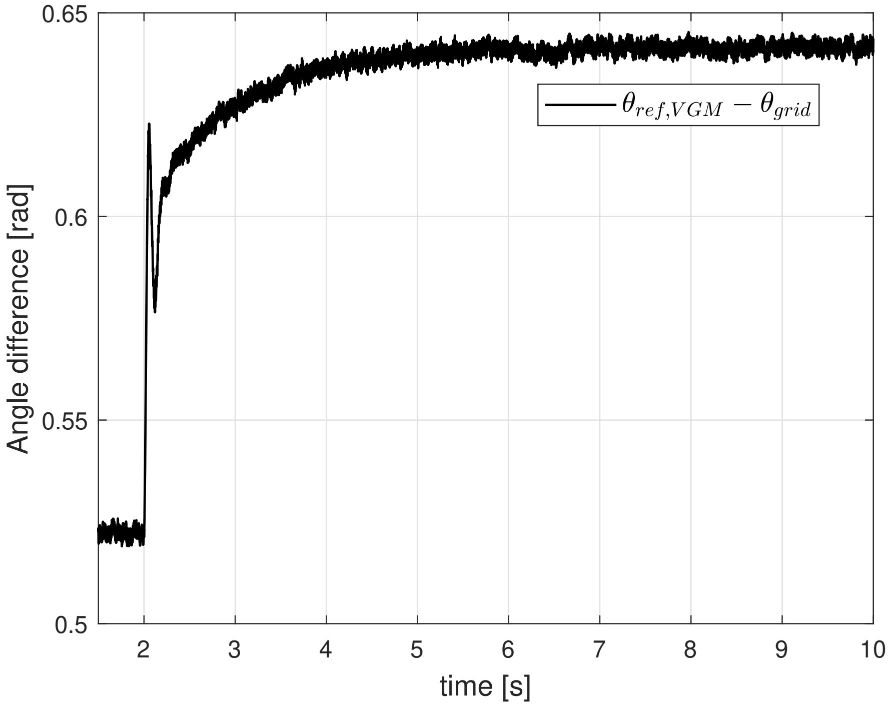

FIGURE 4.42: Angle difference during faults in Test Case D.

## 4.4 Grid-Connected Configuration: BESS pre-load absorbing power

In this scenario the BESS converter is in a grid connected configuration but the initial working point is not a no-load, i.e. the converter is in the pre-load configuration, more precisely a pre load of $-0.3p.u.$ active power and of $+0.3p.u.$ reactive power is implemented. As done in the previous chapter, in every test cases the active power absorption of the BESS is performed with a variation of the VGM algorithm input signal $f_{ref}$ at $t = 2s$ from 50 Hz to 49.5 Hz and the active power droop $m_{droop}$ is not zero.

### 4.4.1 Test Case A - The base case

In this configuration the converter is connected to an external grid. A symmetrical three-phase fault occurs at $t = 6s$ and it is removed after $0.5s$. The inertia and rotor flux values are the standard one while Governor and AVR outputs are not frozen when the fault is detected. In figure 4.43 it is possible to see that in this configuration the converter is able to restore the current previous the fault but with a long transient and it remains in current limit configuration for $300ms$ after the fault clearing and then it returns to previous value with overshoot and a settling time of $500ms$. Voltage and frequency time profiles are reported in figure 4.44, and it is possible to see that the VGM outputs $f_{ref,VGM}$ and $V_{ref,VGM}$ have no an acceptable dynamic. As one can see in figure 4.45, when the fault occurs the angle difference $\theta_{ref,VGM} - \theta_{grid}$ starts to decrease because the VGM output $f_{ref,VGM}$ decreases quickly because the inertia parameter $K_H$ is not modified in this base case. This decrease is the main cause of the slowness of the resynchronization phase.

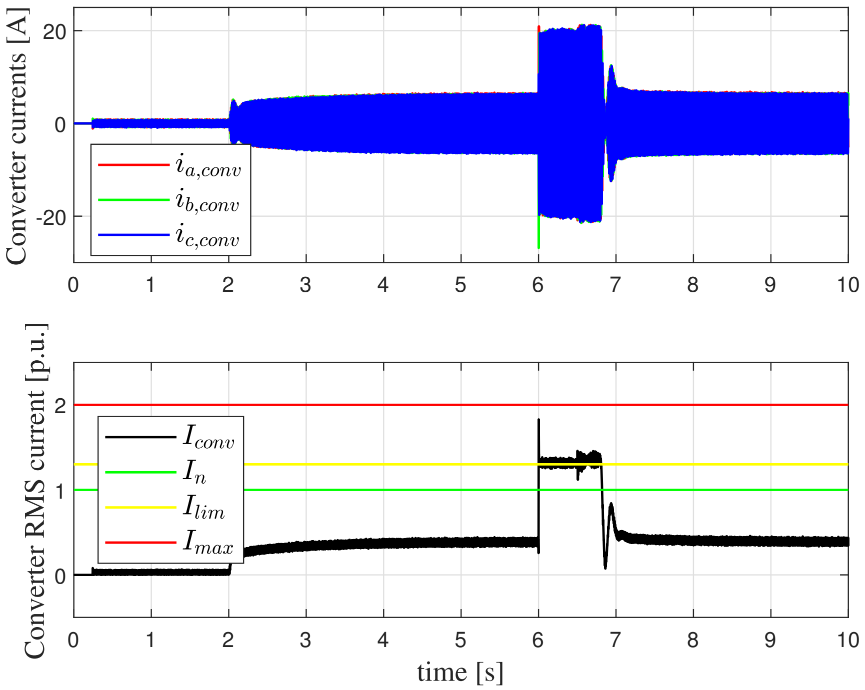

FIGURE 4.43: Currents during faults in Test Case A.

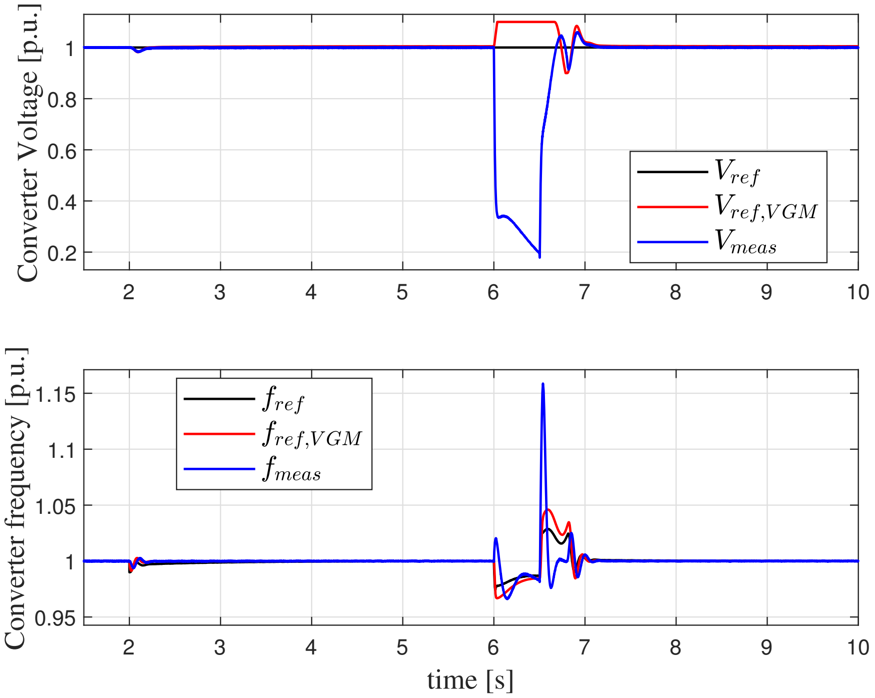

FIGURE 4.44: Voltage and frequency during faults in Test Case A.

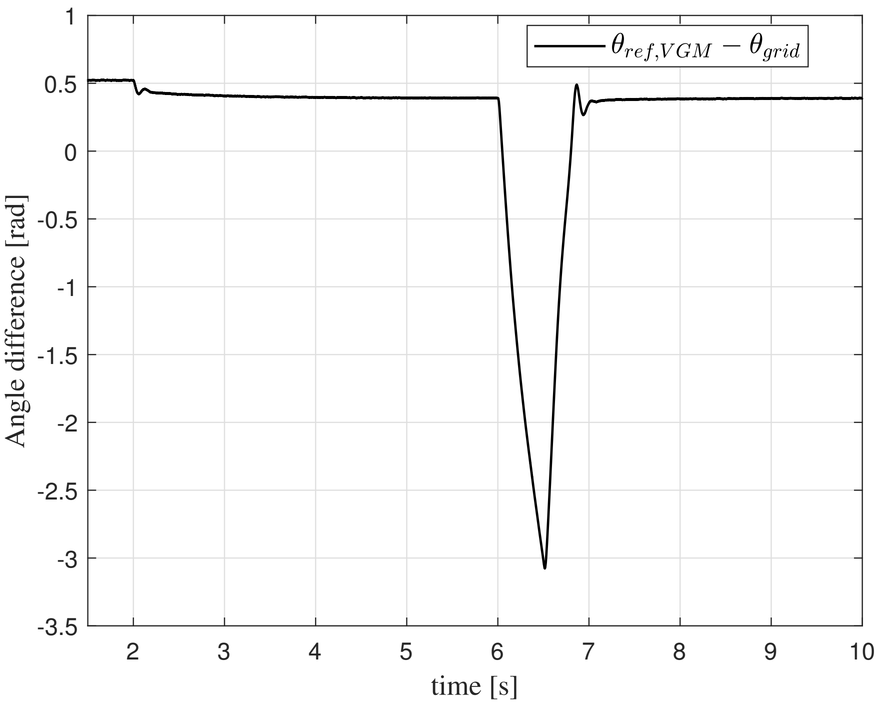

FIGURE 4.45: Angle difference during faults in Test Case A.

### 4.4.2 Test Case B - Freezing actions case

In this configuration the converter is connected to an external grid. A symmetrical three-phase fault occurs at $t = 6s$ and it is removed after $0.5s$. The Inertia and Rotor Flux values are the standard ones while Governor and AVR outputs are frozen when the fault is detected. In figure 4.46 it is possible to see that in this configuration the converter is not able to restore the current previous the fault in a time frame lower than $100ms$. Voltage and frequency time profiles are reported in 4.47 and, as one can see both the VGM output $V_{ref,VGM}$ and $f_{ref,VGM}$ reach their lower and upper limits. This is due to the fact that when the fault is detected the Governor and AVR outputs $P_{GOV}^{BESS}$ and $Q_{AVR}^{BESS}$ are frozen to respective their values previous the fault according to relations (3.31) and (3.32) and this produces a strong variation on the VGM output because the inertia and rotor flux constant $K_H$ and $K_\Psi$ are not modified. Of course this huge variations during the fault are not acceptable for the resynchronization with the external grid, in fact this simulation presents a *pole slipping* event as depicted in figure 4.48 and this is the cause of the different RMS current when the fault is cleared.

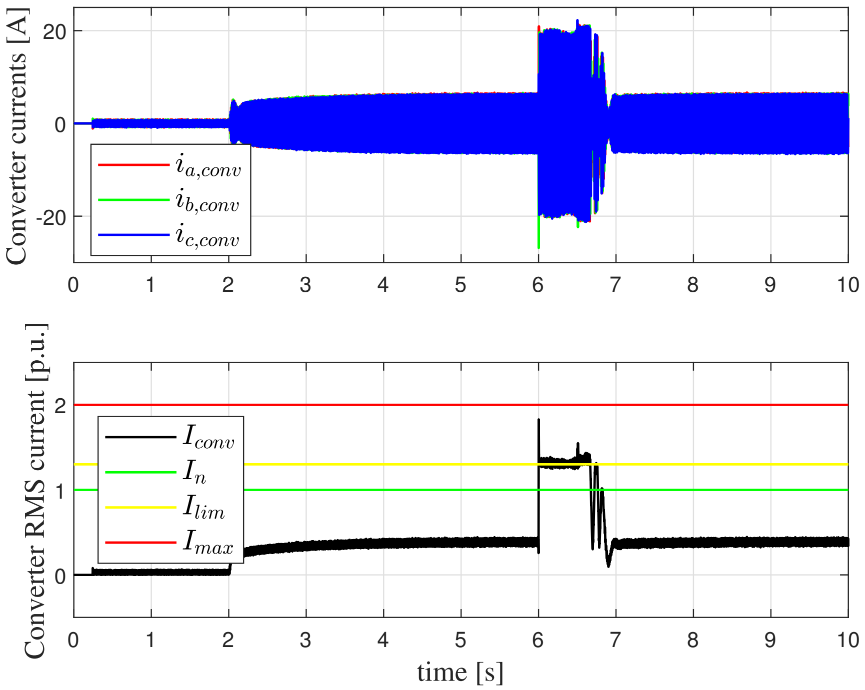

FIGURE 4.46: Currents during faults in Test Case B.

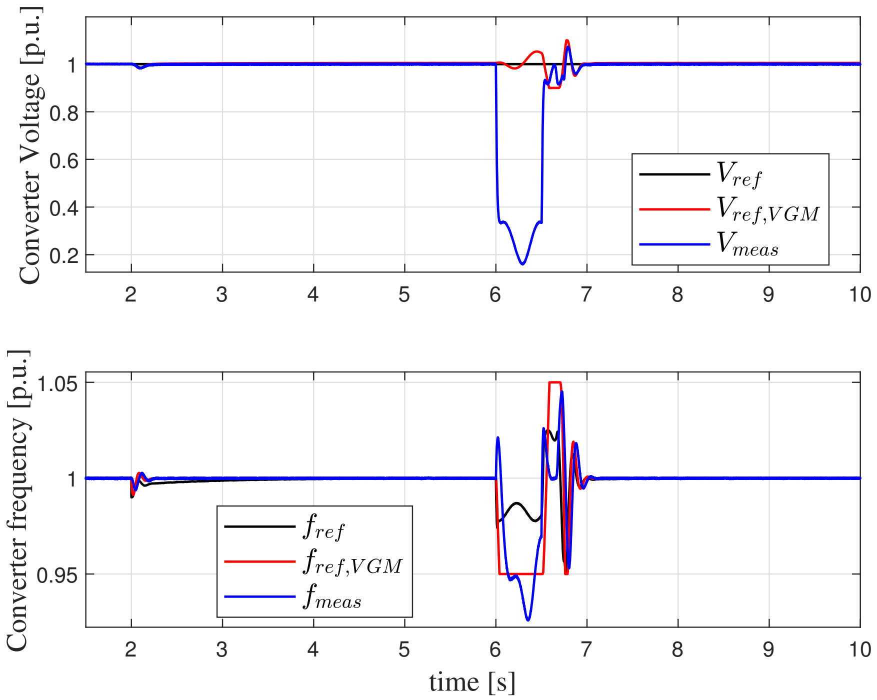

FIGURE 4.47: Voltage and frequency during faults in Test Case B.

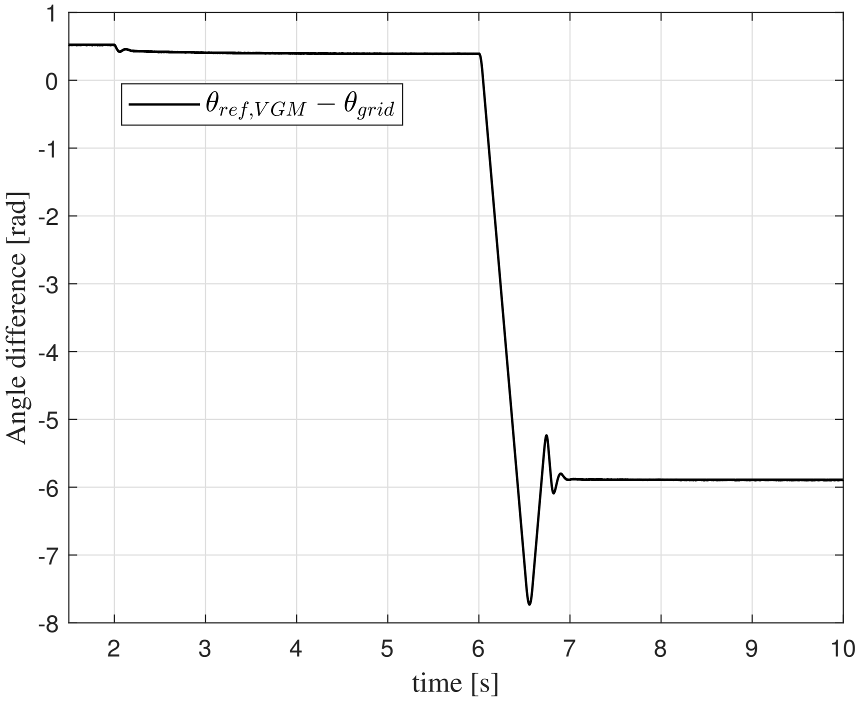

FIGURE 4.48: Angle difference during faults in Test Case B.

### 4.4.3 Test Case C - Parameters modification case

In this configuration the converter is connected to an external grid. A symmetrical three-phase fault occurs at $t = 6s$ and it is removed after $0.5s$. The Inertia and Rotor Flux values are modified when the fault is detected while Governor and AVR outputs are not frozen when the fault is detected. In figure 4.49 it is possible to see the current time profile. Here there something similar to Test Case C in grid connected configuration with no pre-loading and in a pre-loading (power production). In $30ms$ after the fault clearing the converter current return at the previous value but at $6.6s$ it is possible to see a bump in the currents. This is due to the fact that at $6.6s$ inertia and rotor flux variables $K_H$ and $H_\Psi$ return to their rated values but the actions of Governor and AVR are not frozen, i.e. outputs $P_{GOV}^{BESS}$ and $Q_{AVR}^{BESS}$ are not blocked to respective their values previous the fault and so this current bump is imposed by the control when $K_H$ and $K_\Psi$ return to their rated values and by the Governor and AVR input $e_{GOV}$ and $e_{AVR}$ that are non-zero. Voltage and frequency time profiles are reported in figure 4.50 and also here it is possible to see the effect of the parameter control modification. The resynchronization with the external grid is depicted in figure 4.51 and it can be appreciated the fact that, when the fault occurs, the angle difference decreases very slowly and this is due to the modification of the inertia parameter $K_H$.

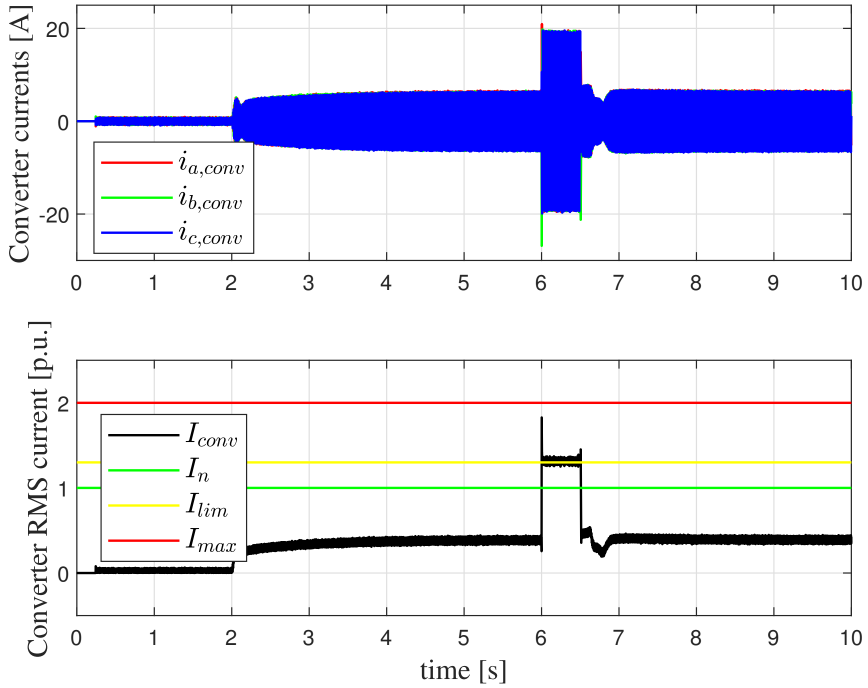

FIGURE 4.49: Currents during faults in Test Case C.

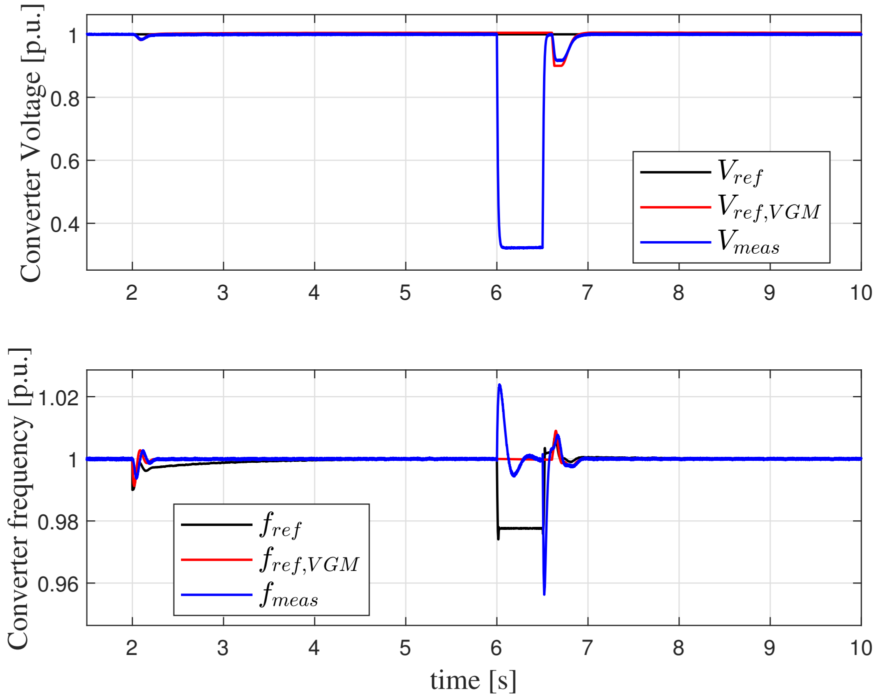

FIGURE 4.50: Voltage and frequency during faults in Test Case C.

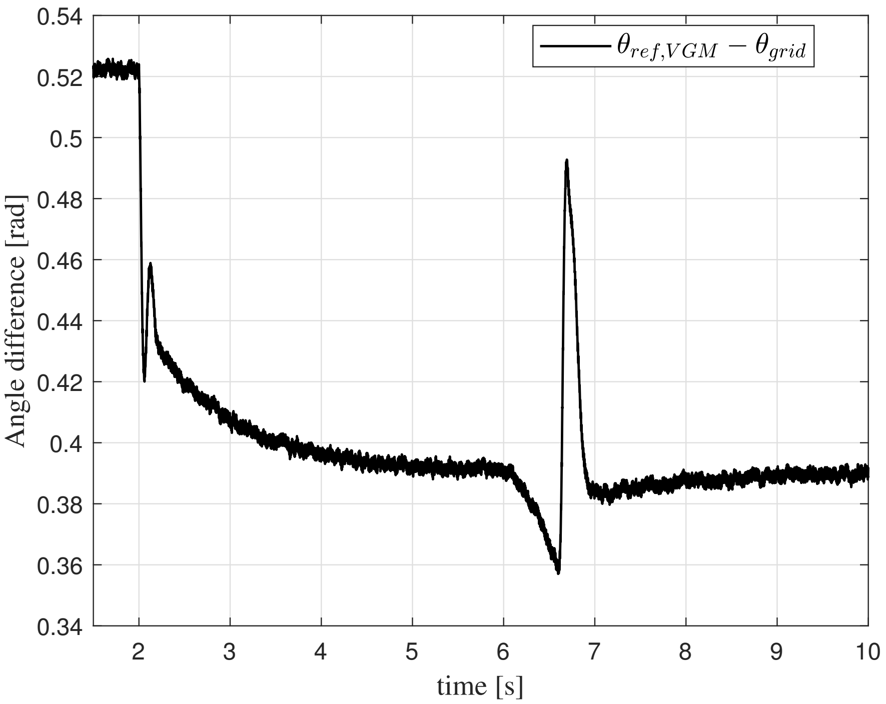

FIGURE 4.51: Angle difference during faults in Test Case C.

### 4.4.4 Test Case D - Complete case

In this configuration the converter is connected to an external grid. A symmetrical three-phase fault occurs at $t = 6s$ and it is removed after $0.5s$. The Inertia and Rotor Flux values are modified when the fault is detected and Governor and AVR outputs are frozen when the fault is detected. In figure 4.52 it is possible to see that in this configuration the converter is able to restore with fast and smooth dynamics the current previous fault in less than $30ms$ as depicted in figure 4.53 and comparison with the other test cases is depicted in 4.54. Voltage and frequency level are restored after a short transient as depicted in figure 4.55, and a comparison in terms of the voltage recovery between test cases is depicted in figure 4.56. The VGM algorithm is able to resynchronize with the external grid after a very short dynamic as it is shown in figure 4.57. A quantitative comparison in terms of r.t. is reported in table 4.4.

| | **RMS Current r.t.** | **RMS Voltage r.t.** | **Frequency r.t.** |
|---|---|---|---|
| **Test Case A** | $700ms$ | $800ms$ | $800ms$ |
| **Test Case B** | $700ms$ | $700ms$ | $700ms$ |
| **Test Case C** | $700ms$ | $600ms$ | $600ms$ |
| **Test Case D** | $30ms$ | $100ms$ | $250ms$ |

TABLE 4.4: Comparative analysis in grid connected configuration with pre-load absorbing power.

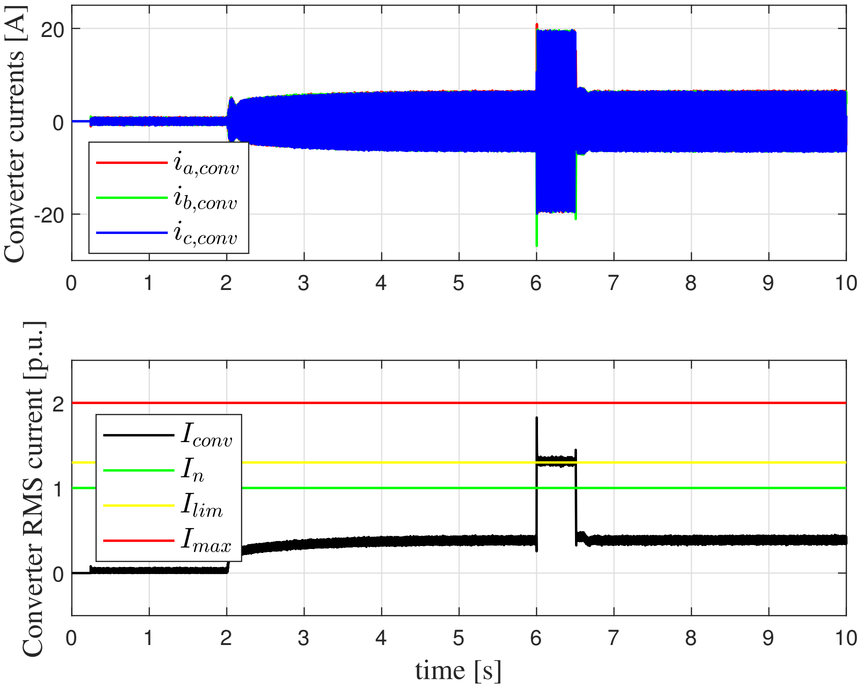

FIGURE 4.52: Currents during faults in Test Case D.

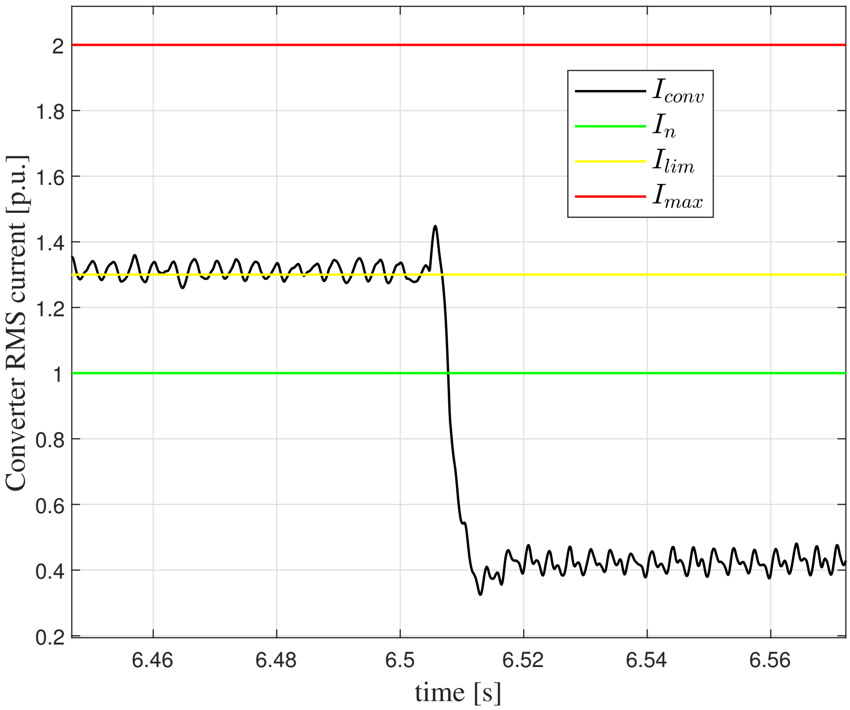

FIGURE 4.53: Currents during faults in Test Case D: detail on resynchronization phase.

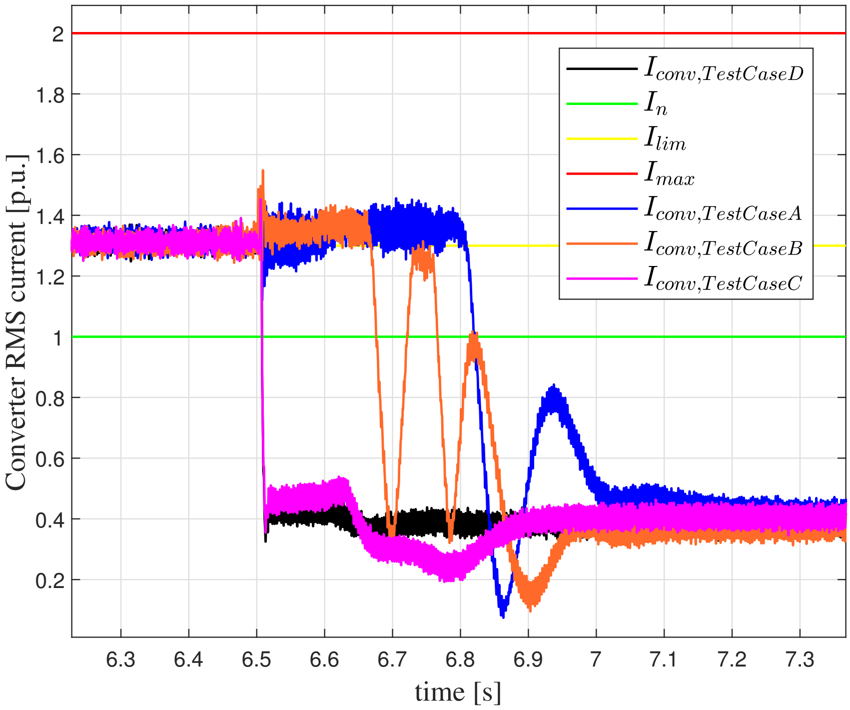

FIGURE 4.54: Currents during faults: comparison between test cases.

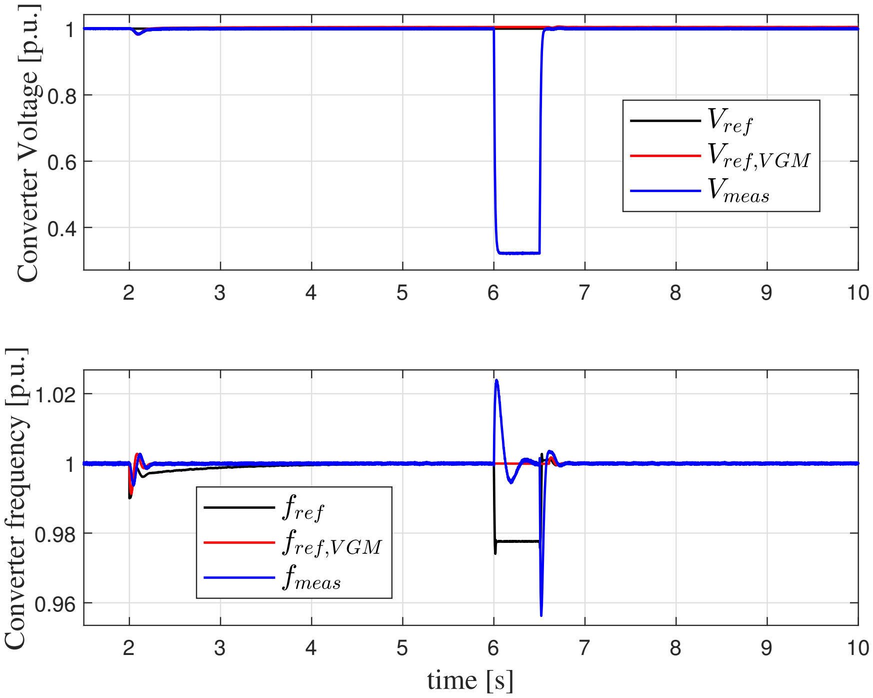

FIGURE 4.55: Voltage and frequency during faults in Test Case D.

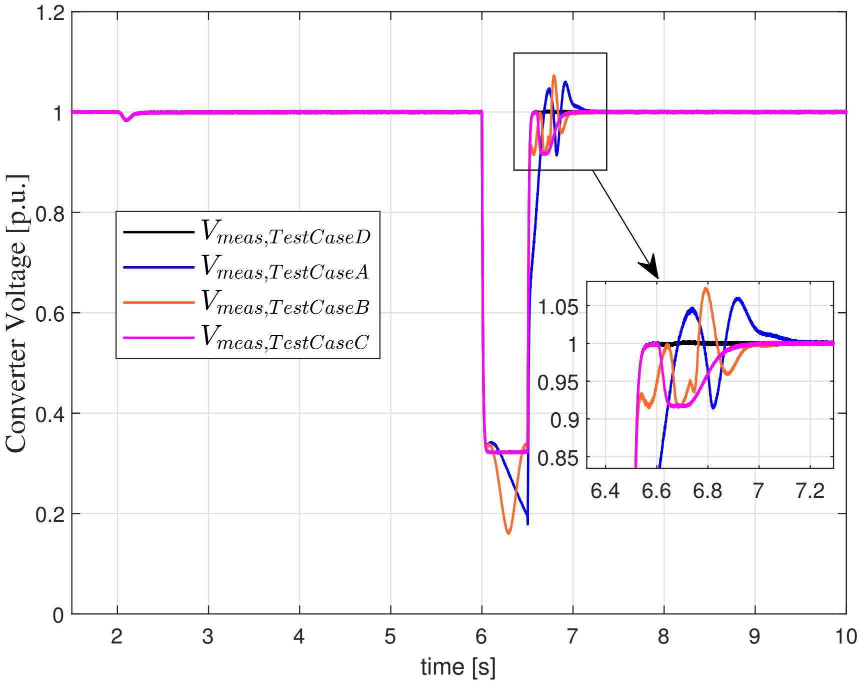

FIGURE 4.56: RMS Voltages during faults: comparison between test cases.

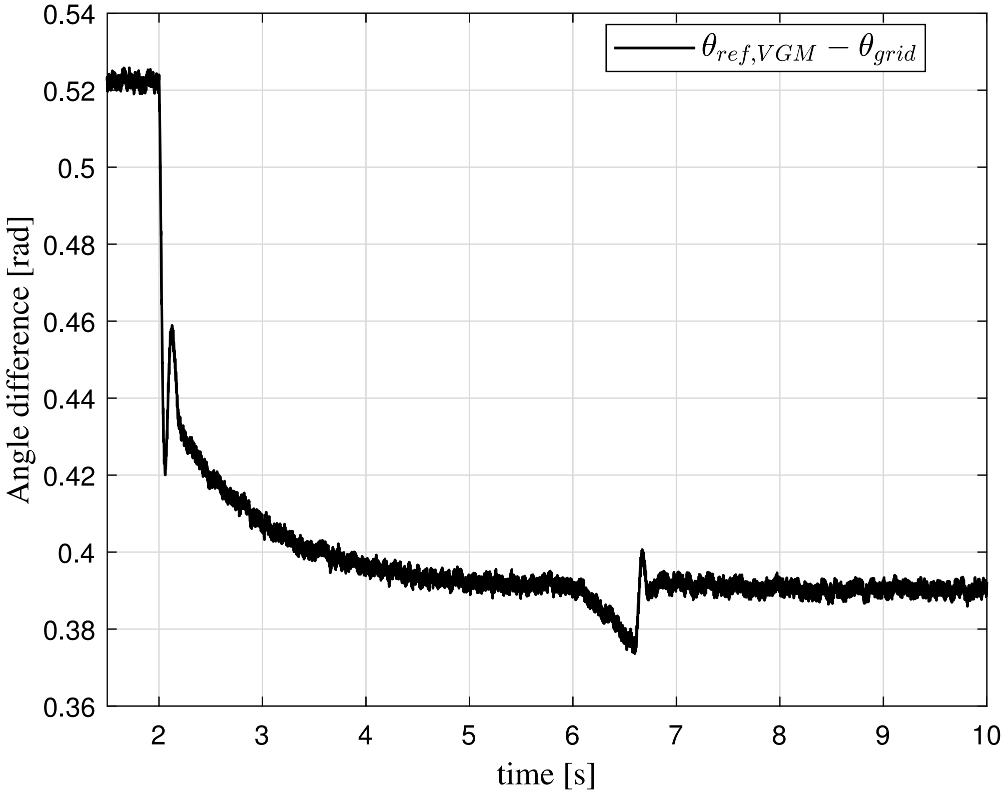

FIGURE 4.57: Angle difference during faults in Test Case D.

# Chapter 5

# Conclusions

This thesis is the final result of academic and industrial research in collaboration with Hitachi Power Grids over the last three years. The first part of this work proposes a new comprehensive primary control for BESS converter in order to provide all the regulations required by IEEE Std. 1547 both in grid-connected and islanded configurations. Due to the need to guarantee fast and smooth dynamics of voltage and frequency in islanded configuration, the BESS converter is controlled using a VGM technique in order to have it acting on the system as a real synchronous generator. Simulations are carried out using the dedicated simulation software DIgSILENT PowerFactory® and show that the proposed controller is able to provide the black-start capability, to regulate frequency and voltage independently of the number of paralleled generators, to synchronize and connect BESS converter to the external main grid or to other DERs in with minimum transients and to guarantee a proper active/reactive power sharing among other DERs. Moreover, simulations showed that the proposed primary control has the possibility to provide fast control actions also in grid-connected mode to allow providing frequency and voltage support (*GSM-fV*) as well as power control following the reference signals from the secondary level control (*GSM-PQ*). Then the thesis moves the attention to the field of VGM algorithm behaviour during faults. It is shown that the proposed VGM algorithm without some corrective actions is not able to guarantee fast recovery in terms of currents and voltage in both islanded and grid-connected configurations and a fast and stable resynchronization to the external grid when the fault is cleared. The proposed strategy to improve the dynamic response of the BESS converter controlled with the VGM strategy during faults is based on the idea that emulation of the dynamic behaviour of a synchronous generator with its controls leaves the possibility of modifying parameters and acting on quantities that obviously would not be possible to apply on a traditional synchronous generator. For this reason an adaptive VGM strategy is proposed in this thesis and it is based on the inertia and rotor flux parameters modification and Governor and AVR freezing actions when a fault event is detected. Simulations results show that the proposed VGM algorithm, with a proper current limiting strategy and with the adaptive algorithm for fault conditions can guarantee excellent performances in terms of recovery time in islanded configuration and a fast resynchronization when connected to external grid also considering voltage disturbances and pre-loading of BESS converter.

# Bibliography

[1] International Renewable Energy Agency. *Renewable Energy Statistics 2020.* IRENA, 2020.

[2] Ali Bidram and Ali Davoudi. Hierarchical structure of microgrids control system. *IEEE Transactions on Smart Grid*, 3(4):1963–1976, 2012.

[3] Ieee standard for interconnection and interoperability of distributed energy resources with associated electric power systems interfaces. *IEEE Std 1547-2018 (Revision of IEEE Std 1547-2003)*, pages 1–138, 2018.

[4] HH Zeineldin, EF El-Saadany, and MMA Salama. Islanding detection of inverter-based distributed generation. *IEE Proceedings-Generation, Transmission and Distribution*, 153(6):644–652, 2006.

[5] HH Zeineldin, EF El-Saadany, and MMA Salama. Distributed generation micro-grid operation: Control and protection. In *2006 Power Systems Conference: Advanced Metering, Protection, Control, Communication, and Distributed Resources*, pages 105–111. IEEE, 2006.

[6] Nimat Shamim, Anitha Sarah Subburaj, and Stephen B Bayne. Renewable energy based grid connected battery projects around the world—an overview. *Journal of Energy and Power Engineering*, 13:1–23, 2019.

[7] Giuliano Rancilio, Arianna Rossi, Claudio Di Profio, Martino Alborghetti, Andrea Galliani, and Marco Merlo. Grid-scale bess for ancillary services provision: Soc restoration strategies. *Applied Sciences*, 10(12):4121, 2020.

[8] Jia Liu, Yushi Miura, and Toshifumi Ise. Comparison of dynamic characteristics between virtual synchronous generator and droop control in inverter-based distributed generators. *IEEE Transactions on Power Electronics*, 31(5):3600–3611, 2015.

[9] Hassan Bevrani. *Robust power system frequency control*, volume 85. Springer, 2009.

[10] Joan Rocabert, Alvaro Luna, Frede Blaabjerg, and Pedro Rodriguez. Control of power converters in ac microgrids. *IEEE transactions on power electronics*, 27(11): 4734–4749, 2012.

[11] Qing-Chang Zhong and George Weiss. Synchronverters: Inverters that mimic synchronous generators. *IEEE transactions on industrial electronics*, 58(4):1259–1267, 2010.

[12] Qing-Chang Zhong, Phi-Long Nguyen, Zhenyu Ma, and Wanxing Sheng. Self-synchronized synchronverters: Inverters without a dedicated synchronization unit. *IEEE Transactions on power electronics*, 29(2):617–630, 2013.

[13] Qing-Chang Zhong, George C Konstantopoulos, Beibei Ren, and Miroslav Krstic. Improved synchronverters with bounded frequency and voltage for smart grid integration. *IEEE Transactions on Smart Grid*, 9(2):786–796, 2016.

[14] Salvatore D'Arco and Jon Are Suul. Virtual synchronous machines—classification of implementations and analysis of equivalence to droop controllers for microgrids. In *2013 IEEE Grenoble Conference*, pages 1–7. IEEE, 2013.

[15] Abdolwahhab Fathi, Qobad Shafiee, and Hassan Bevrani. Robust frequency control of microgrids using an extended virtual synchronous generator. *IEEE Transactions on Power Systems*, 33(6):6289–6297, 2018.

[16] Meng Chen, Dao Zhou, and Frede Blaabjerg. Impact of synchronous generator replacement with vsg on power system stability. In *2020 IEEE 21st Workshop on Control and Modeling for Power Electronics (COMPEL)*, pages 1–7. IEEE, 2020.

[17] Yuko Hirase, Osamu Noro, Eiji Yoshimura, Hidehiko Nakagawa, Kenichi Sakimoto, and Yuji Shindo. Virtual synchronous generator control with double decoupled synchronous reference frame for single-phase inverter. *IEEJ Journal of Industry Applications*, 4(3):143–151, 2015.

[18] Yong Chen, Ralf Hesse, Dirk Turschner, and Hans-Peter Beck. Improving the grid power quality using virtual synchronous machines. In *2011 international conference on power engineering, energy and electrical drives*, pages 1–6. IEEE, 2011.

[19] Yang Xiang-Zhen, Su Jian-hui, Ding Ming, Li Jin-wei, and Du Yan. Control strategy for virtual synchronous generator in microgrid. In *2011 4th International Conference on Electric Utility Deregulation and Restructuring and Power Technologies (DRPT)*, pages 1633–1637. IEEE, 2011.

[20] K Sakimoto, Y Miura, T Ise, and V Ceccarelli. Stabilization of a power system with a distributed generator by a virtual synchronous generator function. In *8th International Conference on Power Electronics-ECCE Asia*, pages 1498–1505. IEEE, 2011.

[21] Toshinobu Shintai, Yuushi Miura, and Toshifumi Ise. Reactive power control for load sharing with virtual synchronous generator control. In *Proceedings of The 7th International Power Electronics and Motion Control Conference*, volume 2, pages 846–853. IEEE, 2012.

[22] Toshinobu Shintai, Yushi Miura, and Toshifumi Ise. Oscillation damping of a distributed generator using a virtual synchronous generator. *IEEE transactions on power delivery*, 29(2):668–676, 2014.

[23] Jaber Alipoor, Yushi Miura, and Toshifumi Ise. Power system stabilization using virtual synchronous generator with alternating moment of inertia. *IEEE journal of Emerging and selected topics in power electronics*, 3(2):451–458, 2014.

[24] Andrew Tuckey and Simon Round. Practical application of a complete virtual synchronous generator control method for microgrid and grid-edge applications. In *2018 IEEE 19th Workshop on Control and Modeling for Power Electronics (COMPEL)*, pages 1–6. IEEE, 2018.

[25] J. Driesen and K. Visscher. Virtual synchronous generators. In *2008 IEEE Power and Energy Society General Meeting - Conversion and Delivery of Electrical Energy in the 21st Century*, pages 1–3, 2008. doi: 10.1109/PES.2008.4596800.

[26] K. Sakimoto, Y. Miura, and T. Ise. Stabilization of a power system with a distributed generator by a virtual synchronous generator function. In *8th International Conference on Power Electronics - ECCE Asia*, pages 1498–1505, 2011. doi: 10.1109/ICPE.2011.5944492.

[27] M. Guan, W. Pan, J. Zhang, Q. Hao, J. Cheng, and X. Zheng. Synchronous generator emulation control strategy for voltage source converter (vsc) stations. *IEEE*

*Transactions on Power Systems*, 30(6):3093–3101, 2015. doi: 10.1109/TPWRS.2014.2384498.

[28] J. Jia, G. Yang, and A. H. Nielsen. A review on grid-connected converter control for short-circuit power provision under grid unbalanced faults. *IEEE Transactions on Power Delivery*, 33(2):649–661, 2018.

[29] E. Afshari, G. R. Moradi, R. Rahimi, B. Farhangi, Y. Yang, F. Blaabjerg, and S. Farhangi. Control strategy for three-phase grid-connected pv inverters enabling current limitation under unbalanced faults. *IEEE Transactions on Industrial Electronics*, 64(11):8908–8918, 2017.

[30] M. Abdelrahem and R. Kennel. Direct-model predictive control for fault ride-through capability enhancement of dfig. In *PCIM Europe 2017; International Exhibition and Conference for Power Electronics, Intelligent Motion, Renewable Energy and Energy Management*, pages 1–8, 2017.

[31] N. Bottrell and T. C. Green. Comparison of current-limiting strategies during fault ride-through of inverters to prevent latch-up and wind-up. *IEEE Transactions on Power Electronics*, 29(7):3786–3797, 2014. doi: 10.1109/TPEL.2013.2279162.

[32] Z. Shuai, W. Huang, C. Shen, J. Ge, and Z. J. Shen. Characteristics and restraining method of fast transient inrush fault currents in synchronverters. *IEEE Transactions on Industrial Electronics*, 64(9):7487–7497, 2017. doi: 10.1109/TIE.2017.2652362.

[33] J. Alipoor, Y. Miura, and T. Ise. Voltage sag ride-through performance of virtual synchronous generator. In *2014 International Power Electronics Conference (IPEC-Hiroshima 2014 - ECCE ASIA)*, pages 3298–3305, 2014. doi: 10.1109/IPEC.2014.6870160.

[34] Weiyi Zhang, Joan Rocabert, J Ignacio Candela, and Pedro Rodriguez. Synchronous power control of grid-connected power converters under asymmetrical grid fault. *Energies*, 10(7):950, 2017.

[35] Aravinda Perera. Virtual synchronous machine-based power control in active rectifiers for micro grids. Master's thesis, Institutt for elkraftteknikk, 2012.

[36] M. S. Moon and R. W. Johnson. Dsp control of ups inverter with over-current limit using droop method. In *30th Annual IEEE Power Electronics Specialists Conference. Record. (Cat. No.99CH36321)*, volume 1, pages 552–557 vol.1, 1999. doi: 10.1109/PESC.1999.789071.

[37] S. Barsali, M. Ceraolo, P. Pelacchi, and D. Poli. Control techniques of dispersed generators to improve the continuity of electricity supply. In *2002 IEEE Power Engineering Society Winter Meeting. Conference Proceedings (Cat. No.02CH37309)*, volume 2, pages 789–794 vol.2, 2002. doi: 10.1109/PESW.2002.985115.

[38] JA Peças Lopes, CL Moreira, and FO Resende. Control strategies for microgrids black start and islanded operation. *International journal of distributed energy resources*, 1(3):241–261, 2005.

[39] DIgSILENT PowerFactory. Digsilent powerfactory 15 user manual. *DIgSILENT GmbH, May-2014*, 2013.

[40] Prabha Kundur, Neal J Balu, and Mark G Lauby. *Power system stability and control*, volume 7. McGraw-hill New York, 1994.